ISSN en trámite

Geofísica Internacional

Revista Trimestral Publicada por el Instituto de Geofísica de la Universidad Nacional Autónoma de México

México
Volume 57 Number 4
October - December
2018

— Geofísica Internacional —

GEOFÍSICA INTERNACIONAL, Año 57, Vol. 57, Núm. 4, octubre - diciembre de 2018 es una publicación trimestral, editada por la Universidad Nacional Autónoma de México, Ciudad Universitaria, Alcaldía Coyoacán, C.P. 04150, Ciudad de México, a través del Instituto de Geofísica, Circuito de la Investigación Científica s/n, Ciudad Universitaria, Alcaldía Coyoacán, C.P. 04150, Ciudad de México, Tel. (55)56 22 41 15. URL: http://revistagi.geofisica.unam.mx, correo electrónico: revistagi@igeofisica.unam.mx. Editora responsable: Andrea Rostan Robledo. Certificado de Reserva de Derechos al uso Exclusivo del Título: 04-2022-081610251200-102, ISSN: en trámite, otorgados por el Instituto Nacional del Derecho de Autor (INDAUTOR). Responsable de la última actualización Saúl Armendáriz Sánchez, Editor Técnico. Fecha de la última modificación: 30 de septiembre 2018, Circuito de la Investigación Científica s/n, Ciudad Universitaria, Alcaldía Coyoacán, C.P. 04150, Ciudad de México.

Geofísica Internacional

Vol. 57, Núm. 4, octubre-diciembre de 2018

Contents

Geofísica Internacional (2018) 57-4: 223-237

Original paper

Evaluation of the leakage origin in Abu Baara earthen dam using electrical resistivity tomography, northwestern Syria

W. Al-Fares and J. Asfahani*

Received: March 26, 2017; accepted: February 16, 2018; published on line: October 03, 2018

Resumen

Se propone un enfoque geofísico integrado para identificar las posibles zonas de fuga dentro de la roca madre de la subestructura cercana al cuerpo de la presa. Este enfoque incluye investigación geofísica basadas en la tomografía de resistividad eléctrica (ERT, por sus siglas en inglés) y datos tradicionales de sondeo VES. La obtención de datos se llevó a cabo en la presa de tierra Abu Baara, ubicada en los márgenes del sur de la llanura de Al-Ghab al noroeste de Siria; el embalse corriente abajo, y la cresta de la presa. Los resultados adquiridos se interpretaron mediante el uso de diferentes técnicas, en particular la de Pichgin y Habibullaev. En los alrededores de la presa se distinguieron tres bloques principales que distinguió las rocas subestructurales. Los depósitos aluviales se superponen a una roca de piedra caliza y un lecho rocoso con dolomita con valores de resistencia que oscilan entre 300 y 1200 m. Se identificaron varias características anómalas estructurales dentro del lecho rocoso de carbonato duro. Estas características están relacionadas de forma mínima con elementos tectónicos como fallas, fracturas o cavidades kársticas. El segundo bloque central parece estar relacionado con una estructura con fallas o hundimientos que coinciden con el valle principal. Este valle se encuentra completamente lleno de depósitos aluviales de más de 50 m de espesor. Por lo tanto, son consideradas las principales causas de los procesos de fuga de la presa. El enfoque geofísico integrado presentado y propuesto en este documento podría aplicarse fácilmente en otras represas similares que sufren problemas de fugas. Palabras clave: estudio ERT, técnica de Pichgin y Habibullaev, filtración, Abu Baara Earthdam, Siria.

Palabras clave: estudio ERT, técnica de Pichgin y Habibullaev, filtración, Abu Baara earthdam, Abu Baara earthdam, Siria.

Abstract

An integrated geophysical approach is proposed herewith to identify the potentialleakage zones within the substructure bedrock close to the dam body. Such an approach includes geophysicalsurveys using Electrical Resistivity Tomography (ERT), and traditional VES soundings. Geophysical measurements were carried out at the Abu Baara earth fill dam, located at the southern margins of Al-Ghab plain northwest of Syria.Three long ERT profiles(P1, P2, and P3)were implemented in parallel with the dam embankment in up and down stream reservoir as well as on the dam crest.The acquired geophysical results were interpreted by using different interpretative techniques, particularly the Pichgin and Habibullaev technique one. Three main major blocks, characterizing the geological substructural rocks were distinguished in the surrounding of the studied dam. The alluvial deposits overlaya resistiveand fractured limestone and dolomite bedrock with resistivity values ranging between 300 and 1200 Ωm. Several structural anomalous features were identified within the hard carbonate bedrock. These features are almost related to tectonic elements such as faults, fractures or karstic cavities. The central second block seems to be related to a faulted or subsidence structure coinciding with the main valley, completely filled by alluvial deposits of more than 50m thickness.The detected features represented by faulted structures, fractures and the karstic occurrences, developed within the dam bedrock are therefore regarded as the main responsible causes of the leakage processes from the dam. The integrated geophysical approach presented and proposed in this paper could be easily applied in another similar dams suffering from leakage problems.

Key words: ERT survey, Pichgin and Habibullaev technique, leakage, Abu Baara earthdam, Syria.

W. Al-Fares
J. Asfahani*
Atomic Energy Commission of Syria
Department of Geology
P.O Box 6091, Damascus, Syria
*Corresponding author: cscientific2@aec.org.sy

Introduction

Syria is located in a semiarid region, where most of the aquifer basinssuffer from water shortage and limitation in water supply. This situation cameas a result of the climatic conditions prevailing in the region, increasing in population rateand accelerated urbanization and economic development. Those combined factor surged during the last three decades the decision-makersto plan for construction tens of damsto meet the increasing demands for water. Syria has actually more than 160 earth fill dams and impounding reservoirs scattered throughout all the Syrian territory. Several of those damsas the earthen dams around the world unfortunately suffer from common filtration or leakage problems.

Water leakage in dam almost occurs either through the bedrock of dam'slake or through the dam body foundations. The geological and tectonic features such as faults, fractures and karstic featuresare the main factors of the leakage causes in earthen dams(Al Saigh *et al*. 1994; Johansson and Dahlin, 1996; Panthulu *et al*., 2001; Wan and Fell, 2004; Rozycki *et al*., 2006; Oh and Sun, 2008; Asfahani *et al*., 2010; Boleve *et al*., 2011; Bedrosian *et al*., 2012).

Modern geophysical techniques in this context are considered as an effective tool in dam'swater leakage investigations. Recently, Electrical Resistivity Tomography (ERT) becomes one of the main geophysical techniques wildly employed in hydrogeology and earth sciences applications. This technique has proven its performance in detecting the leakage path way soccurring in earthendams through numerous works around the world. (Seaton and Burbey, 2002;Sjödahl *et al*., 2006; Cho and Yeom, 2007; Osazuwa1 and Chii, 2009; Zhu *et al*.,2011; Al-Fares 2011; Thompson at al., 2012;Ikard *et al*., 2014). The present paper is therefore oriented towards demonstrating on how the modern geophysical methods such as the ERT one widely contributes in solving hydrogeological problems basically related to dame leakages. Abu Baara dam in Syria is treated herein as a case study, where an integrated geophysical approach, including different techniques with their specific interpretations is proposed and applied. This approach could be easily practiced in other dams suffering from similar leakage's problems.

The main objectives of this paper are therefore the following:

1. Proposing an integrated geophysical approach for delineating and solving the dam's leakage problems.

2. Carrying out geophysical surveys in Abu Baara dam, including mainly the ERT and traditional VES sounding techniques.

3. Interpreting the acquired geophysical results by different interpretative techniques, such as the 2D inversion of ERT, practiced on three executed profiles (P1, P2, and P3), Inverse slope method, and Pichgin technique, practiced only on P1.

4. Identifying the potentialleakage zones within the substructure bedrock close to this dam, through integrating and compiling the different geophysical results obtained in this research case study.

Geological and Hydrogeological Framework

Abu Baara dam is situated at the southern margins of Al-Ghab plain depression, 30 km west of Hama city (Figure 1). The depression of Al-Ghabis developed by the effect of the tectonic evolution along the northern parts of the Dead Sea Fault System (DSFS) in the northwestern part of Syria. This depression forms a plain region suitablefor agriculture due to the suitable climate conditions, fertile lands and reasonable average rainfall (700 mm/y). The flanks of the depression are clearly limited by faults with series of blocks and scarps (Devyatkin *et al*., 1997; Brew, 2001; Gomez *et al*., 2006; Hamade and Tabet, 2013).

Geologically, Al-Ghab depression is filled with Neogene and Quaternary lacustrine, and alluvium deposits. The thickness of these deposits may reaches more than 100 m in the central part of the basin. The Neogene and Quaternary sediments are uncomfortablyoverlaying the Cretaceous calcareous rocks, which form the bottom of the basin(Ponikarov, 1963). The lake of Abu Baara dam is mainly composed of Quaternary alluvial deposits of clays, silts, sands and gravels (Q_3), in addition to some conglomerates of carbonate-siliceous cement (Figure1). The thicknesses of the Quaternary deposits vary from 1-10m in some places. The limestone and dolomite rocks of Cenomanian-Turonian (Cr_2cm-t) constitute the bedrock of the dam's lake. Those rocks are characterized by extensive fissures and karstic features, which contribute in forming of cavities and karstic conduits (Ponikarov, 1963).

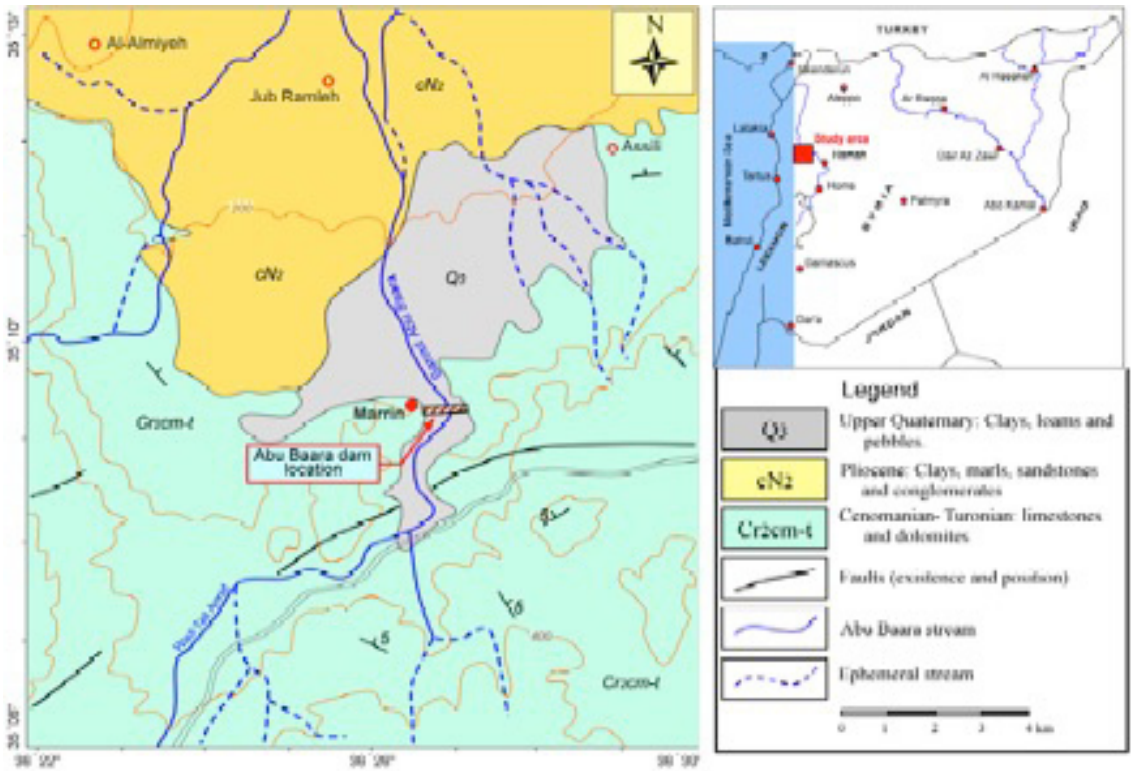

Figure 1. Simplified geological map of the study area showing the location of AbuBaara earth dam (modified after Ponikarov, 1963).

Hydrogeologicaly, the limestone and dolomite of Cenomanian-Turonian rocks constitute the main aquifer in the study area. These formations are characterized by high permeability due to the presence of faults, fractures as well as the common occurrences of karstification at various depths. Whereas, the Quaternary alluvial deposits, composed of clay, sand and gravel constitute the second groundwater aquifer in the study area. The groundwater flow direction is generally from south to north corresponding to the rivers flow direction in the region.These aquifers receive its groundwater feeding from direct recharge of rainfall and drainage network.

Abu Baaradam characterization

Abu Baara dam is one of the earthen-filled dams in Syria, which suffers from an intensive leakage through the lake's bedrock. The dam is located close to Maarin village at the southern margins of Al-Ghab plain, north-west of Syria(Figure 1). The dam was built in the eighties of the last century to protect a part of Al-Ghab plain from rain floods and to satisfy the needs of irrigation and agricultural development in the area. The dam'sembankment is essentially composed of a homogenous clayey core surrounded by filtering layers of sands and various mixtures on sides (Figure 2). The filtering layers themselves are covered by support coarse rock fills to protect the clay core and save the stability of the dam. The dam's embankmenthas east-west direction, perpendicular to the main valley, and extends at distance of 720m with maximum thickness of 24.5m. The crest of the dam has as an absolute elevation of 234.5m above sea level (a.s.l). The dam's lake extends on a surface of 100 hectares with a storage capacity of 7.6 million m^3. The dam is subjected to an intensive leakage, despiteits modest water storage capacity. However, it represents a useful scientific case study. In fact, the dam is located in a complicated geological area and the site locationcontains many tectonic and karstic features, which are considered as the main causes of leakage problems. Abu Baara dam set in operationin winter 1988, where it filled up with water for thefirsttime.An intensive leakage wasappearedthrough the filling of the dam such as the water were flowingfrom some boreholes drilledbehindthedam body, and the water level in the lake was severely decreasing. This phenomenonhas been repeatedinseveralsubsequentseasonsin particularly at certain storagelevelsin the lake. Afterward, the Directorate ofLandReclamation

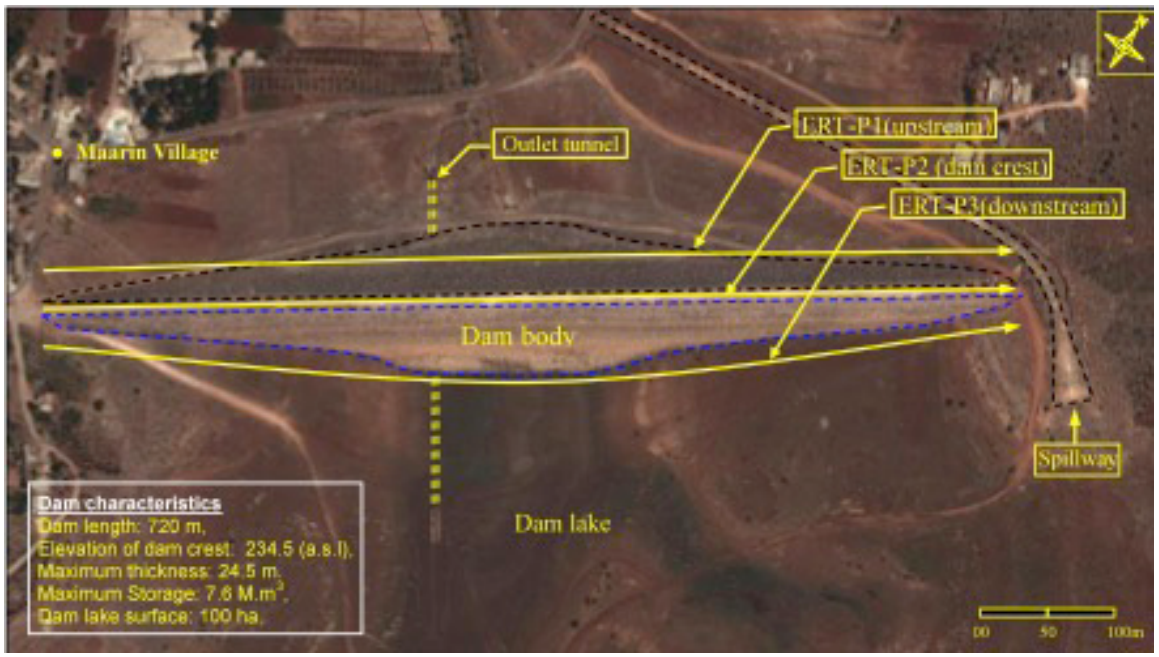

Figure 2. Locations of the ERT profiles carried out in Abu Baara earthen dam (Google Earth).

implementedsome geoelectrical surveys (VES) in the lake and on the right bank of the dam. Al-Diab (2008) carried out a horizontal profiling and SP surveys behind the dam body and on the banks ofthe lake. The results of those surveys clearly showedthe presence of an intersectionof two faults close to the main axis of the dam and some SP anomalies in certain locations around the dam. Nevertheless, the faulted area has sealed by a clayey layer of several meters thick, but the leakage processes still increasing and ongoing especially at high water levels. Thismay posea threat tothe stability and safety ofthe damin the future.

A geophysical survey using electrical resistivity tomography ERT and traditional VES soundings were therefore proposed in orderto characterize in detail the substructure bedrock close and beneath the Abu Baara dam body. Such a survey helps in delineating the probable zones of leakage paths through carrying out a number of ERT profiles in up and downstream sides as well as on dam crest.

Methodology and Materials

2D Electrical Resistivity Tomography (ERT)

Traditionally, the direct-current (DC) electrical survey is used to determine the subsurface resistivity distribution by measuring the electrical potential difference between a pair of potential electrodes M and N, as shown in Figure 3. on the ground surface with a current applied through a pair of current electrodes A and B. The apparent resistivity ρ_a in Ohm.m (Ω.m) is then computed from Ohm's law:

$$\rho_\alpha = k(\Delta v / I)$$

Where k is a geometric constant that depends only on the reciprocal positions of the current and potential electrodes; Δv is the measured potential difference in mV; and I is the applied electric current in mA.

Recent developments in DC technology allow automatic measurements, by switching the current and potential electrodes between a series of equally spaced electrodes laid out along a profile (Figure 3). This allows a dense sampling of subsurface resistivity variation at shallow depth within a short amount of time.

Multi-electrode resistivity survey is a combinational technique of profiling and sounding involving a number of electrodes with a fixed inter-electrode spacing. With the multi-electrode survey one can get lateral as well as the vertical information of the shallow subsurface.The measured apparent resistivity is converted into true resistivity using inversion software in order to produce the 2D resistivity cross-section image (Tomogram). The output from the inversion software displays the

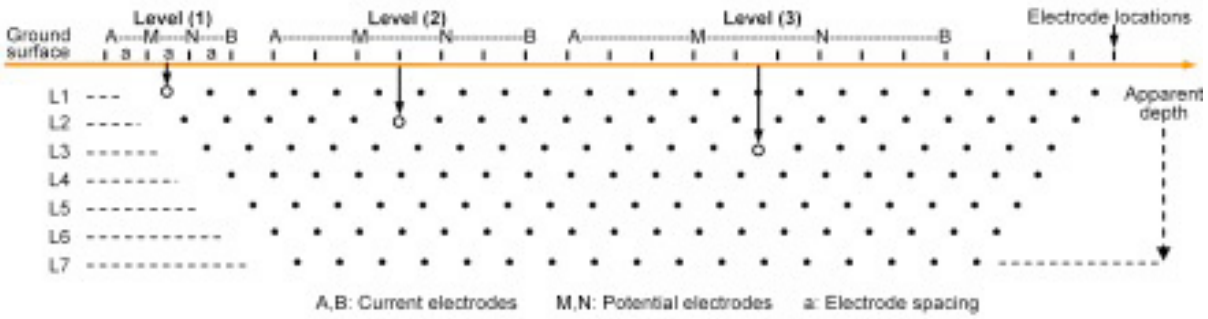

Figure 3. Electrical resistivity tomography configuration.Increasing the distances between current electrodes implies a deep penetration depth.

inverse model resistivity section, which could be thereafter treated geologically point of view.

An electrical resistivity tomography survey (ERT) was carried out in Abu Baara dam site to obtain a comprehensible imageof the geological substructure close and beneath the dam body. The resistivity-meter Syscal Switch-72 was used to acquirethe field ERT measurements. The instrument is modern and equipped with control unit and four multi-swatches cable bobbins to connect 72 electrodes at once with maximum inter-electrodes spacing of 5m.Seventy-twoelectrodes were instilled in a straight line at the selected profile in the study areaaccording to the selected inter-electrodes step. The measurement operation is performed depending on a basis of special mathematical sequence prepared in advance using special software, where the configuration and the interval between the electrodes are selected. The main sequence has maximum length of 360m with an electrode spacing of 5m. In the case where the measuring profile is longer than the main sequence (more than 360m), it is necessary to use a Roll-Along Sequence, compatible with the standard sequence in term of configuration and the inter-electrodes spacing, to end the profile.

The Wenner-Schlumberger array has been purposely applied in the present project work. The advantages of such a configuration over other geoelectrical arrays, such as dipole-dipole or Wenner or Schlumberger,are its reliable stability and itsability to detect horizontal and vertical subsurface features. Moreover,the use of Wenner-Schlumberger configuration provides a good signal/noise ratio for the measurements, and permits getting full density of data from different levels of depth. (Dahlin and Zhou, 2004; Candansayar, 2008). According to the configuration applied in this work with 72 implemented electrodes, the sequence of measurementsincludes therefore 759 measured points, distributed on 16 depth levels.In addition, 304 points are added for each applied roll-along sequence. The collected data are automatically stored in the instrument's memory to be available later for quantitative treatment and interpretation.

ThreeERT profilesof 715m length for each one wereexecuted in Abu Baara dam site (Figure 2): the first one wasin upstream side (behind the dam body), the second at the top of the dam's crest and the third in downstream side. These profiles are straight and parallel to the dam body.It is worth mentioningthat thefield measurements of the ERT profiles were carried outthrough the summer season where the dam'slake was dry andcompletely empty of water. Additionally, a topographical survey wasalso carried out for each profile using a GPS devise with UTM projection.

Inverse Slope Method (ISM)

This method is widely practiced for the estimation of various parameter layers in 1D resistivity surveys(Narayan and Ramanujachary, 1967). Using the *ISM*, the field Schlumberger data are plotted on a simple linear graph paper for generating of a straight line segment by joining various points. The values of the inverse resistance ($AB/2\rho_a$) areplotted against the electrode separation AB/2. Each line segment represents a distinguished layer and the intersections of the line segments with the multiplication of a factor of 2/3 correspond to the depths to the particular layers. This method allows the real thicknesses and resistivities of the corresponding layers to be obtained. It is recently applied in Syria for solving different complicated geological problems, and proven high performance in comparing with traditional

curve matching technique, (Asfahani, 2016). It is applied in this research for interpreting the nine VES data acquired along profile P1. The maximum electrode current AB used for those VES is of 300 m order, allowing a maximum depth penetration of 50 m approximately to be obtained.

Pichgin and Habibullaev Technique

Pichgin and Habibullaevtechnique is oriented towards interpreting vertical electrical soundings (VES) carried out along a given profile(Pichgin and Habibullaev, 1985). It is the most sophisticated one for delineating the subsurface structural features(Asfahani, 2007; Asfahani, 2011).

The theory behind the Pichgin–Habibullaev technique can be summarized as follows: Suppose two vertical electrical soundings, VES1 and VES2 are performed on either side of a vertical contact. For every given current electrode half-spacing (AB/2), all the resistivity profile curves will be intersected at a point located directly over this vertical contact. The locations of the vertical electrical soundings carried out on a given profile are thereforeplotted on the abscissa, and the corresponding measured apparent resistivities for each given AB/2 are plotted on the ordinate, as shown in Figure 4.

The intersection points of the resistivity curves, which are termed Non-Homogeneity

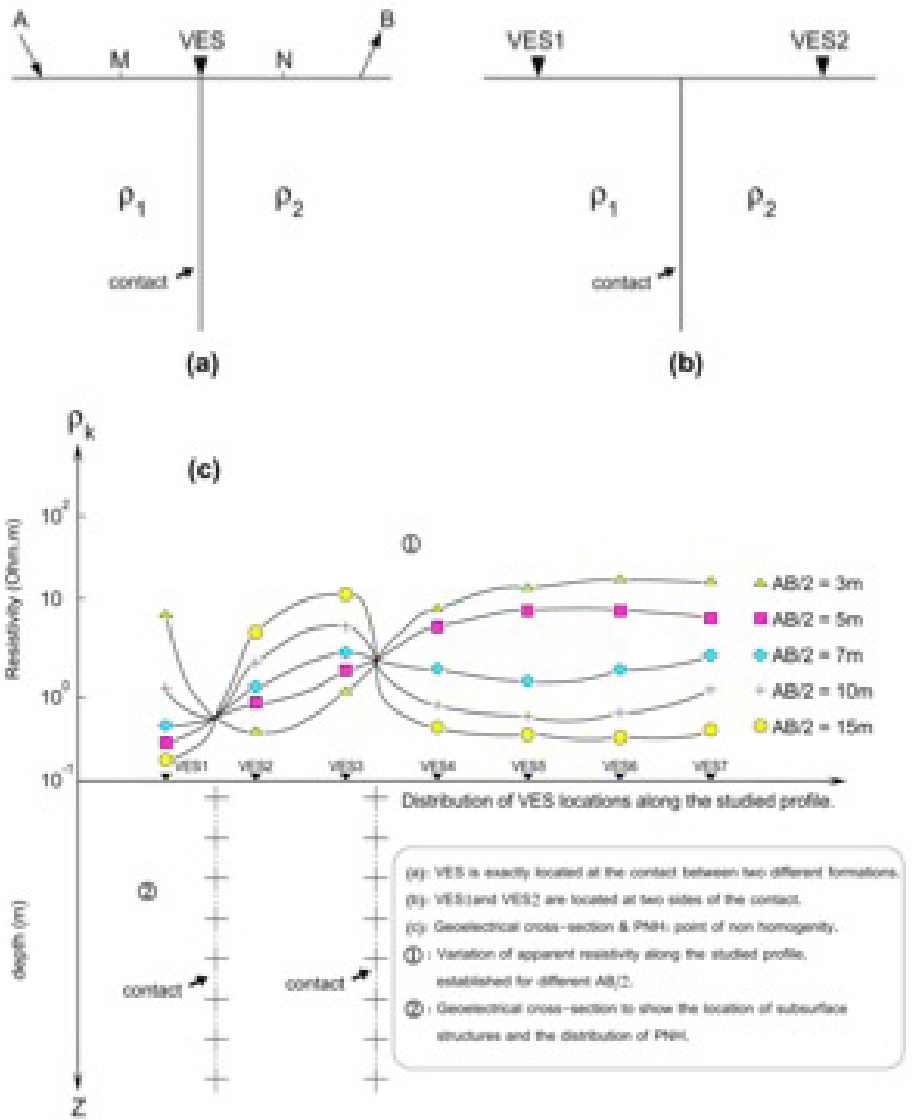

Figure 4. Principal of Pichgin and Habibullaev technique (modified after Asfahani, 2011).

Points (NHP), are plotted on a 2-D (x,z) geological section. The depth (z) of each NHP can be determined from to the following equation:

$$z = [(AB/2)_i + (AB/2)_j] / 2$$

where $(AB/2)_i$ and $(AB/2)_j$ are the half-spacings between the electrodes A and B, at which two horizontal resistivity curves are intersected. The sub fractured zones are determined according to the distribution and interpretation of NHP along the studied profile.

According to this technique, geological interpretation of the NHP is based on the following assumptions:

1. When the NHP are distributed as oblique lines located at shallow depths, they indicate the presence of an inhomogeneous lithologic contact.

2. If they are arranged along oblique lines dipping at an angle exceeding 30° at depth, then they represent a fractured zone.

3. If they are scattered randomly near the surface, then they indicate an homogeneous lithology.

4. If they are arranged in regular forms, then they may reflect certain geological structures, such as synclines, anticlines, or horizontally layered strata.

Those above assumptions have been verified and calibrated through several field examples in Syria, where this technique has proven high performance in solving different field mining, geological and hydrogeological problems(Asfahani and Mohamad, 2002; Asfahani and Radwan, 2007;Asfahani *et al*., 2010). This technique is applied in this paper to interpret the nine VES data acquired along profile P1 in order to extract as maximum as we can the main anomalous structural features, that could be related to the potential leakage zonesin the studied Abu Baara dam.

Results and discussion

The collected ERT field raw data obtained along three profiles P1, P2, and P3were invertedusing RES2DINV inversion software (Loke and Barker, 1996), to characterize the bedrockof the dam's lake substructure. The investigation depth of the ERT configuration applied in this research is of 50 m approximately. The least-squares method including smoothing of model resistivity was used to invert the collected data. The optimization of this method is based on reducing the difference between the measured and calculated apparent resistivity values, where this difference is expressed by Root Mean Squared (RMS) error. The RMS errors in our case study for the inversed geoelectrical sections are ranged between 7 and 12% for 4 and 5 iterations. Increasing the number of iterations for improving RMS errors does not necessarily give reliable and good interpretation geologically point of view.

The inverted model resistivity section represents the true subsurface resistivity values of the investigated geological formations.The ERT profiles were interpreted depending on the available geological information of the study area.

ERT-P1 Profile

The ERT-P1 profile was carried out in upstream side at a distance of 10m from the dam body (Figure 2).Theprofile starts from the western edge of the embankment to end up at the eastern edge traversing a distance of 715m. Figure 5. shows the inverted ERT-P1 geoelectrical section, which can be divided into three principal distinguished blocks:

The first block runs from the beginning of the ERT-P1section to the distanceof 280m. This blockincludes a subsurface layer, of 10m thickness in average, which corresponds to the Quaternary alluvial deposits (Q_3), composed of loams, sands and gravels. The electrical resistivityvalues of these formations are ranging between 50 and 200Ωm. The alluvialdeposits overlay a layer of hard limestone and dolomite Cenomanian-Touronian (Cr_2cm-t) rocks. Thoserocksare characterized byan irregular featuredue to fractures and cracks, which makes them heterogeneous chromatically in the geoelectrical section.The limestone and dolomite rocks have resistivity values of more than 1100Ω.m. These rocks constitute the main hard bedrocks of the dam lake. Otherwise, a distinctive resistive anomaly was noticed between the distance interval60 and 80m of the ERT-P1 section (Figure 5). This anomaly is distinguished by a high electrical resistivity value (up 1200Ωm), which most likely could be associated with probable karstic cavity developed within the limestones bedrock. Evidently, the presence of a possiblecavity constitutes a suitable potential pathway for water leakage occurrence, especially when the water storage reaches high levels in the lake.

The second block extends within the distancebetween 280and 440m of the ERT-P1

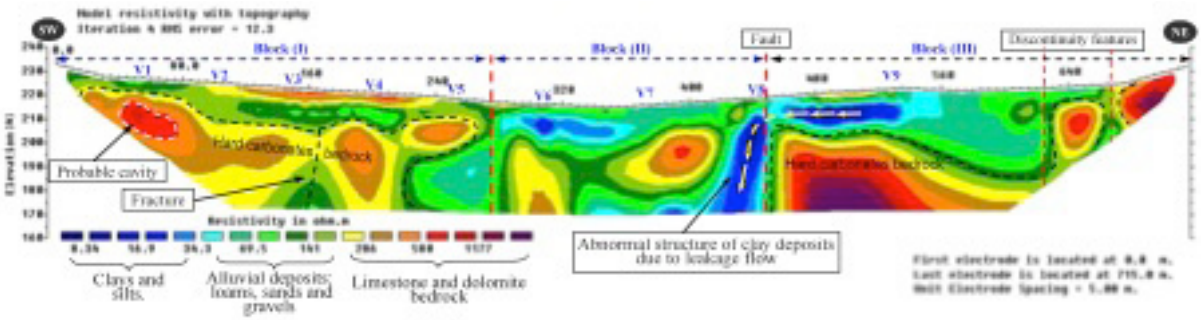

Figure 5. Inverted geoelectrical section of the ERT-P1 profile carried out behind the dambody (upstream site), V: locations of VES.

section. This zone seems well matched with the course of the main valley behind the dam body. Thealluvial deposits are prevailing inthis part of profile and filling the valley with exception the existence of two big scattered masses of limestones. The rightboundary of this block (at the point 440m) is determined by a verticalhard rocks edge.This almost could berelated to the occurrence of a tectonic event such as a fault struck the main valley.Moreover, adistinct anomaly of claywasidentified adjacenttothe mentioned vertical edge; thisabnormal structure maydue to avertical groundwater flow towards the deeper formations. This findingmay indicate to the existence of hydraulic connection between the shallow and the deepgeologic formation. It is obviousthat significant leakagemost likely occurs through this sector along the tectonic contact zone between the alluvium and the limestones rocks.

The third blockextends from the point of 440m to the end of the geoelectrical section (Figure 5). The alluvial deposits thickness rangesbetween 10 to 20m, with resistivity values reach 150Ωm. Those deposits overlay theresistive hard limestonesbedrock(more than 1100Ωm). A discontinuity features were observed in two locationsat the end of the profile (at 630 and 670m), these features are corresponding to fractures in the limestones and dolomites rocks. These discontinuitiesin the bedrock form additional possible pathways for water leakagefrom the dam's lake.

Inverse slope method*ISM* with adapting 1D assumption has been applied in this research for interpreting the nine Schlumberger VES distributed along P1 as shown in Figure 6. True thicknesses and resistivities for the corresponding layers under the study profile P1 have been obtained as shown in Table 1. The most important remark observed while interpreting those nine VES is the presence of negative slopes, indicating high resistivity values in the studied P1 section. Those high values clearly reflect the hard limestone and dolomite rocks existed in the study region (Ponikarov, 1963). The advantages of applying *ISM* is that it easily distinguishes between the different layers under the study VES. The low resistivity values are attributed to the Quaternary alluvial deposits, while the high ones are attributed to the Cretaceous hard limestone and dolomitic rocks. The *ISM* results obtained confirm well those obtained by the ERT measurements and discussed above, particularly the low and high resistivity distributions.

The same nine VES distributed along profile P1 have been interpreted by Pichgin and Habibullaevtechnique explained above. The geometry distribution of the Non Homogeneous Points (NHP) in the 2D (X-Z) section shown in Figure 7 clearly indicates the presence of three main blocks. The central one of more than 150 m wide could be related to a faulted zone, representing the main alluvial valley. The two other right and left blocks are related to the Cenomanian-Turonian limestone and dolomitic rocks. At a detailed level, the NHP clearly showa basinal structure, and the positions of the fractured zones in those two blocks. Their locations are the main leakage points in the study dam under profile P1. It is worth mentioning that the results obtained by interpreting VES data using Pichginand Habibullaevtechnique confirm well those obtained by ERT measurements along Profile P1.

ERT-P2 Profile

This profile wasimplementedalong the dam'screstin parallel with the previous ERT

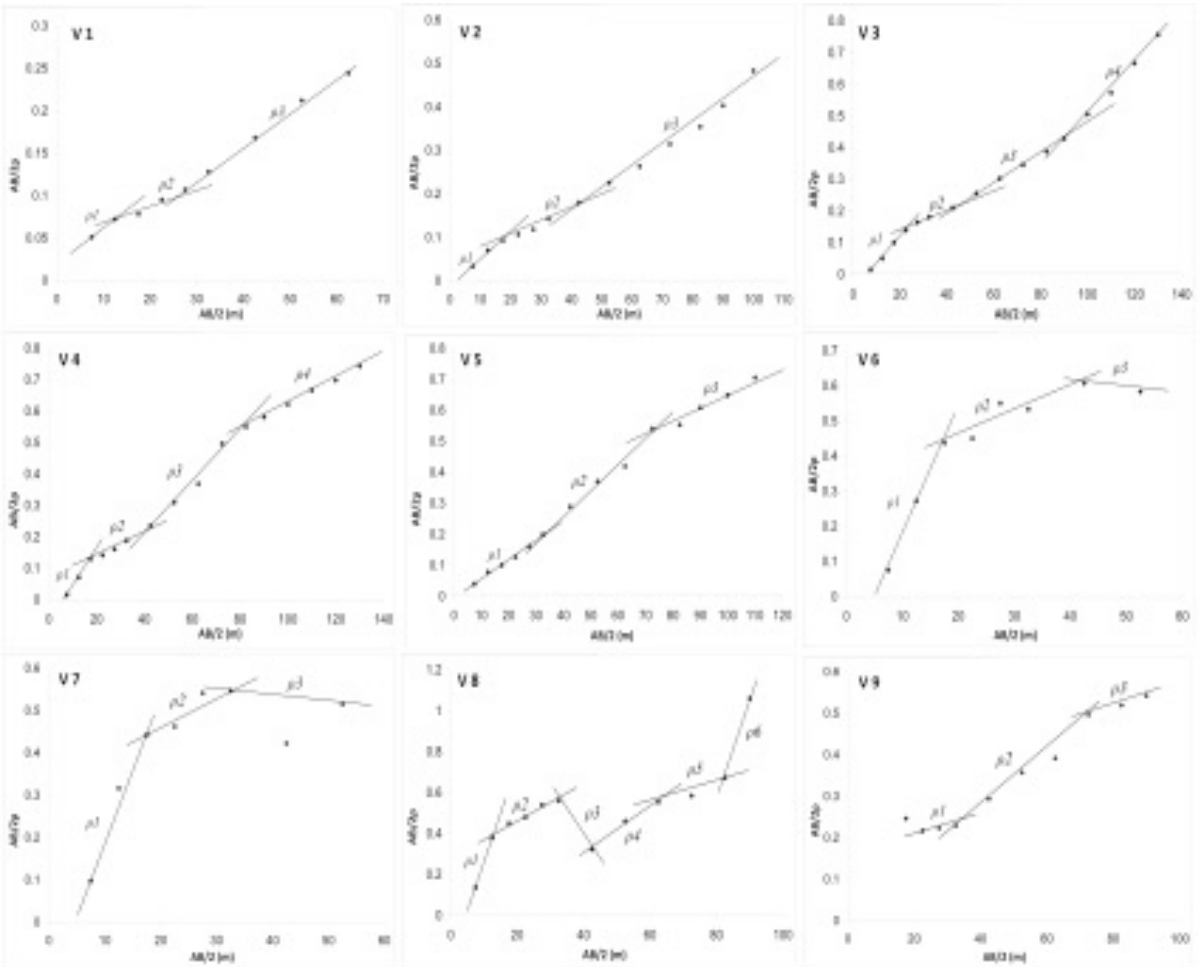

Figure 6. Quantitative 1D interpretation results of nine VES measurements carried out along ERT-P1 profile obtained by *ISM*.

Table 1. ISM Interpretation results of the nine VES distributed along P1.

VES	***Layer resistivity values (Ω.m)***						***Layer thicknesses (m)***				
	ρ1	***ρ2***	***ρ3***	***ρ4***	***ρ5***	***ρ6***	***h1***	***h2***	***h3***	***h4***	***h5***
V1	236	385	227	-	-	-	8	10	--	--	--
V2	161	284	333	-	-	-	12	20	--	--	--
V3	146	435	240	120	-	-	13	9	28	--	--
V4	106	440	187	286	-	-	10	10	29	--	--
V5	167	117	234	-	-	-	24	24	--	--	--
V6	27	167	∞	-	-	-	11	17	--	--	--
V7	29	436	∞	-	-	-	12	10	--	--	--
V8	20	123	∞*	72	169	19	8	12	7	11	16
V9	714	209	181	-	-	-	22	26	--	--	--

*. Very high resistive layer

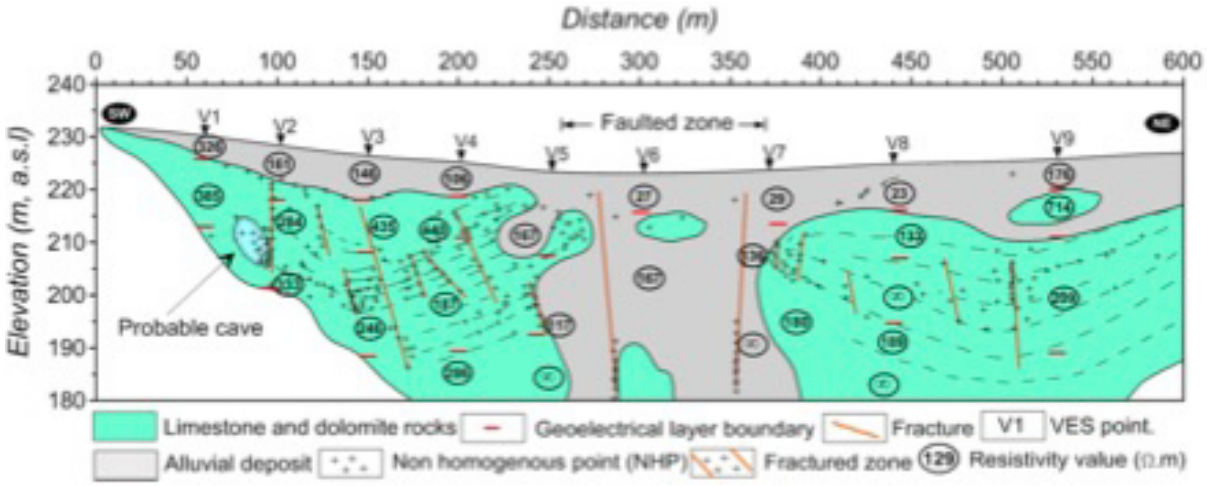

Figure 7. Quantitative interpretation of VES data carried out along ERT-P1 profile by using Pichgin and Habibullaev technique.

profile (Figure 2). This ERT profile, located on the top of dam body, has been carried out by using an electrical driller to dig holes, 4m apart,in the hard asphaltic layer to facilitate the electrodes plantation. The planted electrodes were wetted with salty water and some clay added to ensure a good contact with the underlying soil and to reduce the noise. This profile has length of 716m and 234.5m above sea level (a.s.l) as a constant topographic elevation. Figure 8 shows the inverted geoelectrical section of the ERT-P2 profile, where two main zones can be vertically distinguished; the firstzone is directly related to the clayey core of the dambody, marked by clear blue color in Figure 4. The white dotted line represents the lower boundaries of the dam body with the original land surface of the lake.The resistivity values of thiszone range between 20 and 50 Ωm and the thickness increase towardsthe main valley to reach 25m. The clayey core of the dam seems to be intact and structurallyhomogeneous and the lower boundaries are clear and distinct especially at the contact with the underlying bedrocks.The secondzone of the ERT-P2 section representsthe hard limestones and dolomites bedrock. The general structural of this zone is similar to the ERT-P1 structure. It is consisting of two units of massive carbonates rocks separated by the main valley: the first unitextends from the beginning of the geoelectrical section until the point 320, while the second starts from the point 512 to the end of the section.Bothunits are well differentiated and characterized by high resistivity values.

The central part ofthe second zone extends along the distancebetween 320 and 512m, this part corresponds to the main valley course underneath the dam body.It is believed that the absence of hard bedrock at this part of section could be attributedto dissolution processes of the carbonates rocks by the influence of the water flowing stream, or probably related to tectonic activities such as faults leading to the formation of a subsidence faulted structure filled up later by alluvial deposits (Figure 8). The absence of the bedrock under the central part of the dam body could pose problems in future related to the safety and stability of the dam, particularly when the water reaches high levels during the rainy seasons.Manycracks covering the top of the dam were observed during the fieldworkin the asphaltic layer.This seems to bea negative indicator and must be takeninto consideration through the implementation ofa permanent monitoring programin order to prevent probable failureofthe dam. It is consequently believed that most of the vertical leakage occur sthrough this sector at the contact between alluvial deposits and the hard limestones rocks.

ERT-P3 Profile

The ERT-P3 is implemented in the downstream side adjacent to the dam body (Figure 2). This profile extends as the other profile along 715m of length with inter-electrode spacing of 5m. A topographic survey was performedfor the naturalground surface of the lake along the profile Figure 9 shows the interpretation of the geoelectrical ERT-P3 section, which seems to be structurally similar to theERT-P1 section. It can be therefore also divided into three main blocks differentiated horizontally:

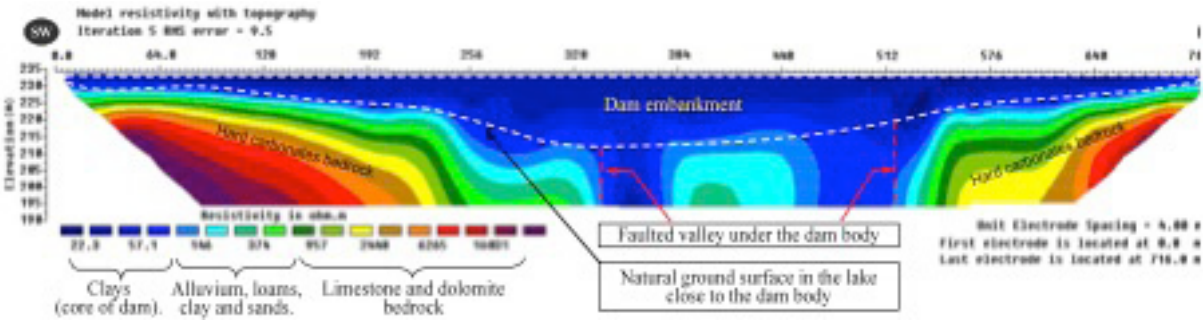

Figure 8. Inverted geoelectrical section of the ERT-P2 profile carried out at the top of the dam body.

The first and thirdblocks are interpreted together because they are composed of the same formations.The first block extends from the beginning of the section to a distance of 300m, while the second one starts from 500m to the end of ERT section.The two blocks include a surface layer of alluvial deposits (Q3). The thickness of these deposits ranges between 1 to 5m in the block(I), andreaches 20mat the third block, sinceit increases towards the main valley. The resistivity values of these deposits vary as mentioned above from 40 to 150Ωm. The alluvial layercovers the bedrock of the hard limestones, which are characterized by high resistivity values (300-1200Ωm), as shownin geoelectrical section. The bedrocks are dipping about 7° (block I) and 15° (block II)towards the main valley. On the other hand, a resistive anomaly is observed between the interval 60 and 90m of the section, this anomaly has been also observed in the ERT-P1 section. It is characterized by a high electrical resistivity value (1200Ωm), which is most likely relatedas mentioned above to karstic cavity within the limestone bedrock. The appearance of this anomaly in the ERT-P1 and ERT-P3 sections at the same location probably indicatesto the presence ofa subsurfacekarstic conduit passing under the dam body at this sector. This subsurface conduit certainly constitutes a suitable pathway for the occurrence of intensive leakage from the lake to outside the dam, especially at the high water storage levels.

Another abnormal structure is also observed between the distances 215-280mof the ERT-P3 section. This structure seems as a void or an opened cavity filled with alluvial deposits (40-150Ωm). Thisvoid or cavity could be resulted by the influence of a tectonic activity followed by erosion and dissolution processes of the limestone and dolomite rocks by the act of water flow effect.Moreover, the discontinuity features identified at the ERT-P1 section is also present in ERT-P3 section at the same location, this features are almost correspond with a fracture extending perpendicular to the dam body within the subsurface carbonate bedrocks. This fracture expands with thedepth, and it is filled with alluvial and claysdeposits of low resistivity (Figure 9). Existences of those fractures constitutes an additional causative of the water leakage from the dam lake.

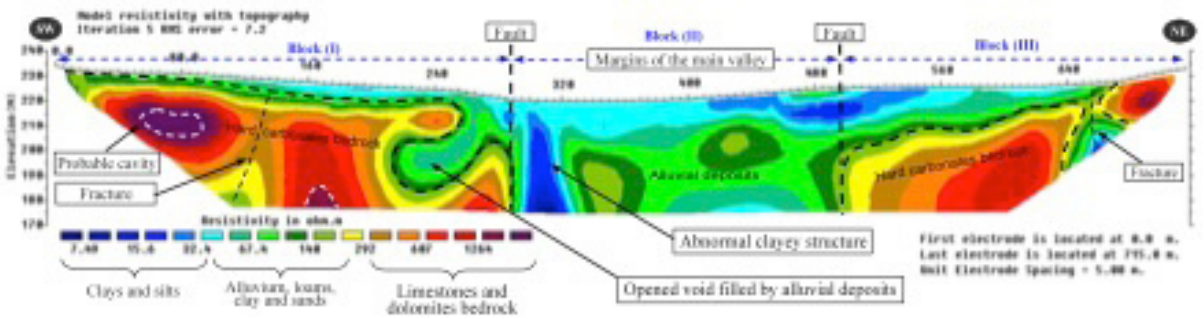

Figure 9. Inverted geoelectrical section of the ERT-P3 profile carried out on downstream site of the dambody.

The second block is stretchingalong the distance from 300 to 500m, and forming the central part of ERT-P3 section. The margins of this sector arein concordance with the main valley and they are delineated by two vertical rockyedges.This part of the section is completely composed of alluvial deposits, where their thicknesses reach more than 50m. Moreover, an abnormal structure of clay, located between 300-320m, is observed at the left edge of this block. This structure represents additional evidence of the presence of a vertical water leakage between the surface and the deep formation.This block is structurally considered as the most significant part of the profile, where many structural anomalies are localized and identified. The filtration and the leakage processes are mostly occurring through this sector. The table (2) globalizes the resistivity values for the different subsurface detected structures obtained from the inversed ERT sections.

A global structural comparison between the geoelectrical ERT sections of the three profilesis illustrated in Figure 10. The general structure of these sections seems to be similarand they are composed of three distinct structural blocks. A remarkable faulted zone can be traced within the interval 300 to 500m of the ERT sections. This zone is compatible with the main valley. Moreover, a karstic cavity located at the beginning ofthe ERT sections can be observed as well as the presence of discontinuity features at the end of the sections.It is worth mentioning, that many field observations have been noted during the implementation of the field measurements,which point to the role of the tectonic activity and other karstic features in the leakage processes. Figure 11 shows some of theses features, where small sinkhole of more than 50 cm of diameter and a large fracture extended for more than 200m parallel to the dam lake marginare observed in many places throughout the lake and behind the dam body.

Table 2. globalizes the resistivity values of the different detected structures obtained from the inversed ERT sections.

Detected features or structure	***Resistivity values range (Ω.m)***
Clays and silts	5 - 20
Alluvial deposits	40 - 120
Limestone and dolomites rocks	400 - 1200
Abnormal clayey structure	5 - 10
Dam embankment	20 - 40

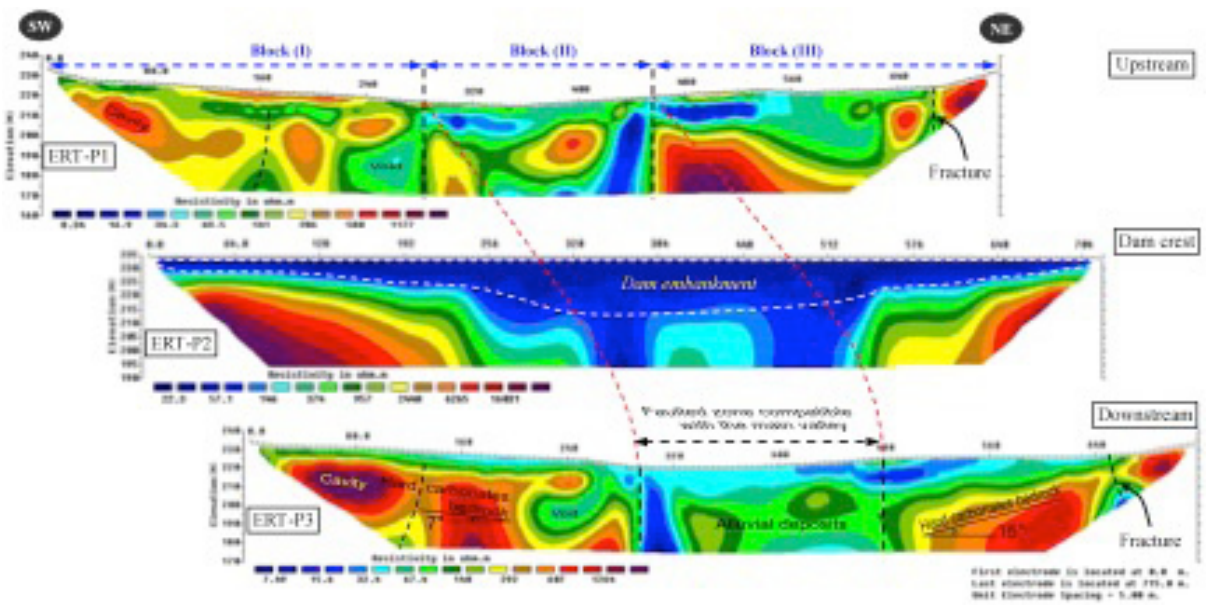

Figure 10. Comparison between the general structure of the inverted geoelectrical ERT profiles carried out in upstream, dam crest and downstream of Abu Baara dam body.

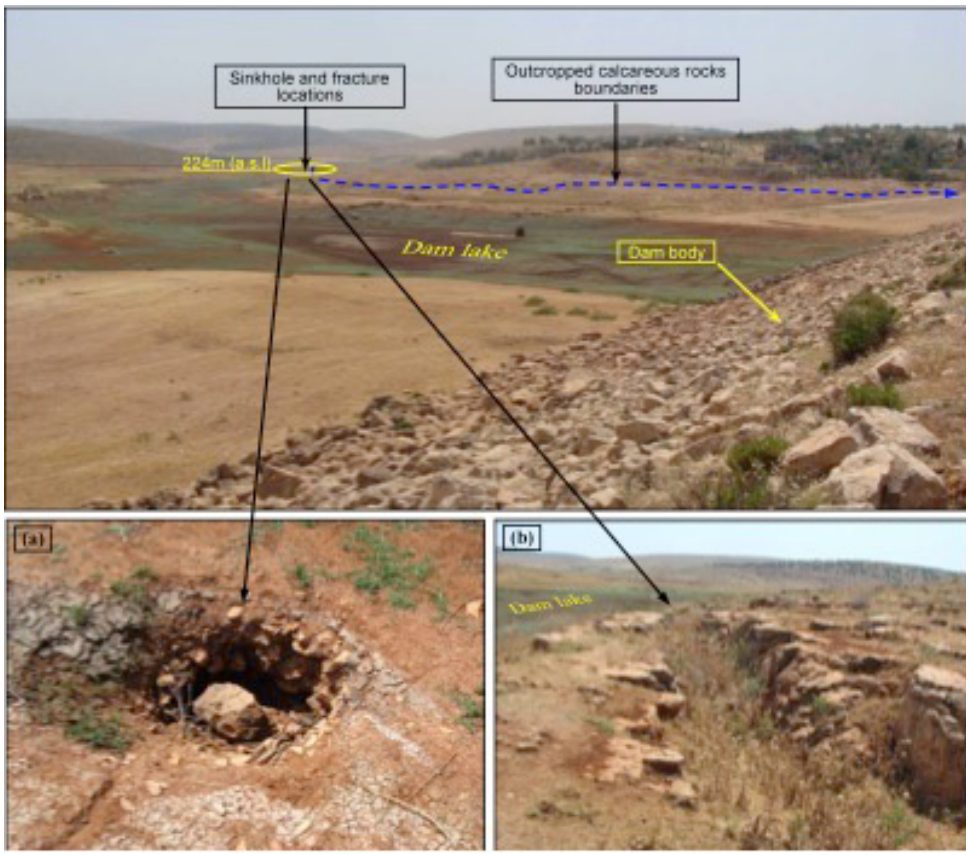

Figure 11. Locations of some leakage features observed at the right bank of Abu Baara dam lake, (a): one of the sinkholes which is located nearby the limestone and dolomite rocks boundary (more than 50cm of diameter), (b): a large fracture of 2-3 depth extends for more than 200m in parallel with the dam lake margin.

Conclusion

An integrated geophysical approach, including different ERT and VES techniques with their specific interpretations is proposed and applied in Abu Baara earthen dam in Northern Syria. The competence and the performance of this approach is proven through the treated case study for solving hydrogeological problems related to leakages of dams. The use of ERT as the main technique in this approach proved also its performance in outlining some critical subsurface geological features such as faults, fractures and cavities. The three inverted ERT sections P1, P2, and P3 discussed in this paper clearly showed three distinct structural blocks: The first and third blocks are consisting of surface alluvial layer composed of loams, sands and gravels covering a hard fractured limestone and dolomite bedrock. The second central block coincides with the course of Abu Baara stream and could be related to a faulted structure that completely filled by more than 50m of alluvial deposits. The presence of this thick structure is considered as one of the main responsible causes of the vertical leakage component occurring through the contact zone between the hard fractured carbonate rocks and the alluvial deposits in the dam lake. Additional geological, tectonic and karstic features such as fractures, faults and cavities have been identified within the underlain carbonates bedrock, which constitutes the major geological formations of dam's lake floor. Those anomalous features localized and delineated by the inverted ERT and Pichginand Habibullaev techniques represent additional potential pathways of water leakage from the dam.

The absence of the hard bedrock underneath the dam body could be asource ofrisk to the safetyand stability of thedam, where some cracks have been observedin theasphaltic layer covering the top of the dam embankment. A permanent monitoring program should be therefore maintained to provide the precaution before the failure of the dam especially during the heavyrainstorms, which characterizethe regionand lead toa sudden increase inwater

levelsin the dam. The proposed approach with its different geophysical techniques contributes efficacy in solving different subsurface hydrogeological problems, such as the one treated in this paper. It could be easily practiced in other similar dams suffering from leakage's problems.

Acknowledgment

The authors would like to thankProfessor I. Othman, Director General of the atomic energy commission of Syria (AECS) for his encouragement and constant support.

References

Al-Diab, S., 2008. Report of geophysical investigations executed under the technical conditions proposed by EDF to estimate the technical situation of Abu Baara dam, 30pp (intern report).

Al-Fares, W., 2011. Contribution of the geophysical methods in characterizing the water leakage in Afamia B dam, Syria. Journal of Applied Geophysics, 75, 464-471.

AlSaigh, N.H., Mohammed, Z.S. and Dahham, M.S. 1994. Detection of water leakage from dams by self-potential method. Engineering Geology, 37, 2, 115-121.

Asfahani, J. and Radwan, Y., 2007. Tectonic Evolution and Hydrogeological Characteristics of the KhanaserValley, Northern Syria, Derived from the Interpretation of Vertical Electrical Soundings. Pures and Applied Geophysics, 164, 2291-2311

Asfahani, J., 2007, Electrical earth resistivity surveying for delineating the characteristics of ground water in semiarid region in Khanaser Valley, Northern Syria. Hydrological Processes, 21, 1085–1097.

Asfahani, J., 2010. Geophysical Case Study of Shallow and Deep Structures Based on Traditional and Modified Interpretation Methods: Application to Tectonic Studies and Mineral Exploration. Exploration and Mining Geology, 19, 3-4, 117-134.

Asfahani, J., 2016. Inverse slope method for interpreting vertical electrical soundings in sedimentary phosphatic environments in the Al-Sharquieh mine, Syria. CIM Journal, 7, 2, 93-104.

Asfahani, J.,Radwan, Y. and Layyous, I., 2010. Integrated geophysical and morphotectonic Survey of the inpact of extensional tectonics on the Qastoon dam, Northwestern Syria. Pures and applied Geophysics, 167, 323-338.

Bedrosian, P.A., Burton, B.L., Powers, M.H., Minsley, B.J., Phillips, J.D., Hunter, L.E., 2012. Geophysical investigations of geology and structure at the Martis Creek Dam, Truckee, California. Journal of Applied Geophysics, 77, 7-20.

Boleve, A., Janod, F., Revil, A., Lafon, A. and Fry J., 2011. Localization and quantification of leakages in dams using time-lapse self-potential measurements associated with salt tracer injection. Journal of Hydrology, 403, 242-252.

Brew, G., 2001. Tectonic evolution of Syria interpreted from integrated geophysical and geological analysis. PhD dissertation at Cornell University, USA, pp. 322.

Candansayar, M.E., 2008. Two-dimensional individual and joint inversion of three and four-electrode array dc resistivity data. Journal of Geophysics and Engineering, 5, 290-300.

Cho, I.K., Yeom, J.Y., 2007. Crossline resistivity tomography for the delineation of anomalous seepage pathways in an embankment dam. Geophysics 72, 31-38.

Dahlin, T., Zhou, B., 2004. A numerical comparison of 2-D resistivity imaging with 10 electrode arrays. Geophysical Prospecting, 52, 379-398.

Devyatkin, E.V., Dodonov, A.E., Sharkov, E.V., Zykin, V.S., Simakova, A.N., Khatib, K. and Nseir, H., 1997. The El-Ghab rift depression in Syria: its structure, stratigraphy, and history of development. Stratigraphy and Geological Correlation, 5, 4, 362-374.

Gomez, F., Khawlie, M., Tabet, C., Darkal, A.N., Khair, K., Barazangi, M., 2006. Late Cenozoic uplift along the northern Dead Sea transform in Lebanon and Syria. Earth and Planetary Science Letters, 241, 913- 931.

Hamade, S. and Tabet, C., 2013. The impacts of climate change and human activities on water resources availability in the Orontes Watershed: Case of the Ghab region in Syria. Journal of Water Sustainability, 3, 1, 45-59.

Ikard, S.J., Revil, A., Schmutz, M., Karaoulis, M., Jardani, A. and Mooney, M., 2014 Characterization of focused seepage through

an earthfill dam using geoelectrical methods. Ground Water, 52, 6, 952-965.

Johansson, S. and Dahlin, T., 1996. Seepage monitoring in an earth dam by repeated resistivity measurements. European Journal of Engineering and Geophysics, 1, 229-247.

Loke, M.H. and Barker, R.D., 1996. Rapid least-square inversion of apparent resistivity pseudo-section by a quasi-Newton method. Geophysical Prospecting, 44, 131-152.

Narayan, P.V.S. and Ramanujachary, K.R., 1967. An inverse slope method determining absolute resistivity. Geophysics 32, 1036-1040.

Oh, S. and Sun, C.G., 2008. Combined analysis of electrical resistivity and geotechnical SPT blow counts for the safety assessment of fill dam. Environmental Geology, 54, 31-42.

Osazuwa1, I.B. and Chii, C.E., 2009. A two-dimensional electrical resistivity imaging of an earth dam, Zaria, Nigeria, Journal of Environmental Hydrology, 17, 28,1-8.

Panthulu, T.V., Krishnaiah, C., Shirke, J.M., 2001. Detection of seepage paths in earth dams using self-potential and electrical resistivity methods. Engineering Geology, 59, 281-295.

Pichgin, N.T. and Habibullaev I.K.H., 1985. Methodological Recommendations in studying geo-tectonic conditions of vertical electrical soundings data with application of EC computer for solving hydrogeological and geo-engineering problems, Tashkend (in Russian).

Ponikarov, V., 1963. The geological map of Syria, Hama-Latheqieh sheet, scale 1:1200, 000, V.O. Technoexport. Ministry of Industry, Damascus, Syria.

Rozycki, A., Fonticiella, J.M.R. and Cuadra, A., 2006. Detection and evaluation of horizontal fractures in earth dams using self-potential method. Engineering Geology, 82, 145-153.

Seaton, W.J. and Burbey, T.J., 2002. Evaluation of two-dimensional resistivity methods in a fractured crystalline-rock terrain. Journal of Applied Geophysics, 51, 21-41.

Sjödahl, P., Dahlin, T. and Zhou, B., 2006. 2.5D resistivity modeling of embankment dams to assess Influence from geometry and material properties. Geophysics, 71, 3, 107-114.

Thompson, S., Kulessa, B. and Luckman, A., 2012. Integrated electrical resistivity tomography (ERT) and self-potential (SP) techniques for assessing hydrological processes within glacial lake moraine dams. Journal of Glaciology, 58, 211, 849-858.

Wan, C.F. and Fell, R., 2004. Investigation of rate of erosion of soils in embankment dams. Journal of Geotechnical and Geoenvironmental Engineering, 130, 4, 373-380.

Zhu, J., Currens, J.C. and Dinger, J.S., 2011. Challenges of using electrical resistivity method to locate karst conduits-A field case in the Inner Bluegrass Region, Kentucky. Journal of Applied Geophysics, 75, 523-530.

Geofísica Internacional (2018) 57-4: 239-251

Original paper

GA-optimized neural network for forecasting the geomagnetic storm index

Pedro Vega-Jorquera, Juan A. Lazzús* and Pedro Rojas

Received: October 31, 2017; accepted: March 12, 2018; published on line: October 03, 2018

Resumen

Se desarrolló un método que combina una red neuronal artificial y un algoritmo genético (ANN+GA) con el fin de pronosticar el índice de tiempo de perturbación de tormenta (*Dst*). A partir de esta técnica, la ANN fue optimizada por GA para actualizar los pesos de la ANN y para pronosticar el índice *Dst* a corto plazo de 1 a 6 horas de antelación usando los valores de la serie temporal del índice *Dst* y del índice de electrojet auroral (*AE*). La base de datos utilizada contiene 233,760 datos de índices geomagnéticos por hora desde 00 UT del 01 de enero de 1990 hasta las 23 UT del 31 de agosto de 2016. Se analizaron diferentes topologías de ANN y se seleccionó la arquitectura óptima. Se encontró que el método propuesto ANN+GA puede ser adecuadamente entrenado para pronosticar *Dst* (*t*+1 a *t*+6) con una precisión aceptable (con errores cuadrático medio *RMSE*≤10nT y coeficientes de correlación *R*≥0.9), y que los índices geomagnéticos utilizados tienen efectos influyentes en la buena capacidad de entrenamiento y predicción de la red elegida. Los resultados muestran una buena aproximación entre las variaciones medidas y modeladas de *Dst* tanto en la fase principal como en la fase de recuperación de una tormenta geomagnética.

Palabras clave: Índice Dst, Pronóstico, Tormenta geomagnética, Serie temporal, Red neuronal artificial, Algoritmo genético.

Abstract

A method that combines an artificial neural network and a genetic algorithm (ANN+GA) was developed in order to forecast the disturbance storm time (*Dst*) index. This technique involves optimizing the ANN by GA to update the ANN weights and to forecast the short-term *Dst* index from 1 to 6 hours in advance by using the time series values of the *Dst* and auroral electrojet (*AE*) indices. The database used contains 233,760 hourly geomagnetic indices data from 00 UT on 01 January 1990 to 23 UT on 31 August 2016. Different topologies of ANN were analyzed and the optimum architecture was selected. It emerged that the proposed ANN+GA method can be properly trained for forecasting *Dst* (*t*+1 to *t*+6) with good accuracy (with root mean square errors *RMSE*≤10nT and correlation coefficients *R*≥0.9), and that the utilized geomagnetic indices significantly affect the good training and predicting capabilities of the chosen network. The results show a good agreement between the measured and modeled *Dst* variations in both the main and recovery phases of a geomagnetic storm.

Key words: Dst index, Forecast, Geomagnetic storm, Time series, Artificial neural network, Genetic algorithm.

P. Vega-Jorquera
P. Rojas
J. A. Lazzús*
Departamento de Física y Astronomía
Universidad de La Serena
Casilla 554, La Serena, Chile

J. A. Lazzús*
Instituto de Investigación Multidisciplinario
en Ciencias y Tecnología
Universidad de La Serena
Casilla 554, La Serena, Chile.
Corresponding author: jlazzus@dfuls.cl

Introduction

Geomagnetic storms are perturbations on the Earth's magnetic field caused by the southward component of the interplanetary magnetic field (IMF). They can last from a few hours to several days (Gonzalez *et al*., 1999). This magnetic field orientation allows magnetic reconnection (Akasofu, 1981) and energy transfer from the solar wind to the Earth's magnetosphere causing a depression of the Earth's magnetic field horizontal (H) component due to the diamagnetic effect generated by the azimuthal circulation of particles in the ring current (Gonzalez *et al*., 1994; Echer *et al*., 2008). Thus, a geomagnetic storm can be defined by ground-based low-latitude geomagnetic field horizontal component variations (Gonzalez *et al*., 1994). Based on this definition, the disturbance storm time index (*Dst*) is established as the average of the disturbance variation of the H-component, divided by the average of the cosines of the dipole latitudes at the observatories for normalization to the dipole equator (Sugiura & Kamei, 1991). *Dst* index serves as a good measure of the overall strength of near-Earth electric currents, especially the ring current (Sugiura, 1964) and it is obtained from four selected geomagnetic observatories operating in the equatorial region (Sugiura & Kamei, 1991).

Another index that can register the geomagnetic activity occurring during a storm is the auroral electrojet index. This index measures the global electrojet activity in the auroral zone (Davis & Sugiura, 1966) and is also derived from geomagnetic variations in the H-component observed from selected observatories throughout the auroral zone in the northern hemisphere (Pallocchia *et al*., 2008). The auroral electrojet index is represented by four índices: *AU*, *AL*, *AE* and *AO*. The *AU* and *AL* indices (Davis & Sugiura, 1966), are used to express the strongest current intensity of the eastward and westward auroral electrojets, respectively (Pallocchia *et al*., 2008). The *AE* index defined as *AE=AU-AL* (Davis & Sugiura, 1966) provides an estimate of the overall horizontal current strength, and to some extent, a rough measure of the ionospheric energy losses (Ahn *et al*., 1983), while the *AO* index defined as *AO=(AU+AL)/2* (Davis & Sugiura, 1966) provides a measure of the equivalent zonal current (Menvielle *et al*., 2011).

The mentioned indices have long records that allow statistical studies of the causes of geomagnetic activity and their related phenomena. In other studies, the relationship between the *Dst* and *AE* indices shows that there is a correlation (with a correlation coefficient of 0.87) for these indices during the recovery phase of the geomagnetic storms (Akasofu, 1981; Saba *et al*., 1997). Thus, correlations between the geomagnetic indices and possible drivers provide the basis for its prediction. In this way, different computational tools have been used for this purpose during the past decades, such as artificial neural networks (ANN). Several examples of the application of ANN to forecast the *Dst* index can be reviewed in (Kugblenu *et al*., 1999; Lundstedt, 2005; Sharifi *et al*., 2006; and references therein). Revallo *et al*., (2014) proposed one of the most recent works on this subject. They present a method for forecasting *Dst* index 1-hour ahead using an ANN combined with an analytical model of the solar wind-magnetosphere interaction.

In this work, *Dst* index 1 to 6 hours ahead were forecasted by an ANN using the time series of the past values of *Dst* itself and *AE* index as input parameters. This ANN was optimized with genetic algorithms (GA) to update the ANN weights. A genetic algorithm is an optimization technique based on the evolutionary ideas of natural selection and genetics (Holland, 1975). The algorithm repeatedly modifies a population of individual solutions into a search space by relying on bio-inspired operators such as mutation, crossover, and selection (Davis, 1991). Due to facts, GA may offer significant benefits over the more typical search of optimization algorithms, and it can be used to optimize the update weights process of an ANN with better results than the traditional back-propagation algorithm (Lazzús, 2016). With this, we propose an improved method to forecast the *Dst* variation based on measurements at ground level. As far as we know, no application yet exists for forecasting *Dst* index using a hybrid ANN+GA method, as is presented here.

Neural networks and genetic algorithms

In this study, we utilize of a multilayer feed-forward neural network. This ANN consists of one input layer with *N* inputs, one hidden layer with *q* units and one output layer with *n* outputs. The output of this model can be expressed as (Lazzús, 2016):

$$y_n = f_n\left(\sum_{j=1}^{q} W_{nj} f_j\left(\sum_{i=1}^{N} W_{ji} x_i + B_j\right) + B_n\right) \quad (1)$$

where W_{nj} are the weights between unit j and unit n of the input and hidden layers, W_{ji} are the weights between the hidden layer and the output, and B_j and B_n represent the biases of the hidden and output layer, respectively. The activation functions $f_n(x)$ and $f_j(x)$ are linear or nonlinear. We used one hidden layer with $f_j(x)$ as a tangent hyperbolic nonlinear activation function and $f_n(x)$ as a linear function in the output layer. For a given set of D inputs, we define the root mean square error (*RMSE*) by:

$$RMSE = \sqrt{\frac{\sum_{d=1}^{D}\left(y_d^{real} - y_d^{calc}\right)^2}{D}} \qquad (2)$$

where y^{real} denotes the actually given output and y^{calc} the neural network output. This network was trained to minimize *RMSE*, replacing the gradient descent error by genetic algorithms (GA), and considering that GA have been applied in the optimization of ANN obtaining better results than the commonly used back-propagation algorithm (Lazzús, 2016). Note that, traditional optimization techniques such as back-propagation learning algorithm (BPLA) can determine the number of network parameters too, such as network connection weights, but BPLA is neither able to control the parameter optimizations in the absence of gradient information nor to reduce the problems of trapping of local minima during the convergence process. In contrast, GA is able to solve these problems.

GA was developed by Holland (1975), and based on the natural selection in biological systems. This algorithm uses genetic information to find new search directions into an error surface aided by operators that reflect the nature of the evolutionary process, such as reproduction, crossover, and mutation (Lazzús, 2016).

GA generates a population of individuals, whose characteristics are encoded in a fixed-length bit string by emulating the biological genotype (Davis, 1991). As a parallel to nature, genetic material is swapped between the individuals and mutated to produce offspring, with corresponding changes in their phenotypic performance (Lazzús, 2016). The crossover operator is an analog of the recombination of genetic material as observed in reproduction. Crossover involves splitting the genomic bit-strings of two parents at a given number of locations and then splicing together complementary sections of each parents' bit-string to form the genotype of the new individual. Crossover occurs with a random probability, and the mutation operator simulates natural mutation of DNA. This simply involves flipping bits in the string in a stochastic manner. The mutation should be fairly infrequent and should be applied following crossover (Davis, 1991).

The main differences between GA and other optimization algorithms are: i) only the objective function and the corresponding fitness levels influence the directions of search; ii) it uses probabilistic transition rules, not deterministic ones; and iii) it works in an encoding environment of the parameter set rather than the parameter set itself (Lazzús, 2016).

Database and training

Data sets of geomagnetic *Dst* index and *AE* index were taken from the World Data Center for Geomagnetism of Kyoto (WDC, 2016), and used to train the network. Figure 1 shows the time series used. These series contain 233,760 hourly data indices from 00 UT on 01 January 1990 to 23 UT on 31 August 2016.

A cross-validation method was used to calculate the predictive capabilities of the proposed method. The training set contains 175,320 hourly data points from 00 UT on 01 January 1990 to 23 UT on 31 December 2009, while the prediction set contains 58,440 hourly data points from 00 UT on 01 January 2010 to 23 UT on 31 August 2016. According to the largest decay values of *Dst* index, the storms fall into low (*Dst*>-20nT), medium (-20nT>*Dst*>-50nT), high (-50nT>*Dst*>-100nT), and extreme (*Dst*<-100nT) categories (Jankovičová *et al*., 2002). Table 1 shows the storm ranges for the database used. Here, geomagnetic indices cover a wide range of values, from -422nT to 95nT for the *Dst* index and from 3nT to 3195nT for the *AE* index. Figure 2 shows the hourly data points categorized as geomagnetic events (extreme storms) that contain the training and prediction sets. In this Figure, both sets show a great number of extreme storms with levels of *Dst*<-100nT.

The main problem of the time series study consists on predicting the next value of the series up to a specific time by using the known past values of the series itself (Palit & Popovic, 2005). In our case, the goal of the proposed method is to use the past values of the time series of geomagnetic indices ($t-\tau_b,\ldots,t-1,t$), with $\tau_b=0,1,\ldots,K$, to predict the geomagnetic index $Dst(t+\tau_a)$, with $\tau_a=1,2,\ldots,T$.

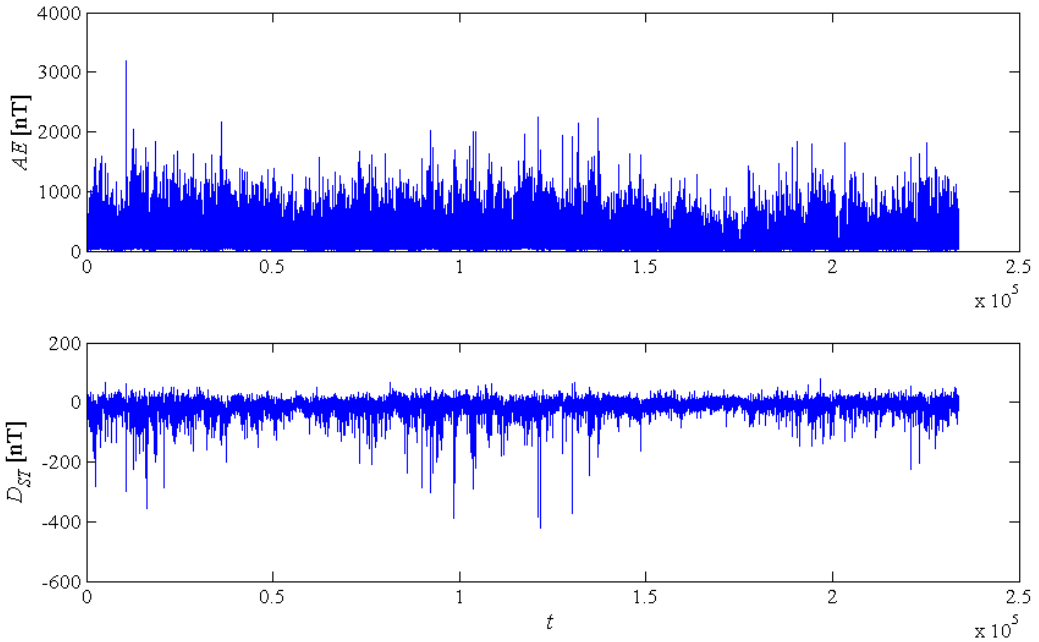

Figure 1. Time series of Dst and AE indices used in this study.

Table 1. Data ranges and geomagnetic storm levels present in the database used.

Data ranges	**Training set**	**Prediction set**
No. data points	233,760	58,440
ΔDst (nT)	-422 to 66	-374 to 95
ΔAE (nT)	5 to 3,195	3 to 2,227
Geomagnetic storm levels (Jankovičová *et al*., 2002)		
Dst>-20nT	117,338	47,007
-20nT>*Dst*>-50nT	46,329	9,774
-50nT>*Dst*>-100nT	9,765	1,519
Dst<-100nT	1,888	140

The inputs are normalized using the following equation:

$$x_i = \left(X_i - X_i^{\min}\right)\frac{2}{X_i^{\max} - X_i^{\min}} - 1 \quad (3)$$

where X_i is the input data i, and X_i^{min} and X_i^{max} are the smallest and largest data values, respectively. Next, the inputs (N) are processed for the ANN neurons as in Eq. (1), and subsequently, GA is used to obtain optimum weights W and biases B for the ANN.

The steps to calculate the optimum weights and biases using GA are as follows (Lazzús, 2016):

1) The initial weights in the ANN are randomly generated (initial population). Then, M-chromosomes are also randomly generated to represent this population, with each chromosome representing all the initial weights and biases in the ANN, which are optimized by GA. Let M be the size of population, i.e. M groups of weights and biases are initialized and encoded into chromosomes as $Z_m(k)=\{W_{ij},W_{nj},B_j,B_n\}$, with m=1,…, M, and

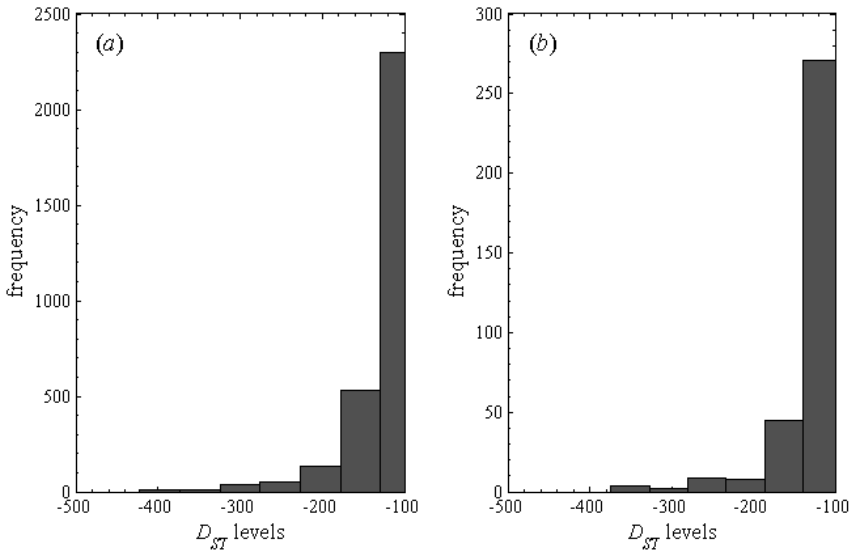

Figure 2. Histograms of main geomagnetic storms. (a) Dst levels for the training set, and (b) Dst levels for the prediction set.

they are randomly distributed in the solution space.

2) The chromosome fitness is evaluated by the performance of the ANN during the training. In this case, fitness function F is defined as $F_m(Z_m(k))=1/(y^{real}-y(k)^{calc})^2$.

3) Fitness function value of each individual in the population is evaluated and the best individual chromosomes are selected for mating. The selection is repeated until the number of individuals in the mating pool is the same as the number of individuals in the population (Che *et al*., 2011). Here, the probability that parental individuals have been selected is given as $p_m=F_m/\Sigma M =_1 F_m$ (Yang *et al*., 2016).

4) Two individuals $Z_u(k)$ and $Z_v(k)$ are selected from the mating pool to generate two child individulas $Z_u(k+1)$ and $Z_v(k+1)$ by two-point crossover, using L as the length of chromosome and a random integer value in interval [1, L] (Yang *et al*., 2016). We used a two-point crossover operator to prevent unreasonable children, two chromosomes break from two points, and thus new chromosomes are generated from the crossover of the first part of parents (Che *et al*., 2011). Thus, two crossover points are selected, the binary string from beginning of chromosome to the first crossover point is copied from one parent, the part from the first to the second crossover point is copied from the second parent and the rest is copied from the first parent (Meng *et al*., 2007).

5) A mutation operator is applied to maintain diversity within the population. Since the initial weights of the ANN could take any values between 0 and 1, the mutation is conducted by switching random genes. The approximate optimal solutions can be found quickly in order to set up the mutation rate as a parameter to control mutation probability (Eiben *et al*., 1999). Here, the mutation strategy for $Z_m(k+1)$ is given as $Z_m(k)$ if $r>r_{mu}$, or $Z_m(k)\times[Z_p(k)+Z_q(k)]$ if $r\leq r_{mu}$, where r is a random number in interval [0,1], and r_{mu} is the mutation factor. Also, $Z_p(k)$ and $Z_q(k)$ are randomly selected from the population and computed as the different gene $[Z_p(k)+Z_q(k)]$. Then, $Z_m(k)\times[Z_p(k)+Z_q(k)]$ is compared with $Z_m(k)$ by item. When $r>r_{mu}$ the item in $Z_m(k)$ remains unchanged, otherwise the item in $Z_m(k)$ mutates to corresponding item in $Z_m(k)\times[Z_p(k)+Z_q(k)]$. Thus, a new individual $Z_m(k+1)$ emerges after comparison (Yang *et al*., 2016).

6) Finally, root mean square error (*RMSE*) is calculated for all the individuals' value. When *RMSE* is less than the preset value, it is considered that the population has converged to the set including the global optimal solution in the ANN+GA (Lazzús, 2016).

Figure 3 shows a block diagram of the ANN+GA method developed for this study. In GA, the number of individuals, the crossover operator, the crossover probability, the mutation operator, and the mutation probability, summarize the main parameters to synchronize for their application in a given problem (Lazzús,

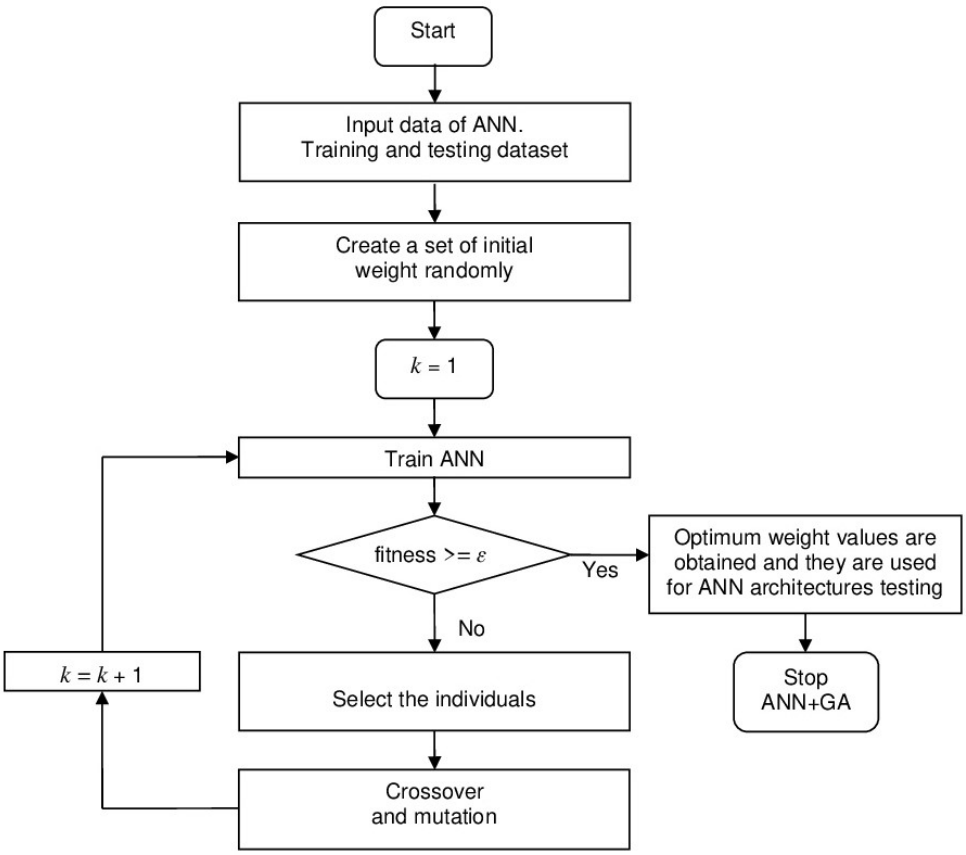

Figure 3. Flow diagram for training of our ANN using GA. Note that training and prediction sets are loaded at the same time by the ANN+GA program, but it must be made clear that only data from the training set were used during the training phase and only prediction data were used in the prediction phase.

Table 2. Parameters used in the hybrid ANN+GA.

Section	Parameter	Value
ANN	NN-type	feed-forward
	Number of hidden layers	1
	Maximum learning epoch	2000
	Transfer function (hidden)	Tansig
	Transfer function (output)	Linear
	Normalization range	[-1, 1]
	Weight range	[-10, 10]
	Bias range	[-5, 5]
	Minimum error	1e-4
GA	Population	10
	Crossover operator	two point
	Crossover rate	0.8
	Mutation operator	binary
	Mutation rate	0.2
	Fitness function	RMSE

2016). For this task, an exhaustive trial-and-error procedure was applied for tuning the GA parameters employed in the ANN. Table 2 shows the selected parameters of ANN+GA. Importantly, these values were obtained from a sub set of examples.

From the above methodology, several network architectures were tested to select the most accurate scheme. The most basic architecture normally used for this type of application involves a neural network consisting of three layers (Lazzús, 2013). The number of hidden neurons needs to be sufficient to ensure that the information contained in the data was adequately represented. No specific approach to determine the number of neurons in the hidden layer (*NHL*) exists, but many posible alternative combinations do. Here, the optimum *NHL* was determined by adding neurons systematically (as a cascade approach) and by evaluating the *RMSE* during the training process (Lazzús, 2016). Thus, we trained 10 different networks for each architecture, from 1 to 30 hidden neurons, totaling 300 NNs (or replications) for each problem ($Dst(t+1)$, $Dst(t+2)$,…, $Dst(t+6)$). In addition, ANN+GA was trained for 2000 epochs (100 generations) for each problem.

Results and discussion

Once the training process was successfully completed and the optimal architecture was determined, the prediction set containing data not used in the training set was evaluated. Table 3 summarizes the best results obtained during the training and prediction processes for forecasting the *Dst* index from 1 to 6 hours in advance.

The results show that the ANN+GA method can forecast the Dst from 1 to 6 hours ahead with a good accuracy by according to the results obtained via $RMSE_{tra}$ and $RMSE_{pre}$. Note that the period from 01 January 1990 to 31 December 2009 (training set) present a greater occurrence of geomagnetic storms with levels of -50nT> *Dst* >-100nT (high) and *Dst* <-100nT (extreme), while for the period used in the prediction set (from 01 January 2010 to 31 August 2016), the occurrence of these types geomagnetic storms are less frequent. Because of this, the prediction *RMSE* were smaller than the training *RMSE*.

As in Table 3, and considering the results obtained during the training and prediction steps ($RMSE_{tra}$ and $RMSE_{pre}$, respectively), deviation increases with the time-ahead. From these results, we observe that our network can forecast only up to 4 hours in advance quite precisely, by considering correlation coefficient *R* greater than 0.9. Note that similar results were obtained by Stepanova & Pérez (2000). For us these results are only related to the processing capabilities of neural networks, and have no relation with the dynamics of the magnetosphere. To clarify, in order to predict each case (from 1 to 6 hours ahead), we trained a new network.

In particular, we focus our analysis on the forecast of $Dst(t+1)$, since for this case we have obtained the best results and can compare them with other available methods. Thus, for this case the best input vector obtained to solve $Dst(t+1)$ was:

$$\begin{aligned} Dst(t+1) = [&Dst(t-4),\ AE(t-4),\\ &Dst(t-3),\ AE(t-3),\\ &Dst(t-2),\ AE(t-2),\\ &Dst(t-1),\ AE(t-1),\\ &Dst(t-0),\ AE(t-0)] \end{aligned} \quad (4)$$

To clarify, for all cases the best input vector was derived from the weights matrices of the network, by using the methodology described

Table 3. Summary of statistical results obtained in the forecast of *Dst* ($t+1$ to $t+6$).

Ahead	Input	NHL	Training set		Prediction set	
			$RMSE_{tra}$	R_{tra}	$RMSE_{pre}$	R_{pre}
t+1	t-4	3	4.63	0.983	3.38	0.980
t+2	t-6	9	7.71	0.952	6.12	0.946
t+3	t-6	12	9.72	0.923	8.63	0.918
t+4	t-8	18	10.31	0.914	10.12	0.901
t+5	t-8	24	12.54	0.889	11.67	0.879
t+6	t-9	27	14.23	0.841	13.72	0.832

above. For *Dst*(*t*+1), these input parameters, we obtained the optimum architecture of 10-3-1, with 10 input neurons corresponding to 5 input parameters for *Dst* index (*t*–4, *t*–3,...,*t*–0) and 5 other input parameters for *AE* index, 3 others neurons in the hidden layer, and one output neuron for *Dst*(*t*+1), as shown in Table 3. Note that considering the structure of this ANN, its length of chromosome was L=10×3+3×1+3+1=37. Also, for this forecast, in Figure 4 appears a comparison between real (solid line) and calculated values (dots) of *Dst*(*t*+1) obtained with the proposed ANN+GA method. Fig. 4*a* shows the comparison during the training step between predicted and real values of *Dst*(*t*+1), from 00 UT on 01 January 1990 to 23 UT on 31 December 2009. Here, *R* was 0.983, while the slope of the curve (*m*) is 0.967 (expected to be 1.0). Fig. 4*b* shows the comparison in the prediction step between predicted and real values of *Dst*(*t*+1), from 00 UT on 01 January 2010 to 23 UT on 31 August 2016). In this case, *R* was 0.979 while *m* was 0.965.

To distinguish the predictive capabilities of ANN+GA between different storm levels, an exhaustive analysis according to storm type for *Dst*(*t*+1), as well as. A comparison between our results and the ones obtained via persistence method was made. Note that the persistence method is usually used in forecast applications. Thus, Table 4 shows the correlation coefficients obtained with the proposed ANN+GA method according to geomagnetic storm levels for *Dst*(*t*+1) versus the results obtained using the persistence method for the same datasets. The results show that the ANN+GA method is a very powerful tool for making forecasts of different geomagnetic storm types. Notably, in the forecast of extreme storms (*Dst*<-100nT), our results were highly accurate with correlation coefficients *R* of 0.945 for the training process and *R* of 0.937 for the prediction step.

As test case to evaluate the predictive accuracy of our ANN+GA method in the forecast of *Dst* index, we used the extreme geomagnetic event of March 2015. The St. Patrick's Day storm on 17 March is categorized as G4-NOAA level that corresponds to an extreme storm (*Dst*<-100nT). This geomagnetic storm serves ou proposed for two main reasons: i) it was the first strongest geomagnetic storm of solar cycle 24, and ii) space weather agencies around the world failed to predict it (Jacobsen & Andalsvik,

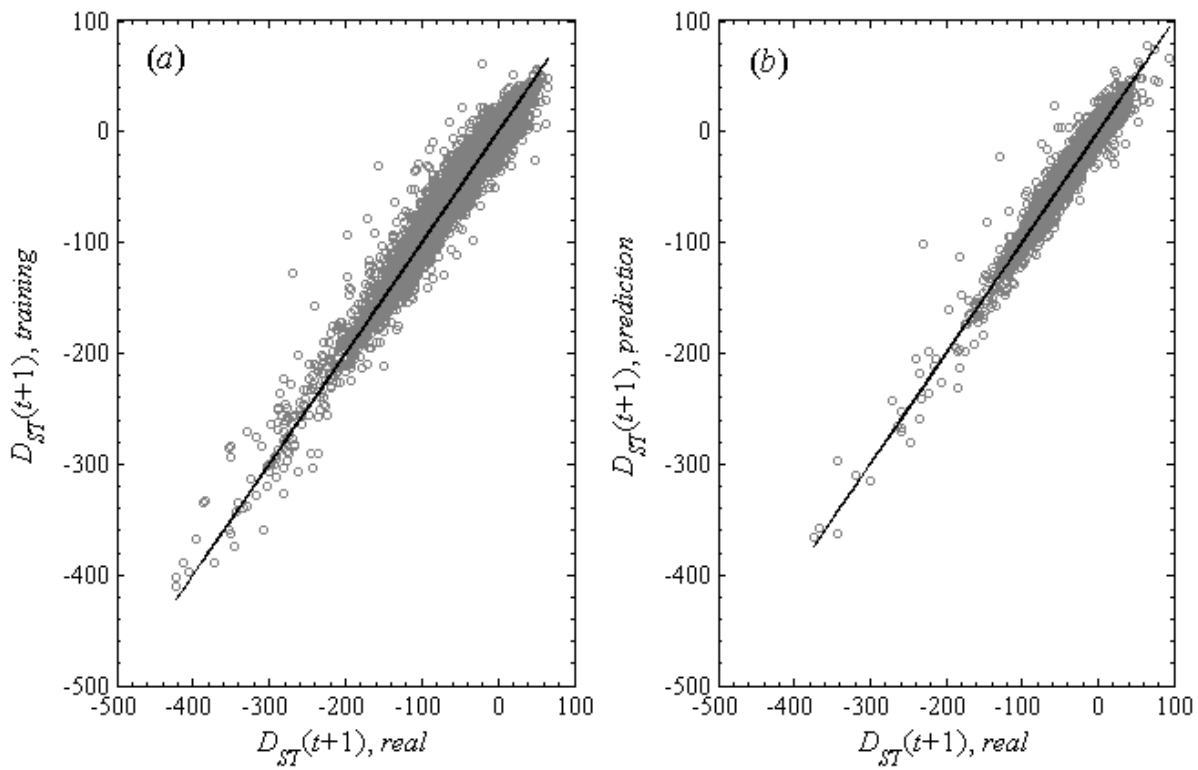

Figure 4. Comparison between real and calculated values of Dst(t+1) using ANN+GA: (a) training set and (b) prediction set.

Table 4. Statistical results obtained with the proposed ANN+GA and the persistence method according to geomagnetic storm levels for *Dst*(*t*+1).

Storm levels (Jankovičová *et al.*, 2002)	Training set		Prediction set	
	R_{pers}	R_{ANN+GA}	R_{pers}	R_{ANN+GA}
Dst>-20nT	0.932	0.938	0.937	0.949
-20nT>*Dst*>-50nT	0.840	0.878	0.838	0.870
-50nT>*Dst*>-100nT	0.802	0.864	0.807	0.842
Dst<-100nT	0.905	0.945	0.863	0.937

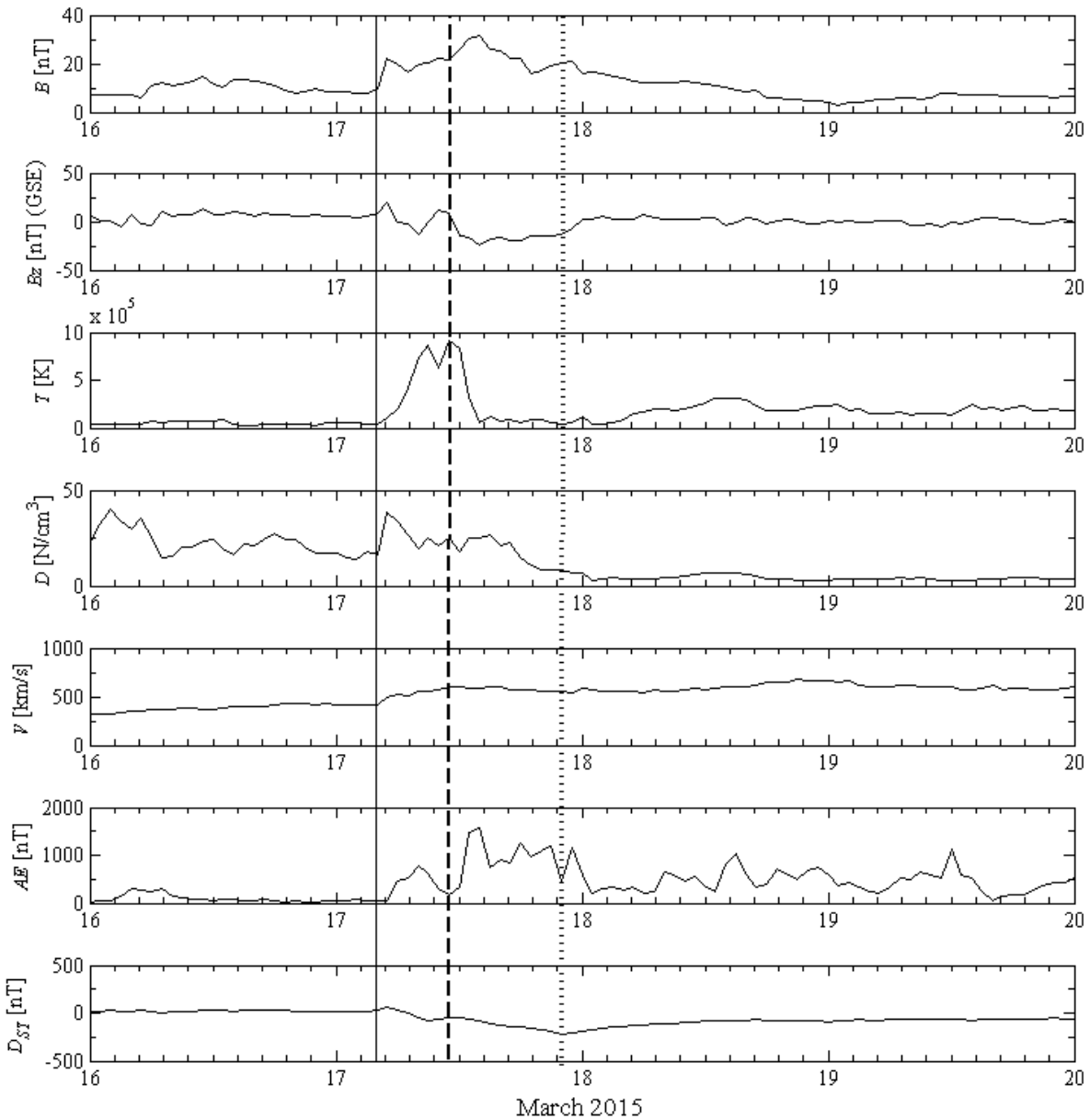

Figure 5. Recorded values of the magnetic field, the solar wind plasma, and the geomagnetic indices during the St. Patrick's Day geomagnetic storm (OMNI, 2016). From top to bottom panels: magnetic field magnitude (B), Bz of the field in GSE, proton temperature (T), proton density (D), flow speed (V), AE index, and Dst index.

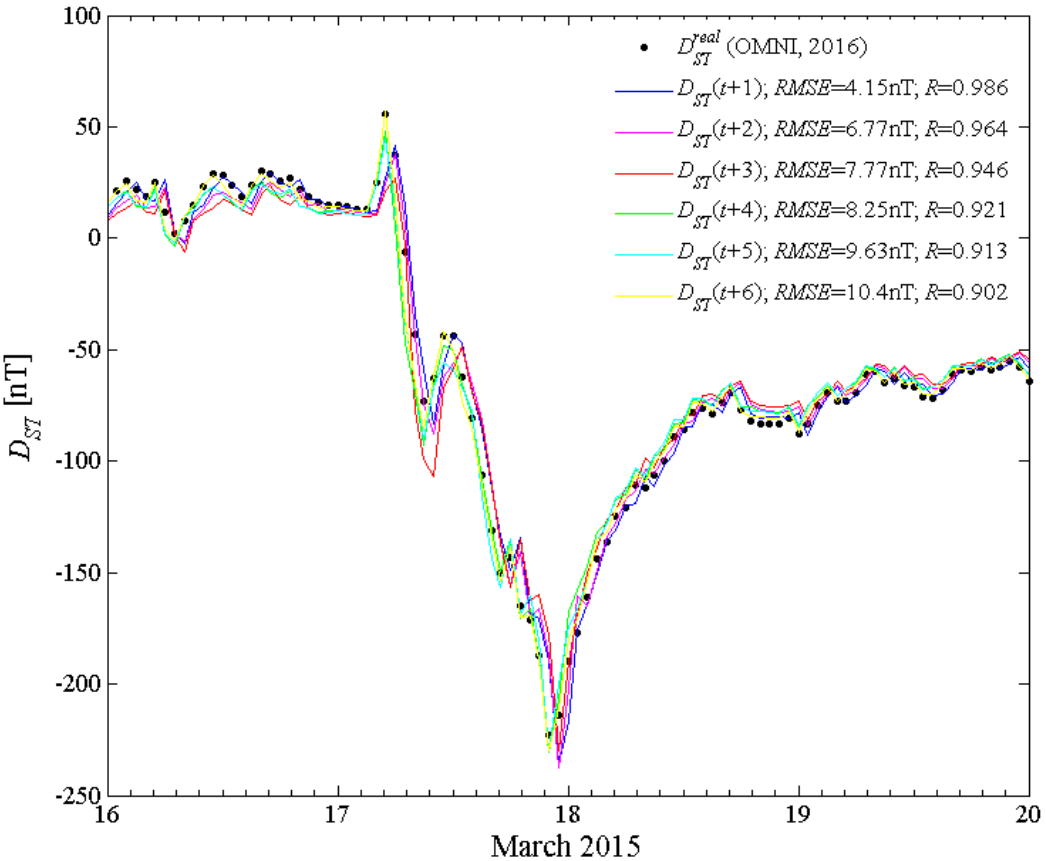

Figure 6. Forecasting of the St. Patrick's Day geomagnetic storm using the proposed ANN+GA method from 1 to 6 hours in advance.

2016). Figure 5 shows the recorded values of the solar wind plasma, the magnetic field, and the geomagnetic indices during the St. Patrick's Day storm from 16-20 March 2015 (OMNI, 2016). The indices contained in this Figure are typically used for monitoring the behavior of a geomagnetic storm. Importantly, the source of this storm must be traced back to a coronal mass ejection (CME) event that occurred on 15 March 2015 at ~2:10 UT and was caused by a partial halo CME with a propagation speed of ~668 [km/s] (Wu *et al*., 2016). Later, an interplanetary (IP) shock arrived to Earth (at ~04:45 UT) causing the sudden storm commencement (Nava *et al*., 2016; Wu *et al*., 2016), as indicated by the solid vertical line in Fig. 5. Next, *Dst* values decreased right after the IMF turned southward (*Dst*=~80nT) and intensified during passage through the region between the IP shock and its driver (Wu *et al*., 2016), as indicated by the dashed vertical line in Fig. 5. Afterwards, it recovered slightly after the IMF turned northward. A few hours later, the IMF turned southward again due to the strongly negative *Bz* associated with a magnetic cloud (MC) and caused a second storm intensification, reaching a *Dst* peak of -223 nT on March 17 (Nava *et al*., 2016; Wu *et al*., 2016), as the dotted vertical line in Figure 5 reveals.

Figure 6 shows the forecast of the *Dst* index during the St. Patrick's Day storm by using our proposed method. As observed, this storm evolves from an abrupt variation of the *Dst* index toward negative values until reaching a minimum value (the main phase of the storm), and starts its recovery until reaching again a *Dst* value close to zero (the recovery phase of the storm). Note that this complete behavior was correctly and quite accurately forecasted by ANN+GA for both phases, where for all forecasted cases of *Dst* (t+1 to t+6), our method obtains $RMSE \leq 10$nT and $R \geq 0.9$ both for the main phase and the recovery phase of that geomagnetic storm (see, Figure

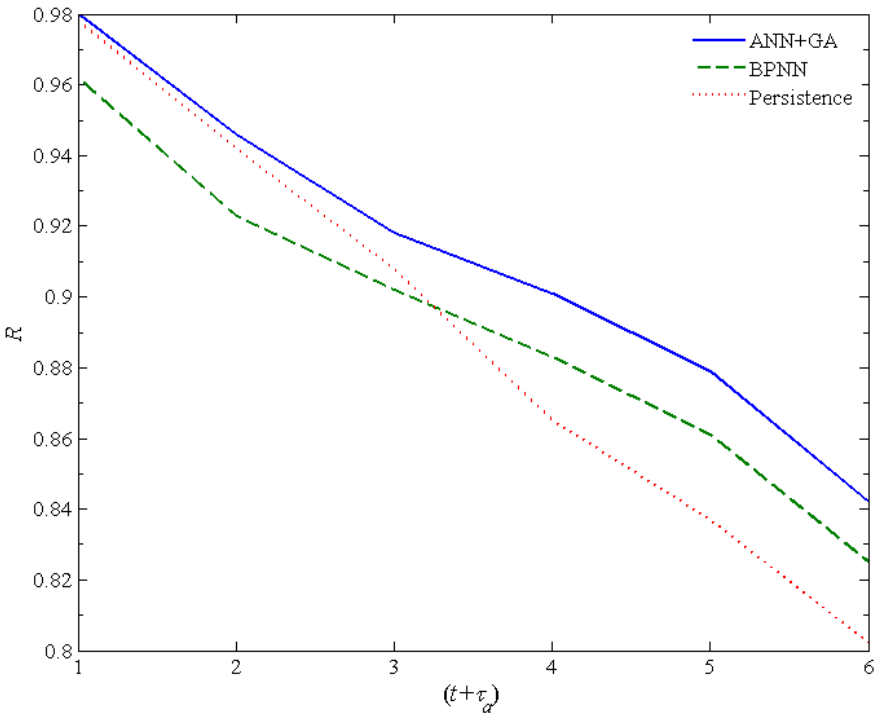

Figure 7. Correlation coeficients (R) obtained by ANN+GA method versus persistence and BPNN methods in the forecast of Dst index from 1 to 6 hours in advance.

6). It should be made clear that data from this storm did not form part of the training set and were completely unknown to the network. This Figure thus also provides a general view of the accuracy and capabilities of the proposed method to forecast the complete behavior of any geomagnetic storm.

On the other hand, various models have been developed to forecast *Dst* index (e.g, in Kugblenu *et al.*, 1999; Lundstedt, 2005; Sharifi *et al.*, 2006; and references therein). However, comparative studies on ANN and the traditional regression approaches for forecasting the *Dst* index have also been conducted, and it has been shown that ANN methodology offers a promising alternative to the traditional approach (Lundstedt, 2005; Stepanova *et al.*, 2005). In this way, a comparison can be made between the proposed ANN+GA method and related methods available in the literatura. For example, Wu & Lundstedt (1996) obtained a *RMSE*=16nT in the prediction of *Dst*(*t*+1) using 97 selected storms. Similarly, Stepanova & Pérez (2000) obtained *R* from 0.95 to 0.72 for a selected set of geomagnetic storms taken from 1983. Later on, Stepanova *et al*. (2005) predicted *Dst*(*t*+1) with *R* from 0.7 to 0.8. Also, Temerin & Li (2006) obtained *RMSE*=6.65nT and *R*=0.914 in the forecast of *Dst*(*t*+1) during the years 1995-2002. Jankovičová *et al.* (2002) present a *R*=0.95 for years 1998-1999. Most recently, Revallo *et al.* (2014) obtained *R* of 0.77 in the forecast of *Dst*(*t*+1) using storms between 1998 to 2005. Meanwhile, our proposed ANN+GA method shows a general accuracy of >97% with *RMSE*=3.4nT and *R*=0.98 in the forecast of *Dst*(*t*+1). It must be mentioned that our results were obtained from different methodologies and databases, and all these results cannot be compared directly with one another. However, from the partial statistical analysis of these different methods, we conclude that our proposed method generates reasonably accurate results. In addition, a comparison was made between the ANN+GA method, and a neural network with standard back-propagation (BPNN) with similar architecture and database. Thus, for example, this BPNN shows a *RMSE* of 5.95, and a *R* of 0.962 in the forecast of *Dst*(*t*+1) with architecture 10-3-1. Figure 7 shows the correlation coeficients obtained by ANN+GA method versus persistence and BPNN methods in the forecast of *Dst* ((*t*+1) to (*t*+6)). This Figure proves that the ANN+GA method can forecast the *Dst* index more accurately than persistence and BPNN methods. Thus, all these results provide a tremendous increase in the accuracy of the forecast of *Dst* index, and

show that both the ANN application and the appropriate selection of the independent input vector were crucial. The innovative aspect introduced in this study pertains to use of a hybrid neural model plus genetic algorithm with only two input variables (*Dst* and *AE*) and a limited number of neurons in the hidden layer for forecasting the *Dst* index.

Conclusions

Based on the results presented in this study, the following main conclusions obtain: i) The proposed ANN+GA method can be properly trained for forecasting the *Dst* index quite accurately ($RMSE \leq 10$nT and $R \geq 0.9$); ii) The geomagnetic indices (*Dst* and *AE*) used have influential effects on the good training and predicting capabilities of the selected network; iii) The ANN+GA method can forecast the Dst index more accurately than persistence and BPNN methods; iv) The low deviations found with the proposed method indicate that it can predict the future values of *Dst* index more accurately than others ANN approach proposed in the literature.

Acknowledgments

The authors thank the Direction of Research and Development of the University of La Serena (DIDULS-PR18141) and the Postgraduate Program of the Department of Physics of the University of La Serena for the special support that made possible the preparation of this paper. Data used were obtained from the World Data Center (WDC) for Geomagnetism of Kyoto, and the OMNI web database of NASA.

References

Ahn B.H., Akasofu S.I., Kamide Y., 1983, The Joule heat production rate and the particle energy injection rate as a function of the geomagnetic indices AE and AL, *J. Geophys. Res.*, 88, 6275-6287, doi: 10.1029/JA088iA08p06275.

Akasofu S.I., 1981, Energy coupling between the solar wind and the magnetosphere, *Space. Sci. Rev.*, 28, 121-190, doi:10.1007/BF00218810.

Che Z.-G., Chiang T.-A., Che Z.-H., 2011, Feed-forward neural networks training: a comparison between genetic algorithm and back-propagation learning algorithm, *Int. J. Innovative Comput.*, 7, 5839-5850.

Davis L., 1991, Handbook of Genetic Algorithms, Van Nostrand Reinhold, New York, USA.

Davis T.N., Sugiura M., 1966, Auroral electrojet activity index AE and its universal time variations, *J. Geophys. Res.*, 71, 785-801, doi: 10.1029/JZ071i003p00785.

Echer E., Gonzalez W.D., Tsurutani B.T., 2008, Interplanetary conditions leading to superintense geomagnetic storms (Dst ≤ -250 nT) during solar cycle 23, *Geophys. Res. Lett.*, 35, L06S03(1)-L06S03(5), doi:10.1029/2007GL031755.

Eiben E., Hinterding R., Michalewicz Z., 1999, Parameter control in evolutionary algorithms, *IEEE Trans. Evolut. Comput.*, 3, 124-141, doi: 10.1109/4235.771166.

Gonzalez W.D., Joselyn J.A., Kamide Y., Kroehl H.W., Rostoker G., Tsurutani B.T., Vasyliunas V.M., 1994, What is a geomagnetic storm?, *J. Geophys. Res.*, 99, 5771-5792, doi:10.1029/93JA02867.

Gonzalez W.D., Tsurutani B.T., Clúa de Gonzalez A.L., 1999, Interplanetary origin of geomagnetic storms, *Space Sci. Rev.*, 88, 529-562, doi:10.1023/A:1005160129098.

Holland J., 1975, Adaptation in Natural and Artificial Systems, University of Michigan Press, Michigan, USA.

Jacobsen K.S., Andalsvik Y.L., 2016, Overview of the 2015 St. Patrick's day storm and its consequences for RTK and PPP positioning in Norway, *J. Space Weather Space Clim.*, 6, A9(1)-A9(12), doi:10.1051/swsc/2016004.

Jankovičová D., Dolinský P., Valach F., Vörös Z., 2002, Neural network-based nonlinear prediction of magnetic storms, *J. Atmos. Sol.-Terr. Phys.*, 64, 651-656, doi:10.1016/S1364-6826(02)00025-1.

Kugblenu S., Taguchi S., Okuzawa T., 1999, Prediction of the geomagnetic storm associated Dst index using an artificial neural network algorithm, *Earth Planet Space*, 51, 307-313, doi:10.1186/BF03352234.

Lazzús J.A., 2013, Neural network-particle swarm modeling to predict thermal properties, *Math. Comput. Model.*, 57, 2408-2418, doi: 10.1016/j.mcm.2012.01.003.

Lazzús J.A., 2016, Estimation of thermal conductivity λ(T,P) of ionic liquids using a neural network optimized with genetic algorithm, *C. R. Chim.*, 19, 332-340, doi: 10.1016/j.crci.2015.09.010.

Lundstedt H., 2005, Progress in space weather predictions and applications, *Adv. Space Res.*, 36, 2516-2523, doi:10.1016/j.asr.2003.09.072.

Meng A., Ye L., Roy D., Padilla P., 2007, Genetic algorithm based multi-agent system applied to test generation, *Comput. Educ.*, 49, 1205-1223, doi: 10.1016/j.compedu.2006.01.012.

Menvielle M., Iyemori T., Marchaudon A., Nosé M., 2011, Geomagnetic Indices. In: Geomagnetic Observations and Models, Ed. Mandea M., Korte M., Springer, New York, USA, pp 183-228.

Nava B., Rodríguez-Zuluaga J., Alazo-Cuartas K., Kashcheyev A., Migoya-Orué Y., Radicella S.M., Amory-Mazaudier C., Fleury R., 2016, Middle- and low-latitude ionosphere response to 2015 St. Patrick's Day geomagnetic storm, *J. Geophys. Res. Space Phys.*, 121, 3421-3438, doi:10.1002/2015JA022299.

OMNI, 2016, Space Physics Data Facility OMNIWeb database, National Aeronautics and Space Administration (NASA), https://omniweb.gsfc.nasa.gov/.

Palit A.K., Popovic D., 2005, Computational Intelligence in Time Series Forecasting Theory and Engineering Applications, Springer-Verlag, London, UK, doi:10.1007/1-1004 84628-184-9.

Pallocchia G., Amata E., Consolini G., Marcucci M.F., Bertello I., 2008, AE index forecast at different time scales through an ANN algorithm based on L1 IMF and plasma measurements, *J. Atmos. Sol.-Terr. Phys.*, 70, 663-668, doi: 10.1016/j.jastp.2007.08.038.

Revallo M., Valach F., Hejda P., Bochníček J., 2014, A neural network Dst index model driven by input time histories of the solar wind-magnetosphere interaction, *J. Atmos. Sol.-Terr. Phys.*, 110-111, 9-14, doi:10.1016/j.jastp.2014.01.011.

Saba M.M.F., Gonzalez W.D., Clúa de Gonzalez A.L., 1997, Relationships between the AE, ap and Dst indices near solar minimum (1974) and at solar maximum (1979), *Ann. Geophys.*, 15, 1265-1270, doi:10.1007/s00585-997-1265-x.

Sharifi J., Araabi B.N., Lucas C., 2006, Multi-step prediction of Dst index using singular spectrum analysis and locally linear neurofuzzy modeling, *Earth Planet Space*, 58, 331-341, doi:10.1186/BF03351929.

Stepanova M. V., Pérez P., 2000, Autoprediction of Dst index using neural network techniques and relationship to the auroral geomagnetic indices, *Geofís. Int.*, 39, 143-146.

Stepanova M., Antonova E., Troshichev O., 2005, Prediction of Dst variations from polar cap indices using time-delay neural network, *J. Atmos. Sol.-Terr. Phys.*, 67, 1658-1664, doi:10.1016/j.jastp.2005.02.027.

Sugiura M., 1964, Hourly values of equatorial Dst for the IGY, *Ann. Int. Geophys. Year*, 35, 9-45.

Sugiura M., Kamei T., 1991, Equatorial DST index 1957-1986, in IAGA Bull. 40, Ed. Berthelier A., Menvielle M., Int. Serv. of Geomagn. Indices Publ. Of., Saint-Maur-des-Fosses, France.

Temerin M., Li X., 2002, A new model for the prediction of Dst on the basis of the solar wind, *J. Geophys. Res.*, 107, SMP31(1)-SMP31(8), doi:10.1029/2001JA007532.

WDC, 2016, World Data Center for Geomagnetism, Kyoto, Japan, http://wdc.kugi.kyoto-u.ac.jp/.

Wu C.-C., Liou K., Lepping R.P., Hutting L., Plunkett S., Howard R.A., Socker D., 2016, The first super geomagnetic storm of solar cycle 24: "The St. Patrick's day event (17 March 2015)", *Earth Planets Space*, 68, 151(1)-151(12), doi:10.1186/s40623-016-0525-y.

Wu J.-G., Lundstedt H., 1996, Prediction of geomagnetic storms from the solar wind data using Elman recurrent neural networks, *Geophys. Res. Lett.*, 23, 319-322, doi:10.1029/96GL00259.

Yang J., Zhao H., Chen X., 2016, Genetic algorithm optimized training for neural network spectrum prediction, 2nd IEEE International Conference on Computer and Communications, IEEE Press, China.

Geofísica Internacional (2018) 57-4: 253-275

Original paper

Atmospheric corrections of the cosmic ray fluxes detected by the Solar Neutron Telescope at the Summit of the Sierra Negra Volcano in Mexico

M. Barrantes*, J. F. Valdés-Galicia, O. Musalem, A. Hurtado, M. Anzorena, R. García, R. Taylor, Y. Muraki, Y. Matsubara, T. Sako, Y. Sasai, N. Hinaro, N. Tateiwa, H. Tsujihara, L. X. González, E. Ortiz, S. Shibata, K. Watanabe, T. Sakai

Received: April 04, 2018; accepted: August 24, 2018; published on line: October 03, 2018

Resumen

Un Telescopio de Neutrones Solares (TNS) fue instalado en la cima del volcán Sierra Negra, Pue., México (19.0º N , 97.3º W, 4580 m sobre el nivel del mar); el cual se encuentra en operación desde el 2004. En este trabajo, utilizamos los valores de la presión barométrica, de la presión dinámica, de la temperatura ambiental y de la humedad relativa obtenidos por una estación meteorológica cercana al TNS, para calcular los coeficientes de corrección atmosféricos para el flujo registrado de rayos cósmicos. Cuando los datos de rayos cósmicos están libres de las variaciones de origen atmosférico, analizamos los perfiles de tiempo observados por el TNS durante seis decrecimientos tipo Forbush seleccionados para el período 2011-2013. Los resultados obtenidos por varios canales de depósito de energía (30,60,90 MeV) son discutidos para establecer la confiabilidad del TNS para este tipo de eventos.

Palabras clave: parámetros atmosféricos, coeficientes de corrección, Decrecimiento Forbush, telescopio de neutrones solares.

M. Barrantes*
J. F. Valdés-Galicia
O.Musalem
A. Hurtado
M.Anzorena
R. García
R. Taylor
Instituto de Geofísica
Universidad Nacional Autónoma de México
Circuito de la Investigación Científica S/N
Av. Universidad 3000
Delegación Coyoacán,
Ciudad de México, C.P. 04510 México
*Corresponding author: marnebasal@gmail.com

M. Barrantes
On leave from: Escuela de Física
Universidad de Costa Rica
San Pedro de Montes de Oca, San José
C.P. 11501 Costa Rica

Y. Muraki
Y. Matsubara
T. Sako
Y. Sasai
N. Hinaro
N. Tateiwa
H. Tsujihara
Institute for Space-Earth Environmental Research
Nagoya University
Furo-cho, Chikusa-ku
Nagoya 464-8601, Japan

L.X. González
SCiESMEX-IGUM
Universidad Nacional Autónoma de México
Antigua carretera a Pátzcuaro 8701
Morelia, Michoacán, C.P. 58190 México

E. Ortiz
Instituto de Ciencias Físicas
Universidad Autónoma de México
Avenida Universidad 2001, Chamilpa
Cuernavaca, Morelos, C.P. 62210 México

S. Shibata
College of Engineering, Chubu University, Kasugai 487-8501, JAPAN.

K. Watanabe
Deparment of Earth and Ocean Sciences
School of Applied Sciences
National Defense Academy of Japan
239-8686, Kanagawa Prefecture
Yokosuka, Hashirimizu, Japan.

T. Sakai
College of Industrial Technologies
Nihon University, Narashino 275-0005
Japan

Abstract

A Solar Neutron Telescope (SNT) was installed at the summit of Sierra Negra volcano, Pue., Mexico (19.0º N, 97.3º W, 4580 m above sea level); it is in operation since 2004. In this work, values of barometric pressure, dynamic pressure, ambient temperature and relative humidity obtained by a meteorological station close to the SNT were used, to calculate the coefficients of atmospheric correction to the registered cosmic ray flux. Once the cosmic ray data are free from variations of atmospheric origin, the time profiles observed by the SNT during five selected Forbush type decreases during the period 2011-2013 were analysed. Results obtained by several energy deposition channels (30, 60, 90 MeV) are discussed to establish the reliability of the SNT for this type of events.

Key words: atmospheric parameters, correction coefficients, Forbush Decrease; Solar neutron yelescope.

1 Introduction

Cosmic rays (galactic and solar) generate particle air showers that are absorbed and attenuated as they travel deeper into the atmosphere. Therefore, mountain detectors are relevant to register high cosmic ray fluxes.

Forbush decreases (FDs) are perhaps the most impressive phenomenon of galactic cosmic rays (GCRs) caused by solar activity. The cosmic ray intensity may have a drastic decrease (up to 20%) in a few hours, however the recovery is slow, lasting typically around seven to ten days. It is one of the extreme manifestations of transient modulation of GCRs, therefore an interesting subject of study to elucidate the mechanisms of solar activity with a recognizable influence in the interplanetary medium. FDs are generally correlated with corotating interaction regions (CIRs), interplanetary shocks or interplanetary coronal mass ejections (ICMEs) originated at the Sun (Subramanian, 2009; Richardson & Cane, 2011; Musalém, 2015).

In most of these cases, an associated plasma is much faster than the normal solar wind (300-800 ms^(-1)) and produces a shock wave, which acts as a magnetic 'sweeper' partially impeding the passage of the cosmic radiation to the region behind it. As the shock wave moves away from the point of observation, its influence diminishes. FDs are usually observed by particle detectors on Earth within shortly before or after the passage of an ICME, a CIR or a shock; the descent in the counting rates takes place in the course of less than 24 hours, as a rule. During the following seven to ten days, the intensity of the cosmic rays returns to normal, this is known as the recovery period of the FDs.

Recent statistical studies on the relationship between characteristics of solar wind disturbances, ICMEs, CIRs and shocks, with properties of FDs (i.e.: Dumbovic *et al*., 2011; Musalém, 2015) revealed that not only the increase in magnetic field strength and fluctuations define the amplitudes of the GCR decrease; the length of time the Earth stays inside the solar wind disturbed region is also important; the recovery phase depends on the magnetic field strength and the size of the disturbance. The deepest FDs are always found to be associated with ICMEs accompanied by a magnetic cloud (Richardson & Cane, 2011; Dumbovic *et al*., 2011). Examining simultaneous observations of FD events by different GCR stations on the Earth's surface remains a subject of interest. Variability in the manifestations of FDs demonstrates that there are still open questions in this field (Okike & Collier, 2011; Pintér *et al*., 2011). FDs are observed mainly by neutron monitors (NMs), but also at higher energies of primary GCRs by muon telescopes or other types of detectors (Braun *et al.*, 2009; Abbrescia, *et al*., 2011; Bertou, 2011; Augusto, *et al*., 2012; Dasso *et al*., 2012; Deggeroni, *et al*., 2013). In this context, the possibility to add the results of a detector of a different design, such as the SNT is a matter of interest in the subject.

The plan of the paper is as follows: In section 2 the influence of the atmosphere on cosmic radiation is briefly described, their interaction with air particles and due to meteorological parameters; In section 3 the main characteristics of the Solar Neutron Telescope at Sierra Negra is shown . The set of data employed in this study, together with the methods used are presented in section 4. Section 5 is dedicated to the presentation of the particular data and the results obtained. An interpretation of the results is given in section 6. Finally, in section 7 ar summary and conclusions are given.

2 Influence of the atmosphere on cosmic radiation

2.1 Interaction of primary cosmic rays with the atmosphere

Galactic cosmic rays (GCR) extend over an enormous range of energies, (106 – 1021 eV). These high-energy particles that come from outer space are mainly protons (90% - hydrogen nuclei, helium nuclei 9% and heavier cores 1%). When primary cosmic radiation enters the atmosphere, everything that happens is the result of its collision with air particles. These collisions may be of two types: with the electronic structure of the atom, or with the nucleus. Since the nucleus is so small, the collision with it is less common, but it involves very large energy changes and these changes are the ones that determine all the formation of secondary cosmic rays.

When a particle of primary cosmic radiation collides with the nucleus of an air molecule, cascades of a large number of secondary particles are produced, mainly pions. The charged pions quickly decay, emitting muons.

Secondary particles are absorbed more easily with the increase in the density of the atmosphere, some of them reach the surface of the Earth, and the most vigorous can penetrate significant depths of the Earth's crust.

When a primary cosmic ray hits directly with the nucleus of an atmospheric atom, depending on the energy of the primary particle, the size of the nucleus, etc., a variety of processes can occur. These can be divided into absorption and dispersion processes. In the scattering processes, the elasticity and the total kinetic energy are retained. On the other hand, in those of inelastic dispersion, a fraction of the energy of the incident ray is absorbed by the nucleus, leaving the latter excited. This energy is subsequently issued in the form of γ rays, α particles, etc.

Due to the large energy of the incident particle, most of the secondary particles that are produced are propagated in the same direction as the primary one.

There are three possible scenarios (Figure 1) by means of which the primary particle transfers its energy through the atmosphere to the sea level or down to a level below: the hadronic, the muonic, and the electromagnetic components.

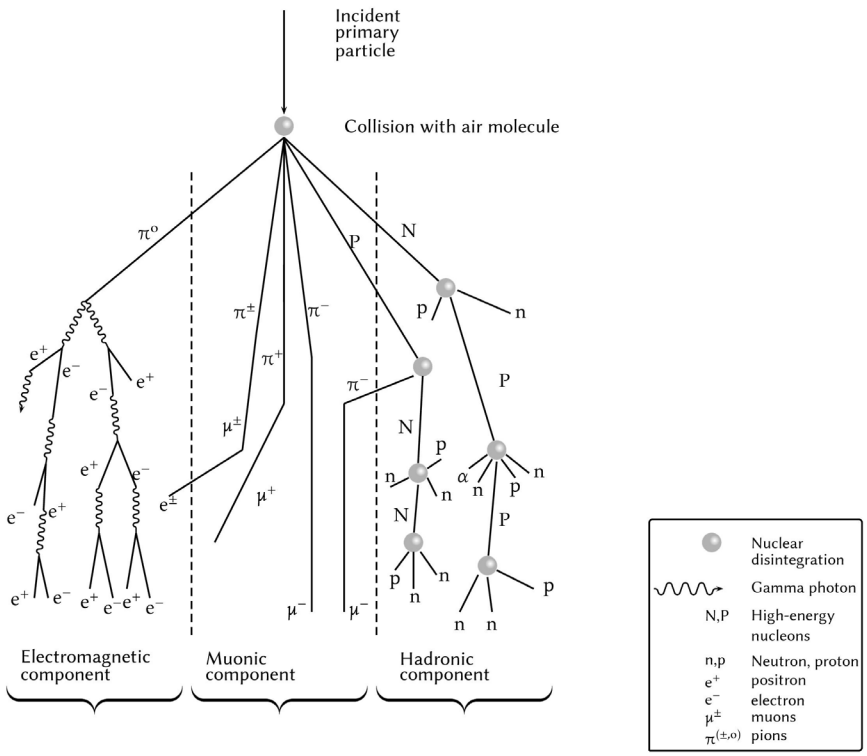

Figure 1. Basic scheme of an air shower. From left to right, the electromagnetic component (soft), muonic and hadronic cascades, are respectively denoted. Symbols 'p' and 'n' represent protons and neutrons.

Neutrons and protons that result of the disintegration of an atmospheric atom by a primary particle of low energy are those that originate the hadronic component. However, these nucleons, of lower energy as compared with the primary particle, have enough energy to act as if they were primary elements and interact with new atmospheric atoms, generating new showers. When reaching the lower atmospheric layers, the flow of this component decreases rapidly with the atmospheric depth.

2.2 Different atmospheric parameters and their influence due to meteorological effects.

Although the study of FDs was done using only the charged particle channels, in this section the calculations of the atmospheric correction coefficients for both charged and neutral channels of the SNT-SN are reported.

2.2.1 *Barometric effect*

Variations in the values of the counting rates in a given unit of time, due to the variation of atmospheric pressure is known as the barometric effect. Likewise, there may be variations in the counting rates of a cosmic ray monitor or telescope due to other meteorological factors such as: wind speed, temperature changes in the different seasons of the year, greater or lesser presence of humidity, greater or lesser presence of snow, among others (Dorman, 2004). The behavior of the pressure is inverse to the counting rates of the experiments: in the presence of a lower atmospheric pressure, a greater amount of particles (accounts/time) are recorded.

Based in the Dorman's criteria (2004, p. 352), a general expression for the correction of the counting rates as a function of the variability of the pressure at a certain height is

$$N(P)=N(P_0)\exp\left(\int_{P_0}^{P}\beta(P)dP\right) \quad (1)$$

where P_0 - normalization pressure, for the count value $N(P_0)$,

N(P) - value of the counting rates for the pressure P and β(P) - barometric coefficient, which is used to enter corrections by pressure on the values of the counting rates in each measurement channel. The barometric coefficient might be approximated as

$$\beta(P)=\beta(P_0)+\eta_1(P_0)(P-P_0)+\eta_2(P_0)(P-P_0) \quad (2)$$

where η1 and η2 - constant coefficients. If $(P-P_0)$are small ⇒ then

$$N(P)=N(P_0)\exp(\beta(P-P_0)) \quad (3)$$

If the variation in pressures is small, then

$$N(P)=N(P_0)(1+\beta(P-P_0)) \quad (4)$$

2.2.2 Wind speed effect

The dynamic pressure is determined by the Bernoulli's equation $P_{dyn}=\frac{1}{2}\rho v^2$, where

ρ – the air density and v - the wind speed.

The wind speed effect becomes important from v ≥ 10 ms^{-1} (Dorman, 2004). Barrantes, *et al*. (2018) established that in the case of the SN station registers this effect can not be verified, since at the SN top, for v≈20 ms^{-1}, the dynamic pressure values represent the 0.24% of the mean barometric pressure and besides that, the dynamic pressure values lie in the standard deviation range of the mean barometric pressure.

2.2.3 Relative Humidity effect

According to Dorman (2004), the total effect of the relative humidity (RH) may be determinated using the ratio

$$\frac{\beta_{rh}}{\beta_P} \quad (5)$$

where $\beta_{rh}=\beta_P+C_{rh}$, β_P and C_{rh} - barometric and RH coefficients, computed by the linear regression method as the slopes in the corresponding graph of normalised counting rates vs ΔP and ΔRH, respectively. In any case, the presence of water in the air may influence a significant increase in barometric effect, because the humid air mass is denser than dry air, what is observable in the behavior of the barometric pressure for periods of dry and humid seasons (Barrantes, *et al*., 2018).

2.2.4 Temperature effect

The length for crossing the same amount of matter (in g cm^{-2}) will increase with the increasing air temperature, but the number of nuclear interactions producing pions will decrease at a certain height (Dorman, 2004). This effect leads to the positive temperature effect for the muon component and to the negative temperature effect for the nucleonic component.

The atmospheric conditions for determining the temperature effect are usually characterized by the following parameters: the air temperature on the ground, the height and air temperature of the level where main muon generation is assumed to take place (usually levels of 100 or 200 mb), the average mass temperature of the atmosphere. Blackett (1938) used two parameters: the height H(h_M) and air temperature T(h_M) at the muon-generation level h_M (about 100-200 mb). Therefore the total regression equation for the temperature component has the form:

$$\left(\frac{\Delta N}{N}\right)_T = C_G \Delta T(h_G) + C_H \Delta H(h_M) + C_M \Delta T(h_M) \quad \text{(Dorman, 2004)} \quad (6)$$

where ΔT (h_G) is the ground temperature deviation at the h_G height and $h_M \geq 16$ km (De Mendonça, Raulin, Echer, Makhmutov, & Fernandez, 2013). In the present case h_G=4580 m asl. The detected CRs intensities that reach the surface of the Earth are influenced by the solar activity and by the structure of the geomagnetic field. In order to avoid this influence and to make a reliable calculation of the values of the atmospheric correction coefficients, two quiet intervals of solar activity: July 22 - August 20, 2004 (NOAA, K-Indexes, 2004) and September 23 - October 20, 2005 (NOAA, K-Indexes, 2005) were chosen. Since the data recorded by the SNT-SN and INAOE-SN stations were only at ground level, equation (6) was simplified as

$$\left(\frac{\Delta N}{N}\right)_T = C_G \Delta T(h_G) \equiv C_T \Delta T \quad (7)$$

2.3 Definition of coefficients for different atmospheric parameters

According to Dorman (2004) and based on the results shown in Table 2, the contribution of the atmospheric parameters in the normalized variations of the cosmic ray registers at Sierra Negra are determined by

$$\left(\frac{\delta N}{N}\right)_{total} = \left(\frac{\delta N}{N}\right)_P + \left(\frac{\delta N}{N}\right)_{WS} + \left(\frac{\delta N}{N}\right)_T + \left(\frac{\delta N}{N}\right)_{RH} \quad (8)$$

where

$\left(\frac{\delta N}{N}\right)_P = \beta_P \delta P$ barometric component"

$\left(\frac{\delta N}{N}\right)_T = C_T \delta T$ temperature component"

$\left(\frac{\delta N}{N}\right)_{RH} = C_{RH} \delta RH$ component due to RH"

$\left(\frac{\delta N}{N}\right)_{WS} = \beta_{WS} \delta WS$ component due to WS

and β_P, C_T, C_{RH}, β_{WS} are the atmospheric correction coefficients.

3 Instrumentation

3.1 Solar Neutron Telescope at Sierra Negra

Sierra Negra (SN) is a 4580 m asl inactive volcanic cone formed 460 000 yr ago, located at 18.98º N, 97.46º W, inside the Parque Nacional Pico de Orizaba, Mexico, at about 100 km east from Puebla City. The weather of the site is influenced by the dry climate of the high-altitude central Mexican plateau and humid conditions coming from the Gulf of Mexico (Carrasco, et. al., 2009). The Solar Neutron Telescope at the top of Sierra Negra (SNT-SN) is operating since 2004. A detailed description of the SNT may be found in González-Méndez (2010); the detector has the ability to measure the energy deposited by the incident particles, and their direction of arrival with a precision of 15 degrees. To detect neutrons associated with solar flares at the ground level, it is preferable to locate detectors very close to the Equator, ensuring that the exposure time to the Sun does not change much with yearly seasons and that the charged particle cuotoff required for incident ions is very high, eliminating as much as possible the influence of protons emmited during the same solar event. It is also preferable, to be located as high as possible a.s.l. to reduce the amount of matter which can interact with solar neutrons, increasing the probability of neutrons to be detected. Because they have zero charge, solar neutrons can travel from the Sun to the top of the atmosphere without being affected by any electromagnetic field, with a probability of survival for the neutron,

$$P(E) = \exp\left(-\frac{t}{\gamma\tau}\right) \quad (9)$$

where t is the flight time of a neutron between the Sun and Earth, γ is its corresponding Lorentz factor and τ=(880.2±1.0) s is the neutron mean lifetime (Patrignani & others, 2016). SNTs were installed at different longitudes making a world network that has continuous observations of the Sun. The SNT-SN consists of plastic scintillators (PS) surrounded by proportional counters (PCs). It distinguishes between charged and neutral particles by an electronic anticoincidence system between the signals triggered by PS and PCs.

3.2 Structure and general operation of the Solar Neutron Telescope at Sierra Negra, Puebla.

A scheme of the SNT-SN is presented in Figure 2. The detector was built and tested in March 2003 in SN; long operation periods since November 2004 have been possible. The area of each PS is 1 m^2, with four of them the total detection area is 4 m^2, the thickness of the plastics is 30 cm.

The SNT-SN has four energy (E) deposition channels, which correspond to E⩾30MeV, E⩾60 MeV, E⩾90 MeV and E⩾120 MeV. Above the uppermost PCs gondola (Figure 2) a 0.5 cm thick lead plate is placed, where 67% of the incident photons are converted into electron-positron pairs (Valdés-Galicia, *et al*., 2004). To reduce background radiation from the sides, PCs were protected of the background photons by iron plates of 0.5 cm thickness (González-Méndez, 2010), these four vertical planes iron sheets act as shielding. Most of the incidente gamma rays are contained by the lead, where they produce electron positron pairs; the charged particles (mostly protons) trigger the PCs and the PS, while the neutral particles only trigger the PS. All these events are registered by the system, which records the energy deposited by every particle in PMTs located just above the PS. Thus, the SNT discriminates between charged particles and neutrons based on the electronic anticoincidences between PCs and PS.

The energy deposited by the incident particles is measured with pulse height discriminators, connected to the PMTs which are installed above every PS inside light tight boxes. The height of the pulse is discriminated and recorded in the four different energy deposition channels stated above. The logical scheme of detection of the SNT-SN is shown in Figure 3.

4 Data coverage

In order to determine the correction coefficients due to atmospheric effects data on two periods were used: September 23 - October 20, 2004 and July 23 - August 22, 2005. These periods were selected since they are geomagnetically quiet (NOAA, K-Indexes, 2004, NOAA; K-Indexes, 2005), with a relative low solar activity, near the end of the 23th Solar Cycle (http://www.swpc.noaa.gov/products/solar-cycle-progression, solar activity images A REFERENIAAS). A part of these data consists of atmospheric pressure, temperature, relative humidity (RH) and wind speed, recorded by the INAOE-SN station called Campbell and which has been operational since 2000. The Campbell station consists of temperature and humidity sensors enclosed on a radiation shield, a barometer, an anenometer, a controle console and a data logger. The Campbell station data have a 1 min time resolution. The location of the Campbell station relative to the SNT-SN station

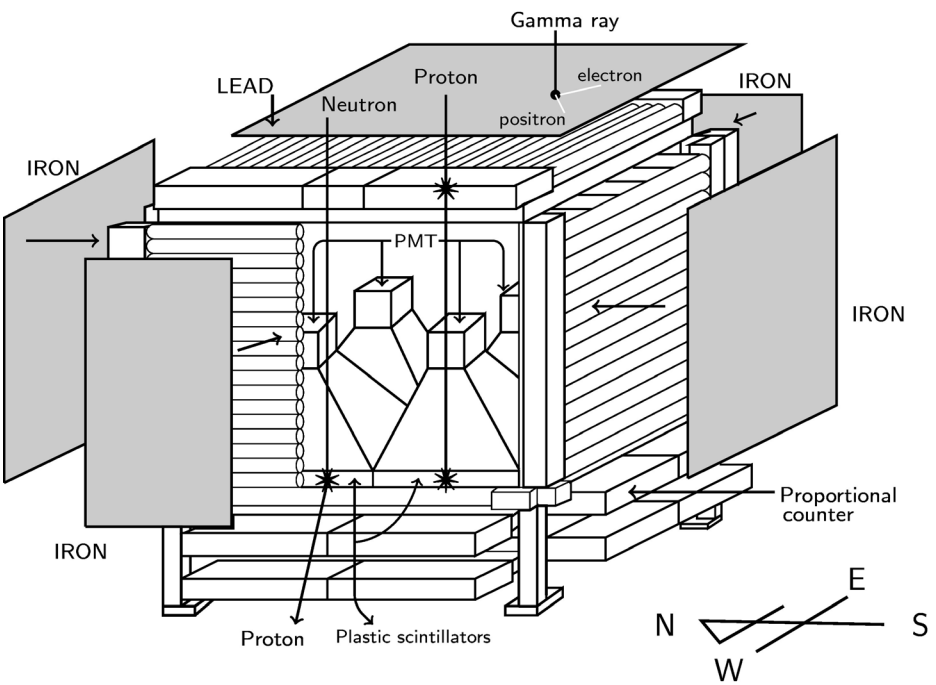

Figure 2. Scheme of the SNT-SN. Anticoincidences between protons and neutrons are shown using the PS and PCs. The dimensions of the SNT-SN are 2m x 2m x 2 m.

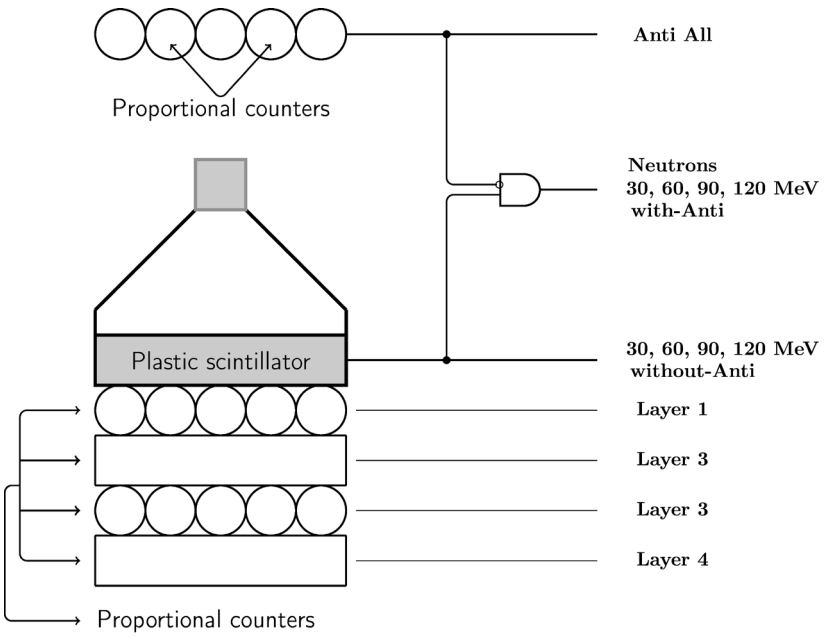

Figure 3. SNT logical detection system. Signals are measured by PS, PCs. Coincidence signals for charged particles channels and anticoincidence signals for the neutral particle channels, which correspond to neutrons.

is (201,104) m in the NE direction (Barrantes, *et al*., 2018). The data of atmospheric pressure at the SNT-SN station were also used. The SNT-SN station data on 2004-2005 period have a 1 min resolution. Since a FD is a phenomenon whose evolution is in the order of hours, all atmospheric data were averaged at intervals of 30 minutes, in order to analyze possible variations of the values of the atmospheric parameters in short time intervals, given the time scale of the phenomenon under analysis. To determine the value of the correction coefficients we used the linear regression method of Dorman (2004). There are various interpretations of what is a FD. In general, it is established as a global secondary cosmic radiation event at Earth level, registered by the worldwide network of NMs. Here, a FD is defined as the phenomenon which presents the next two characteristics (Musalém, 2015):

1. Its fall, in the percentage of the intensity of the secondary cosmic radiation, is at least 1.5%; this allows us to discriminate from the diurnal variation (amplitude approx. 0.7%). The interval between onset and minimum point is reached in less than 24 hours.

2. The recovery time is 7 days, on average. It should be noted that the record of a FD will depend, among other factors, on the latitude at which the monitoring station is located: at greater geomagnetic latitude, lower geomagnetic rigidity threshold.

The Neutron Monitor station at UNAM (NMCDMX) (http://cosmicrays.unam.mx), is part of the worldwide network of cosmic ray detectors called Neutron monitor database (NMDB) (http://nmdb.eu/nest). It has been operational since 1989. A list of FDs was produced for the period 2007-2013, based on the records of this station and Moscow and Oulu NMs (Musalém, 2015).

Six FD were selected, clearly observed in the S1, S2 and S3 charged particle channels, based on the available SNT-SN data set (see Table 1). These events were selected considering that they were recorded in both, the SNT-SN and the NMCDMX. The quality of the data recorded by the SNT-SN for each FD within the list was verified. Additionally, in order to be sure that the selected events were worldwide, FDs had to be registered by all three monitors of the Musalém (2015) list, as it is clearly evidenced in our case.

In the cases of FDs registered by SNT-SN, the records of charged particles were used, since the GCRs are essentially charged particles. Due to some inconsistences in the data registered in the S4 channel for some FDs, data from this channel were not used. SNT-SN station data were averaged in intervals of 60 min., with the purpose of comparing these results with those obtained by the NMCDMX.

Table 1. FDs selected for analysis. Reliability of the registers in SNT-SN is required. The threshold of the NMs are in GV: Oulu 0.81, Moscow 2.41 and Mexico City 8.42.

FD	Oulu (%)	Moscow (%)	Mexico City (%)
17/06/2011	2.8	2.5	2.3
05/08/2011	5.0	4.5	2.5
08/03/2012	11	9.0	7.0
05/04/2012	3.5	3.0	3.5
16/06/2012	5.0	4.0	4.0
14/04/2013	5.0	4.5	4.0

Table 8 presents the percentages of the maximum decrease for each selected FD recorded by the SNT-SN and the NMCDMX, whose similarities/differences are discussed in section 5.

5 Calculation of correction coefficients

5.1 Correction coefficients by atmospheric parameters.

Based on the mean values of the atmospheric parameters for each of the select periods that are shown in the Table 2, it is evident that the contribution of the dynamic pressure to the total pressure at the SN summit is negligible, since for both periods the maximum value of the dynamic pressure is within the uncertainty range of the values of the barometric pressure.

In Figure A- 1 - Figure A- 6 (appendix) the scatter plots of normalized counting rates as a function of barometric pressure, temperature and relative humidity variations are shown. β_P, C_T and C_{RH}, $\Delta\beta_P$, ΔC_T and ΔC_{RH} represent the value of the respective coefficient and its standard deviation, calculated by linear regression. In addition, the value of the Pearson correlation coefficient and the standard deviations of the data of each axis are shown in the plot upper insert.

Table 3 summarizes the values of the coefficients per channel for the three atmospheric parameters considered during the period September 23-October 20, 2004.

Table 4 shows the values of the coefficients per channel for the period July 22 - August 20, 2005.

The values in Table 3 and Table 4 marked with a * are unreliable because their respective uncertainties are of the same order as the average value, i.e. the mean may be zero.

Table 2. Mean values of the atmospheric parameters for each of selected periods: Sep 23-Oct 20, 2004 and Jul 22- Aug 20, 2005. Here, $P_{dyn}=\frac{1}{2}\rho_{air}\, v_w^2$, $\rho_{air}=\rho_0(1-\frac{\theta z}{T0})^{\alpha}$=0.72 kg m^{-3}; where ρ_0=1.24 kg m^{-3}, α=5.256, θ=6.5 K km^{-1}, T_0=305.15 K, according to ISA

Period	P (mbar)	P_{dyn} (mbar)	T (ºC)	RH (%)
Sep 23 - Oct 20	589.98 ± 1.06	0.18 ± 0.32	3.38 ± 3.19	82.78 ± 10.42
Jul 23 - Aug 22	591.35 ± 0.90	0.25 ± 0.22	4.34 ± 4.61	67.13 ± 17.66

Table 3. Values of the correction coefficients due to atmospheric parameters for the records of the INAOE-SN and SNT-SN stations, shown for neutral and charged particles channels. Period Sep 23 - Oct 20, 2004.

Channel	β_P %/mbar	C_T %/(ºC)	C_{RH} /%
$S1_{neutral}$	-0.173 ± 0.054	0.455 ± 0.011	-0.008 ± 0.006 **
$S2_{neutral}$	-0.287 ± 0.038	0.245 ± 0.010	0.002 ± 0.004 *
$S3_{neutral}$	-0.490 ± 0.031	-0.008 ± 0.012 *	0.23 ± 0.003 **
$S4_{neutral}$	-0.406 ± 0.046	0.244 ±0.014	0.13 ± 0.005 **
$S1_{charged}$	-0.354 ± 0.013	-0.029 ± 0.006	0.10 ± 0.002 **
$S2_{charged}$	-0.399 ± 0.020	-0.114 ± 0.007	0.18 ± 0.002 **
$S3_{charged}$	-0.515 ± 0.023	-0.138 ± 0.08	0.26 ± 0.002 **
$S4_{charged}$	-0.600 ± 0.026	-0.148 ± 0.010	0.28 ± 0.003 **

Table 4. Values of the correction coefficients due to atmospheric parameters for the records of the INAOE-SN and SNT-SN stations, shown for neutral and charged particles channels. Period Jul 22 - Aug 20, 2005.

Channel	β_P %/mbar	C_T %/(ºC)	C_{RH} /%
$S1_{neutral}$	-0.152 ± 0.095	0.587 ± 0.011	-0.006 ± 0.004 **
$S2_{neutral}$	-0.337 ± 0.064	0.368 ± 0.009	0.002 ± 0.003 *
$S3_{neutral}$	-0.536 ± 0.033	0.046 ± 0.008	0.016 ± 0.002 **
$S4_{neutral}$	-0.428 ± 0.074	0.392 ± 0.011	0.009 ± 0.003 *+
$S1_{charged}$	-0.363 ± 0.013	-0.023 ± 0.004	0.008 ± 0.001 **
$S2_{charged}$	-0.424 ± 0.022	-0.098 ± 0.005	0.013 ± 0.001 **
$S3_{charged}$	-0.544 ± 0.027	-0.122 ± 0.006	0.018 ± 0.001 **
$S4_{charged}$	-0.622 ± 0.029	-0.124 ± 0.006	0.020 ± 0.001 **

Those indicated with **, correspond to the relative humidity correlations with cosmic ray intensity, these values were not considered since, due to the high calorific capacity of the water, the relative humidity acts as a temperature catalyst. This indicates that the influence of the relative humidity on the variation of the particle count recorded by the SNT-SN is included in the temperature correction. Besides, the RH coefficients are generally at least an order of magnitude smaller than the pressure or temperature coefficients. Therefore only two coefficients (pressure and temperature) are neccesary for the atmospheric effects correction to the SNT intensity rates.

It should be noted that the temperature coefficients for the neutral particle channels showed in Table 3 and Table 4 are positive. This is due to the predominance of the negative effect of temperature on the total neutron component over all the atmosphere. In the high atmosphere, neutral pions ($\pi^0_{\text{mean-life}}$=(8.52±0.18)x10^{-17}s) decay in electromagnetic component of air shower, a fraction of charged pions ($\pi^{\pm}_{\text{mean-life}}$ = (2.6033±0.0005)x10^{-8}s (Patrignani and others, 2016)) decay in muons, raising the sea level and deeper (Figure 1). On the other hand, a relative number of charged pions collide with nuclei of air particles, generating neutrons and protons: with increasing air temperature, the length for crossing the same depth of matter "(in g cm^{-2}) will increase but the number of nuclear interacted pions will decrease (Dorman, 2004).

5.2 Determination of a global correction coefficient

The general correction coefficient is

$$\beta_{\text{total}} = \beta_P + \beta_T \qquad (10)$$

To use equation (10) it is necessary to express the temperature coefficient C_T(%/ºC) as β_T(%/mbar).

Table 5 summarizes the values of the correction coefficients for each channel under study, for the analyzed quiet periods.

Table 5. Correction coefficients by atmospheric parameters for the channels S1, S2 and S3 for charged particles and the respective global average, for the periods of September 23-October 20, 2004 and July 22-August 20, 2005. As shown in equation (10), $\beta_{total} = \beta_P + \beta_T$.

	2004			2005		
Channel	S1	S2	S3	S1	S2	S3
C_T %/ºC	0.029	0.114	0.138	0.023	0.098	0.122
β_T %/mbar	0.018	0.072	0.087	0.027	0.117	0.145
β_P %/mbar	0.354	0.399	0.515	0.363	0.424	0.544
β_{total} %/mbar	0.372	0.471	0.602	0.390	0.541	0.689
Channel	S1		S2		S3	
$\bar{\beta}_{total}$ %/mbar	0.381 ± 0.030		0.506 ± 0.064		0.646 ± 0.078	

As can be observed in Table 5, for channels S1, S2 and S3 the ratios $\frac{\bar{\beta}_T}{\bar{\beta}_T}$ are 0.07, 0.23 and 0.22 respectively. In the case of the S1 channel, the $\bar{\beta}_T$ value (0.023) lies within the range of the $\bar{\beta}_{total}$ uncertainty. For the channel S2, its $\bar{\beta}_T$ value (0.095) is of the same order that its $\bar{\beta}_{total}$ uncertainty. In the case of the S3 channel, its $\bar{\beta}_T$ value (0.116) is just a 49% higher than the standard deviation for its corresponding $\bar{\beta}_{total}$. These calculations show that the prevailing atmospheric parameter to perform the correction of the SNT-SN counting rates is the barometric pressure. The coefficients for neutral particles are not considered, since FDs events are phenomena related to charged particles.

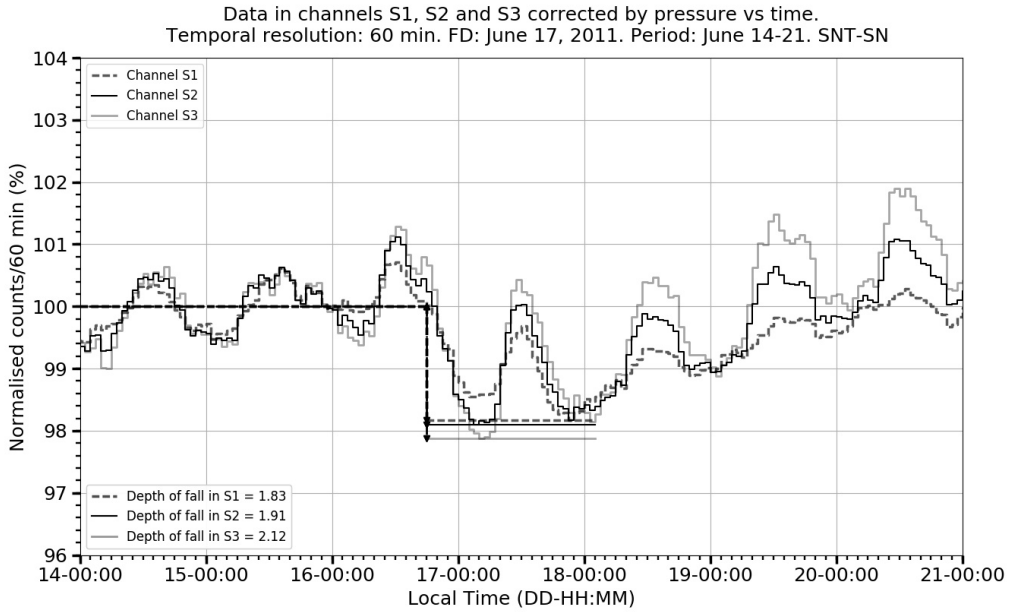

Figure 4. FD on June 17, 2011. The graph shows the normalized counting rates time evolution of the three charged particle channels in the counting rates corrected by pressure.

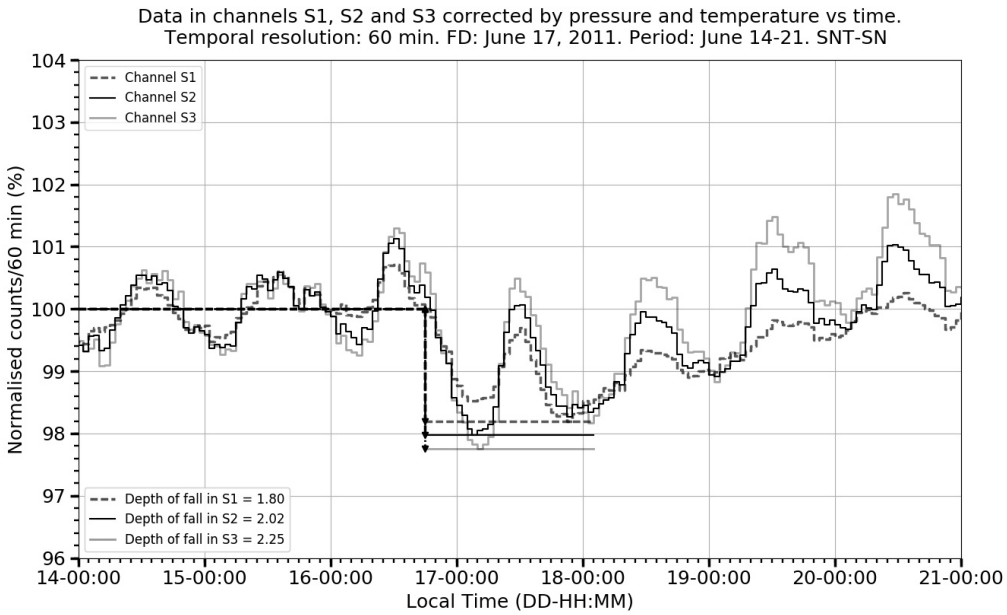

Figure 5. FD on June 17, 2011. The graph shows the normalized counting rates time evolution of the three charged particle channels, corrected by pressure and temperature.

6. Selected FDs time-intensity results

The plots presented below show the selected FDs, for which data were corrected by pressure and by pressure plus temperature. The vertical axis presents the values normalized to the average values of the counting rates of each channel, expressed as percentage of the total. The counting rates are normalized to the mean value of the data set corresponding to three quiet days before the onset of the FD. On the horizontal axis time is represented in DD-HH:MM format. The values in the inset of each graph are shown as percentage values. In each graph, information in the inset shows the percentage of the counting rate decreases in each of the plotted channels. For the purpose of comparison with the NMCDMX records, the temporal resolution of the data in every one of these plots is about 60 minutes.

6.1 June 17, 2011 event

Figure 4 and 5 show that the level of daily fluctuations in the counting rates is high and that the maximum amplitude of the diurnal variation (1.6%) represents a high proportion of the percentage of the FD fall (71% in the S3 channel). On the other hand, let us consider the depth of decrease (ff_{PP}), based on data corrected by pressure, and the depth of fall ff_{PT}, based on data corrected by pressure plus temperature. The parameter $ff = \left(\frac{ff_{PT} - ff_{PP}}{ff_{PP}}\right)$ - is the normalized difference amongst these two. In this event, the relative differences between the fall percentage values shown in Figure 4 and 5, for the channel S1 is -0.02 (-2% of the decrease value), for the channel S2 is 0.06 (6% of the decrease value) and for S3 is 0.06 (6% of the decrease value). For all channels, the relative differences are two orders of magnitude smaller than the percentage of FD.

6.2 August 05, 2011 event

Figure 6 and Figure 7 show that the level of daily fluctuations in the counting rates is high and that the maximum amplitude of the diurnal variation (3%) represents a very high proportion of the percentage of the FD fall (256% in the S3 channel). In this event, the relative differences between the fall percentage values shown in Figure 6 and Figure 7: for the channel S1 is 0.00 (0% of the decrease value), for S2 is 0.01 (1% of the decrease value) and for S3 is 0.01 (1% of the decrease value). In the S2 and S3 channel cases, the relative differences are two orders of magnitude smaller than the percentage of FD.

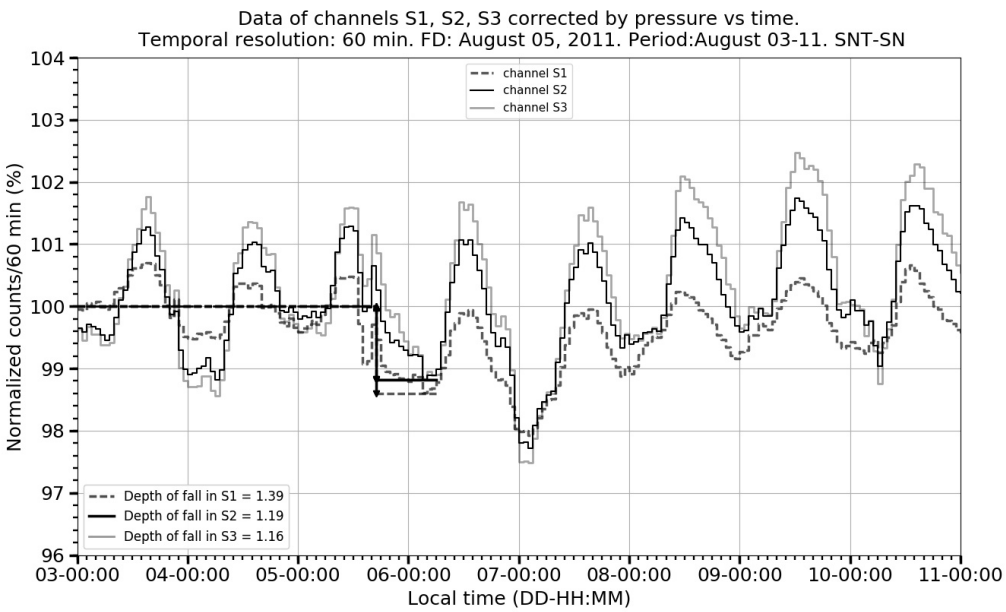

Figure 6. FD on August 05, 2011. The graph shows the normalized counting rates time evolution of the three charged particle channels in the counting rates corrected by pressure.

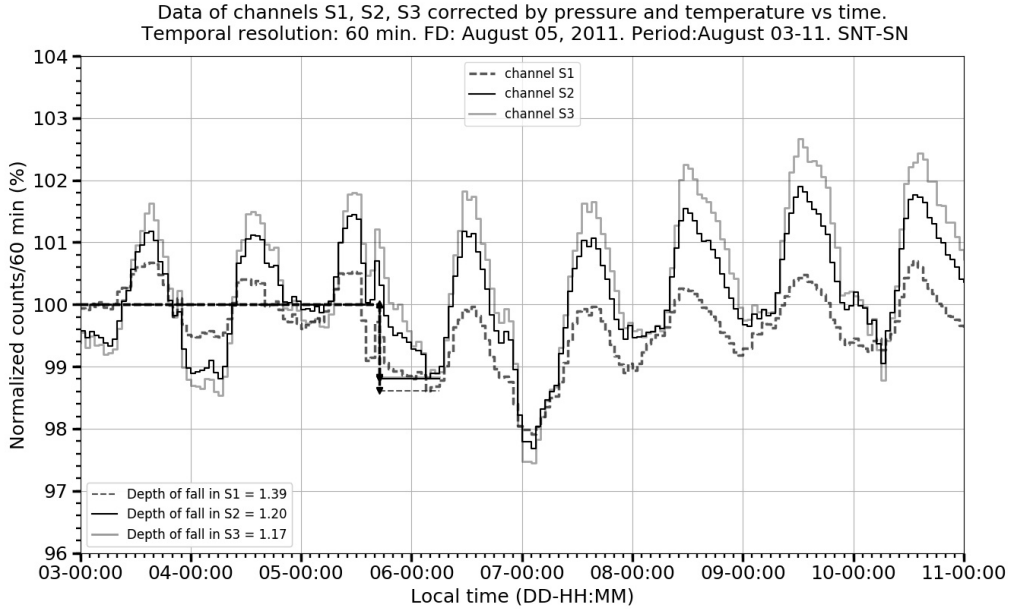

Figure 7. FD on August 05, 2011. The graph shows the normalized counting rates time evolution of the three charged particle channels, corrected by pressure and temperature.

6.3 March 08, 2012 event

Derived from the normalized counting rates in Figure 8 and Figure 9, we estimate for the channel S3, $ff_3 = \left(\frac{ff_{PT} - ff_{PP}}{ff_{PP}}\right)_3 = 0.03$, being this the bigger one of the three estimates. Therefore, for this event, practically there is no difference between values, given by the pressure and the pressure plus temperature corrections. The March 08, 2012 event presents fluctuations in the amplitude of the diurnal variations (ADV) in all channel counting rate registers, about 2%. The $\frac{ADV}{ff_{PT}}$ ratio for the S3 channel reaches 36%, the lowest ratio value for any of the studied events.

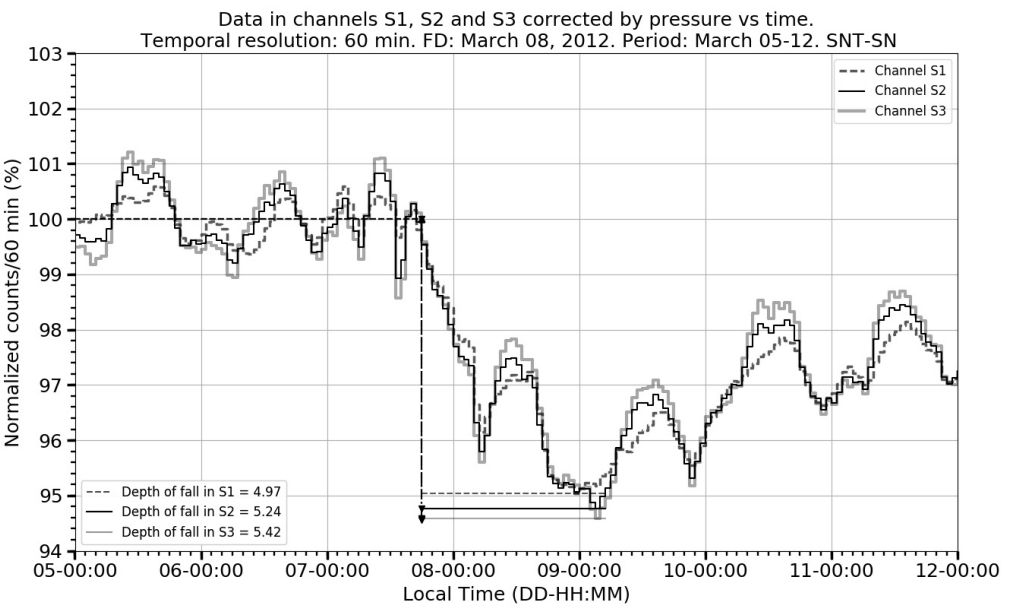

Figure 8. FD on March 08, 2012. The graph shows the normalized counting rates time evolution of the three charged particle channels in the records, corrected by pressure.

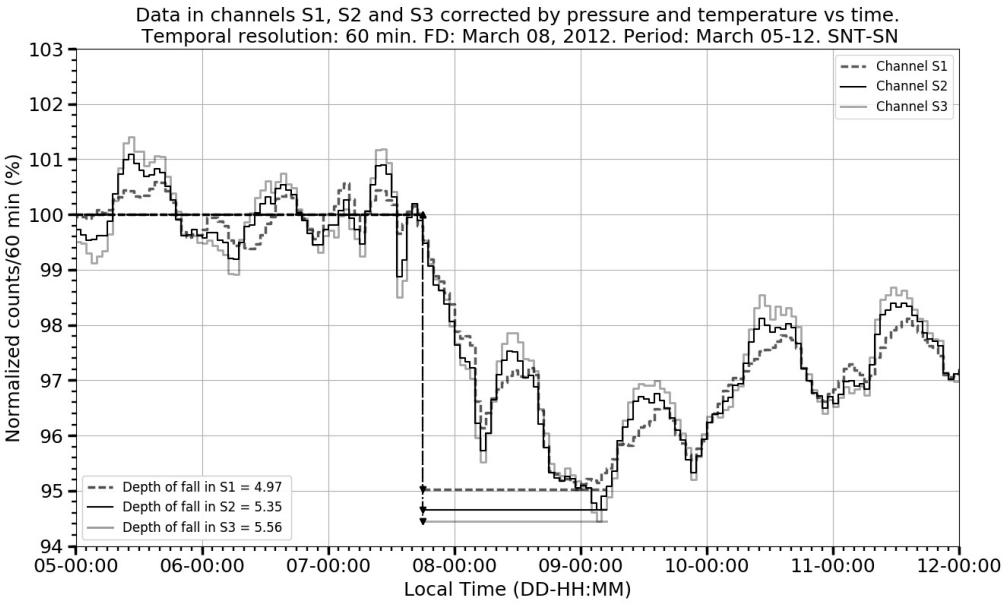

Figure 9. FD on March 08, 2012. The graph shows the normalized counting rates time evolution of the three charged particle channels in the records, corrected by pressure and temperature.

6.4 April 05, 2012 event

Figure 10 and 11 show that the maximum amplitude of the diurnal variation is about 2% and it represents a very high proportion of the percentage of the FD fall (82% in the S1 channel, for the counting rates corrected by pressure). In this event, the relative differences between the fall percentage values shown in Figure 10 and 11 for channel S1 is -0.02 (-2% of the decrease value), for S2 is -0.05 (-5% of the decrease value) and for S3 is -0.07 (-7% of the decrease value). For all channels, the relative differences are two orders of magnitude smaller than the percentage of FD.

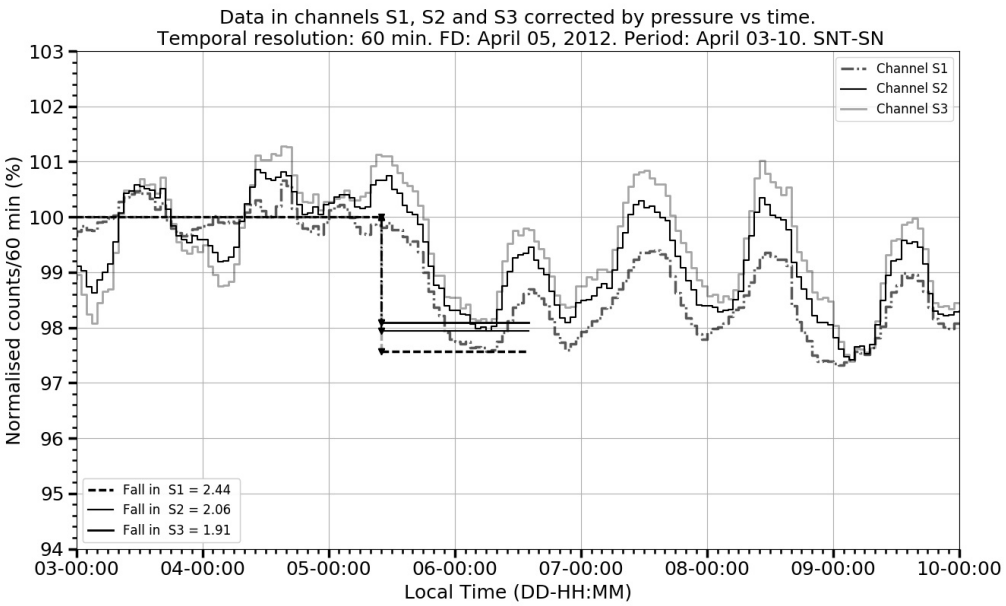

Figure 10. FD on April 05, 2012. The graph shows the normalized counting rates time evolution of the three charged particle channels in the records, corrected by pressure.

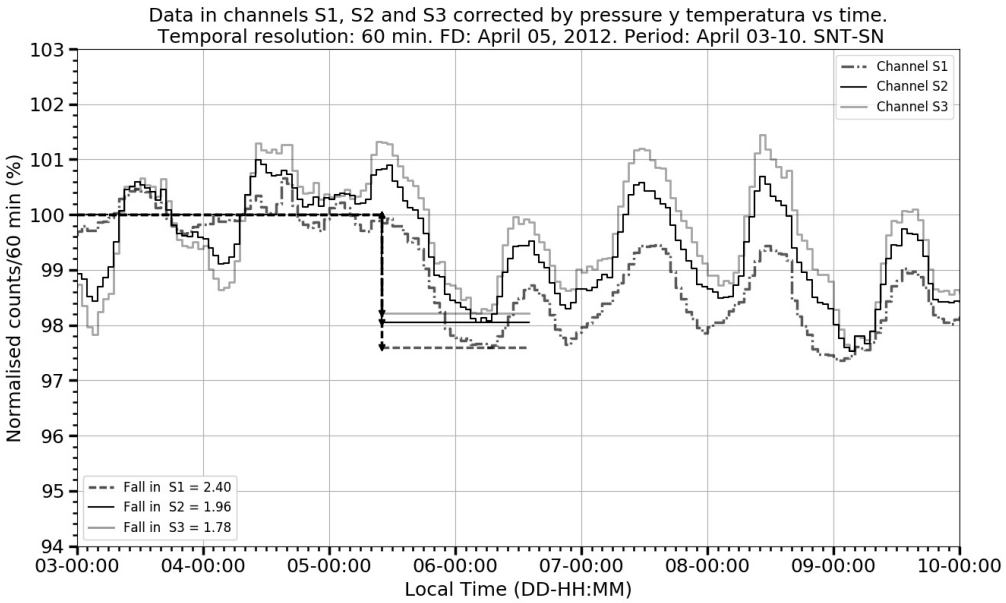

Figure 11. FD on April 05, 2012. The graph shows the normalized counting rates time evolution of the three charged particle channels in the records, corrected by pressure and temperature

6.5 June 16, 2012 event

Derived from the normalized counting rates in Figure 12 and 13 estimations were performed for the channels: S1, $ff_1 \left(\frac{ff_{PT} - ff_{PP}}{ff_{PP}}\right)_1$=-0.01, S2, $ff_2=\left(\frac{ff_{PT} - ff_{PP}}{ff_{PP}}\right)_2$=-0.02, S3, $ff_3\left(\frac{ff_{PT} - ff_{PP}}{ff_{PP}}\right)_3$=-0.02. Therefore, for this event, practically there is no difference between values, given by the pressure and the pressure plus temperature corrections.

The June 12, 2012 FD presents high fluctuations in the ADV in all channel counting rate registers (2 - 4.5%) in the hours just before the start of the event. Its mean value (3%) represents a very high proportion (113%) of the deepest decrease value (2.66%).

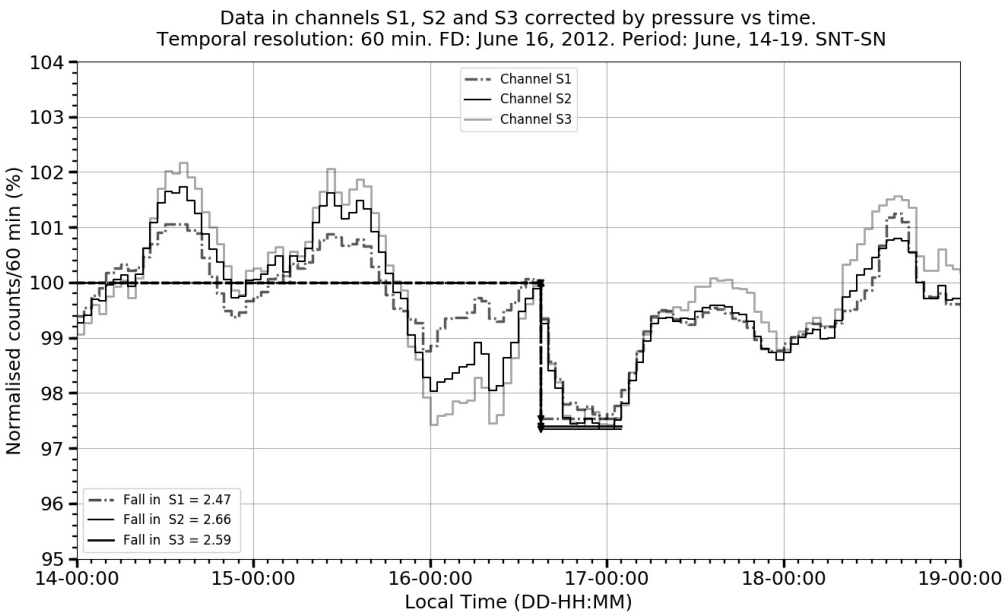

Figure 12. FD on June 16, 2012. The graph shows the normalized counting rates time evolution of the three charged particle channels in the records, corrected by pressure.

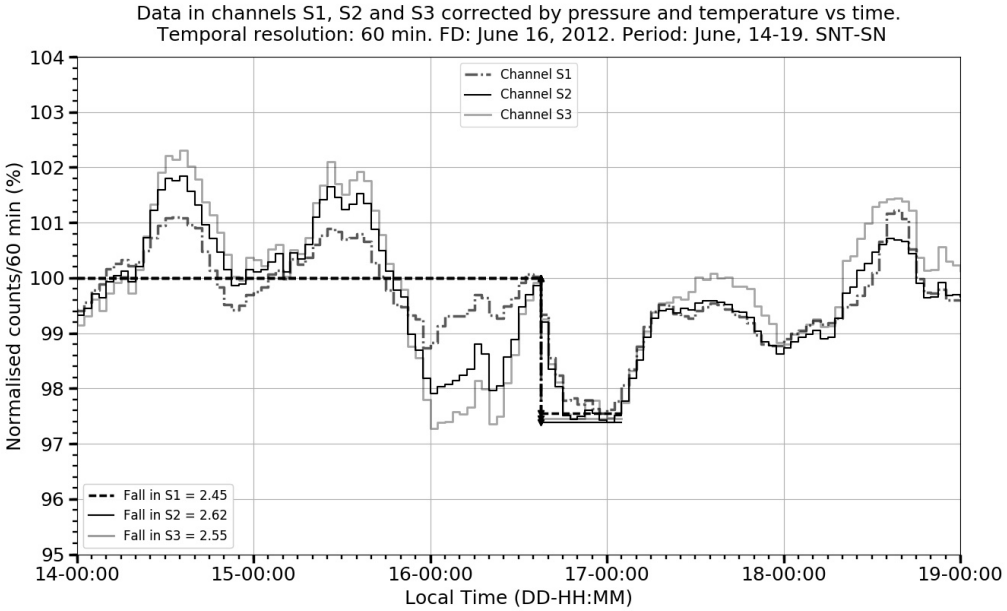

Figure 13. FD on June 16, 2012. The graph shows the normalized counting rates time evolution of the three charged particle channels in the records, corrected by pressure and temperature.

6.6 April 14, 2013 event

Once data corrections by pressure and by pressure plus temperature were made for this event, the variations $ff_1 \left(\frac{ff_{PT} - ff_{PP}}{ff_{PP}}\right)_1$=-0.02, $ff_2 \left(\frac{ff_{PT} - ff_{PP}}{ff_{PP}}\right)_2$=0.05, and $ff_3 \left(\frac{ff_{PT} - ff_{PP}}{ff_{PP}}\right)_3$=0.07, *were calculated*. The highest values of the normalized correction coefficients difference that have been found in this work, between pressure and pressure plus temperature corrections, are presented. The differences presented in the values are small; therefore only the pressure correction is found necessary. Table 6 summarizes those records for data corrected by pressure and by pressure plus temperature.

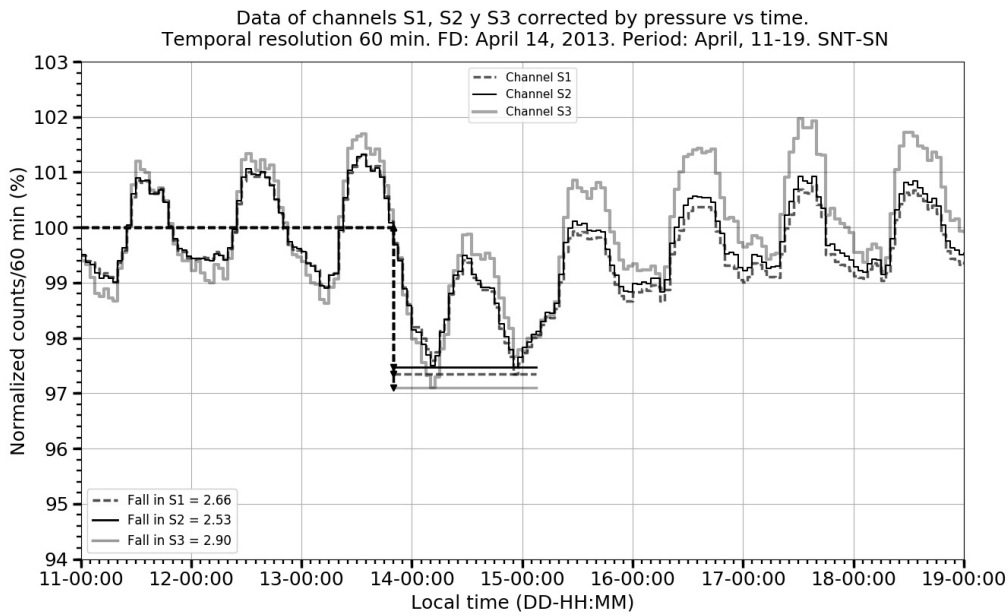

Figure 14. FD on April 14, 2013. The graph shows the normalized counting rates time evolution of the three charged particle channels in the records, corrected by pressure.

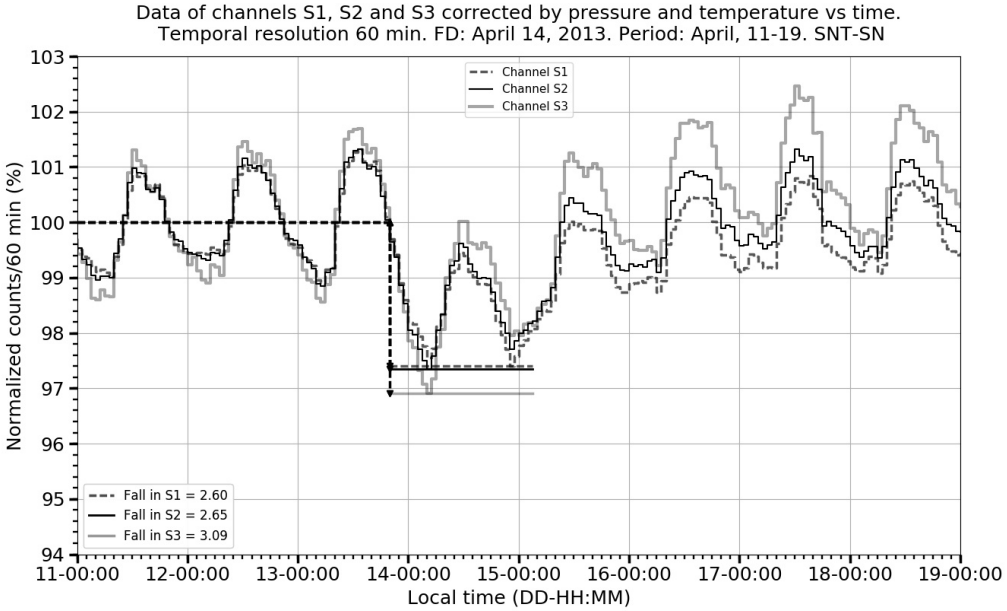

Figure 15. FD on April 14, 2013. The graph shows the normalized counting rates time evolution of the three charged particle channels in the records, corrected by pressure and temperature.

Table 6. Relative variations in the fall percentage values for the FDs analyzed, for the data corrected by pressure and by temperature and pressure, where $ff_3 = \left(\frac{ff_{PT} - ff_{PP}}{ff_{PP}}\right)$, estimated for the channel $S3_{charged}$.

FD	ff_{PP} (%)	ff_{PT} (%)	ff_3
17/06/2001	2.12	2.25	0.06
05/08/2011	1.16	1.17	0.01
08/03/2012	5.42	5.56	0.03
05/04/2012	1.91	1.78	-0.07
16/06/2012	2.59	2.55	-0.02
14/04/2013	2.90	3.09	0.07

As stated previously, one of the main goals of the present work was to determine the SNT-SN capabilities as an instrument for the analysis of FDs.

Table 7 shows the percentage decrease for each event and for each charged particle channel, together with the estimated ADV amplitude, which is then used to compare the FD depth in the counting rates with that of the diurnal variation.

The results shown in Table 7 tells that almost all of the amplitudes of the diurnal variation exceed the 50% of the maximum decrease of the different FDs studied. This fact leaves only one event for which the amplitude of the diurnal variation does not exceed the 50% of the maximum decrease. This implies that the SNT-SN is not a reliable instrument to analyze FD events for which the percentage decrease in the counting rate is less than 5%.

The decay rates recorded in the S1, S2 and S3 channels of the SNT-SN were computed for the selected events. They are summarized in Table 8.

Table 7. Values of the fall percentages for the FDs analyzed and the corresponding proportion of the amplitude of the diurnal variation (ADV). The values in parentheses represent the proportion $\frac{ADV}{ff_{PT}}$ for the corresponding channel.

FD	ADV(%)	S1	S2	S3
17/06/2011	1.6	1.80 (0.88)	2.02 (0.80)	2.25 (0.71)
05/08/2011	2.0	1.39 (1.42)	1.20 (1.67)	1.17 (1.60)
08/03/2012	1.6	4.97 (0.32)	5.35 (0.30)	5.56 (0.29)
05/04/2012	1.6	2.40 (0.67)	1.96 (0.81)	1.78 (0.90)
16/06/2012	3.0	2.45 (1.22)	2.62 (1.14)	2.55 (1.17)
14/04/2013	2.0	2.60 (0.77)	2.65 (0.75)	3.09 (0.65)

Table 8. Comparison of FD percentage recorded in the SNT-SN channels S1, S2 and S3, and the fall percentage registered by the NMCDMX.

FD	S1	S2	S3	Average	NMCDMX
June 17, 2011	1.80 ± 0.05	2.02 ± 0.05	2.25 ± 0.06	2.02 ± 0.34	2.3
August 05, 2011	1.39 ± 0.05	1.20 ± 0.06	1.17 ± 0.08	1.25 ± 0.29	2.0
March 08, 2012	4.97 ± 0.09	5.35 ± 0.09	5.56 ± 0.11	5.29 ± 0.53	7.0
April 05, 2012	2.40 ± 0.08	1.96 ± 0.08	1.78 ± 0.08	2.04 ± 0.41	3.5
June 16, 2012	2.45 ± 0.08	2.62 ± 0.07	2.55 ± 0.08	2.54 ± 0.31	4.0
April 14, 2013	2.60 ± 0.08	2.65 ± 0.09	3.09 ± 0.10	2.78 ± 0.50	4.5

The uncertainty numbers expressed in the column 'Average' include the standard deviation of the FD values recorded in channels S1, S2 and S3 of charged registers, and the margin of uncertainty from the values for every channel, for each event. From the calculations shown in Table 8 it can be seen that all events chosen for this study the estimated depths of the FDs by SNT-SN are under those registered by the NMCDMX (Musalém, 2015). As shown in Table 7, the March 08, 2012 is the only event for which the $\frac{ff^{ADV}}{ff_{PT}}$ proportion is under the 50% in all the three charged particle channels of the SNT-SN. This difference could be due to the lower energies present in the cosmic ray showers that are able to arrive to SN, but not to CDMX as there is a 200 g cm^{-2} difference in the heights of both locations and therefore the lowest energy component of the showers must be absorbed. According to Shibata (1994), for particles with energies of 150 MeV, the attenuation for CDMX as compared to that of SN has at least an order of magnitude difference.

Figure 16 shows the response functions for both detectors on March 2012, using Clem & Dorman (2000) formalism.

From Figure 16 it may be appreciated that the Rigidity Response for both monitors are very similar. Mean responses were computed, for SNT-SN is about 23.7 GV and for NMCDMX is about 24.5 GV.

Therefore, the difference can be considered in the minimum values registered by both stations on all selected events, and might additionally be due to the slight difference in their mean differential response values.

7 Summary and conclusions

In this work an analysis of six selected FDs in the period 2011-2013, recorded by the SNT-SN was presented. The aim was to determine if the SNT-SN is a reliable instrument for research on the FD phenomena. In order to know which of the relevant atmospheric parameters (pressure, temperature, relative humidity and wind speed) might have an influence in the registered counting rates, a detailed correlation study was done with each one of these parameters. It was determined that dynamical pressure is not

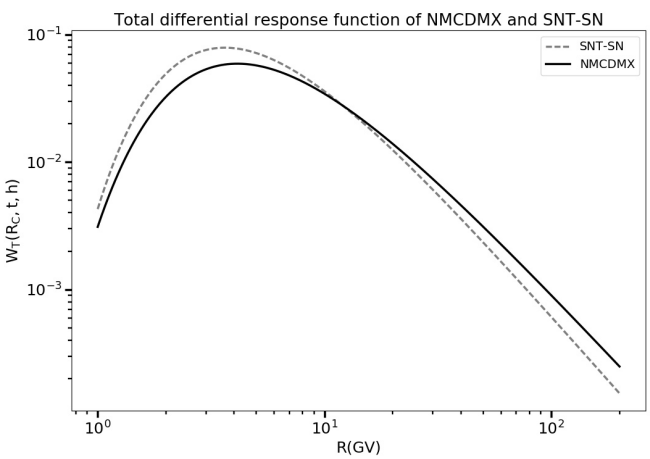

Figure 16. Total differential response functions for the NMCDMX and the SNT-SN, on March 2012. Plots were calculated according to Clem & Dorman (2000) expressions.

significant in the total pressure value, therefore the barometric pressure is the only one of the two to be considered for the subsequent analysis. Plots of the data recorded in the S1, S2, S3 channels for neutral and charged registers on the SNT-SN vs pressure, temperature and RH for the calculation of the correction coefficients, using data from quiet periods, avoiding in this way the possible influence of the solar activity phenomena were made. Relative Humidity had not enough influence in the data variations and then only the barometric pressure and the temperature were taken into account in the calculation of the atmospheric corrections to the raw data (Table 3 and 4).

I the case of the $S1_{charged}$ channel, the mean value of the correction coefficient by temperature represents only the 5.9% of the mean value of the total correction coefficient, for the $S2_{charged}$ channel it represents the 18.6% of the mean value of its total coefficient and for the $S3_{charged}$ channel, it represents the 17.9% of its total coefficient (see Table 5).

In the case of the analysis of the selected FDs using data corrected by pressure, and by pressure plus temperature, the minimum relative difference was found in the event of August 05, 2011, reaching a relative difference of 0.01, while the biggest difference was obtained is in the case of the event of April 05, 2012 with the -0.07 (deeper falls in the counting rates corrected by pressure) and in the case of the event of April 14, 2013, with the 0.07 (Table 6), which lies in the margin of uncertainties for channels $S2_{charged}$ and $S3_{charged}$. Those arguments lead to establish (as was discussed in comments of Table 5 and 6) that the prevailing atmospheric parameter to perform the correction of the SNT-SN counting rates is the barometric pressure. The contributions of the temperature coefficients to the estimation of the total decrease values are not significant, since these contributions lie in the margins of uncertainty of the total decrease values (see Table 6 and SNT-SN averaged decrease values in Table 8), therefore, the temperature can not be considered as a factor for computing the correction coefficients.

When FD data for the SNT-SN were compared with those of the NMCDMX, an appreciable difference in the records of the FD minima on both monitors is significant. The Rigidity Response Mean Value of both stations was similar, but the difference in atmospheric depth can perfom the most relevant role in the differences found, since for the lower energy components of the secondary shower, the atmospheric absorption reaches at least an order of magnitude. A general conclusion of the present evaluation would be that, due to a diurnal variation of large amplitude (about (1.6 – 3)%, Table 7), the SNT-SN is not a reliable instrument for the analysis of FDs whose minimum value is less than 5% of the quiet day reference line. However, it is remarkable that the SNT-SN is widely and successfully used as instrument for measuring activity of secondary cosmic rays and neutron solar activity.

Acknowledgements

UNAM personnel (Marco Barrantes, José Francisco Valdés Galicia, Luis Xavier González, Octavio Musalém, Alejandro Hurtado, Ernesto Ortíz, Rocío García, Marcos Anzorena and Roberto Taylor) thanks to INAOE authorities for the continued use of facilities at Sierra Negra that allowed the continues operation of the SNT. Likewise, we would like to express our acknowledgement to Dr. Esperanza Carrasco and Dr. Alberto Carramiñana for providing us data of the INAOE-SN station, without which we would not have been able to complete our analysis.

Partial support to CONACyT grant 180727 and UNAM PAPIIT grant IN-104114 are also acknowledged. Marco Barrantes thanks CONACyT for the granting of a scholarship during his PhD studies at UNAM.

EN LAS REFERENCIAS SE PONEN TODOS LOS AUTORES Y EL ET AL SE PONE EN EL TEXTO.

References

Clem, J. M., & Dorman, L. I. (2000). Neutron Monitor Response Functions. Space Science Reviews , 93, 335-359.

Carrasco, E., Carramiñana, A., Avila, R., Gutiérrez, C., Avilés, J. L., Reyes, J., *et al*. (2009). Weather at Sierra Negra: 7.3-yr statistics and a new method to estimate the temporal fraction of cloud cover. Monthly Notices of the Royal Astronomical Society , 398, 407.

Abbrescia, M., Aiola, S., Antolini, R., Avanzini, C., Baldini Ferroli, R., Bencivenni, G., *et al*. (2011). Observation of the February 2011 Forbush decrease by the EEE telescopes. The European Physical Journal Plus, 126, 61.

Augusto, C. R., Kopenkin, V., Navia, C. E., Tsui, K. H., Shigueoka, H., Fauth, A. C., *et al*. (2012). Variations of the Muon Flux at Sea Level Associated with Interplanetary ICMEs and Corotating Interaction Regions. The Astrophysical Journal , 759, 143.

Blackett, P. M. (1938). On the Instability of the Barytron and the Temperature Effect of Cosmic Rays. Physical Review , 54, 973-974.

Barrantes, M., Valdés-Galicia, J. F., González, L. X., Carrasco, E., Carramiñana, A., Reyes, J., *et al*. (2018). Atmospheric variability at the summit of Sierra Negra, Mexico, from 2012 July to 2015 October. Monthly Notices of the Royal Astronomical Society , 473, 3299-3311.

Bertou, X. (2011). Background radiation measurement with water Cherenkov detectors. Nuclear Instruments and Methods in Physics Research Section A: Accelerators, Spectrometers, Detectors and Associated Equipment , 639, 73-76.

Braun, I., Engler, J., Hörandel, J. R., & Milke, J. (2009). Forbush decreases and solar events seen in the 10-20 GeV energy range by the Karlsruhe Muon Telescope. Advances in Space Research, 43, 480-488.

Dasso, S., Asorey, H., & Collaboration, F. T. (2012). The scaler mode in the Pierre Auger Observatory to study heliospheric modulation of cosmic rays. Advances in Space Research , 49, 1563-1569.

De Mendonça, R. R., Raulin, J.-P., Echer, E., Makhmutov, V. S., & Fernandez, G. (2013). Analysis of atmospheric pressure and temperature effects on cosmic ray measurements. Journal of Geophysical Research: Space Physics , 118, 1403-1409.

Deggeroni, V., Echer, E., Dal Lago, A., Hammerschmitt, B. K., Bremm, T., Rockenbach, M., *et al*. (2013). Cosmic ray decreases caused by interplanetary shocks observed by the muon telescope at Sao Martinho da Serra, Southern Brazil. 33rd International Cosmic Ray Conference, Rio de Janeiro, 2013. The Astroparticle Physics Conference.

Dorman, L. I. (2004). Cosmic Rays in the Earth's Atmosphere and the Underground. Netherlands.: Kluwer Academic Publishers.

Dumbovic, M., Vrsnak, B., Calogovic, J., & Karlica, M. (2011). Cosmic Ray Modulation by Solar Wind Disturbances. Astronomy & Astrophysics , 531.

González-Méndez, L. X. (2010). El Telescopio de Neutrones Solares en Sierra Negra y aceleración de los iones en la atmósfera solar. Ph.D. dissertation, National Autonomous University of Mexico, UNAM.

Miroshnichenko, L. I. (2011). Physics of the Sun and solar-earth relations. University book, Moscow.

Musalém, O. (2015). Análisis de los fenómenos solares e interplanetarios causantes de decrecimientos Forbush en los rayos cósmicos. Master's thesis, National Autonomous University of Mexico, UNAM, M\'exico City.

NOAA. (2004). K-Indexes, 2004.

NOAA. (2005). K-Indexes, 2005.

Okike, O., & Collier, A. B. (2011). A multivariate study of Forbush decrease simultaneity. Journal of Atmospheric and Solar-Terrestrial Physics , 73, 796-804.

Ortiz, E., Valdés-Galicia, J. F., Matsubara, Y., & Nagai, Y. (2016). Observation of cosmic ray hadrons at the top of the Sierra Negra volcano in Mexico with the SciCRT prototype. Advances in Space Research , 58, 2018-2025.

Patrignani, C., & others. (2016). Review of Particle Physics. C40 , 100001.

Pintér, T., Rybanský, M., Kudela, K., & Dorotovic, I. (2011). Peculiarities in Evolutions of Cosmic Radiation Level after Sudden Decreases. Sun and Geosphere , 6, 23-26.

Richardson, I. G., & Cane, H. V. (2011). Galactic Cosmic Ray Intensity Response to Interplanetary Coronal Mass Ejections/ Magnetic Clouds in 1995--2009. Solar Physics , 270, 609-627.

Shibata, S. (1994). Propagation of solar neutrons through the atmosphere of the Earth. Journal of Geophysical Research: Space Physics , 99, 6651-6665.

Subramanian, P. (2009). Forbush Decreases and Space Weather. Bangalore - 560034, India: Indian Institute of Astrophysics.

Valdés-Galicia, J. F., Muraki, Y., Tsujihara, H., Sako, T., Musalem, O., Hurtado, A., *et al*. (2004). An improved solar neutron telescope installed at a very high altitude in Mexico. Nuclear Instruments and Methods in Physics Research , 535, 656.

Appendix. Plots for the section 4

In Figure A-1 - Figure A-6 the scatter plots of normalized counting rates as a function of barometric pressure, temperature and relative humidity variations are presented. β_p, C_T and C_{RH}, $\Delta\beta_P$, ΔC_T and ΔC_{RH} represent the value of the respective coefficient and its standard deviation, calculated by linear regression. In addition, the value of the Pearson correlation coefficient and the standard deviations of the data of each axis are shown in the plot upper insert.

Figure A-1 shows the linear fit for the normalised counting rates in channel S3 for neutral particles vs ΔP. From

$$\frac{\Delta N}{\overline{N}} = \beta_P \, \Delta_P \qquad (11)$$

and from the values shown in the graph, it follows that $\beta_{S3_{neutral}}$ = (-0.490±0.031)%/mbar is the value of the pressure correction coefficient for $S3_{neutral}$ channel.

When the normalised counting rates on the $S3_{charged}$ channel for this period were analysed, the next dispersion plot was obtained.

Figure A-2 shows the linear fit for the normalised counting rates of the S3 charged particle channel vs ΔP. Using equation (11) $\beta_{S3_{charged}}$ = (-0.515±0.023)%/mbar, the value of the pressure correction coefficient for S3 charged particles channel was obtained.

Based on the information provided in Figure A-3, we deduce that the pressure correction coefficient for the neutral channel S3neutral is $\beta_{S3_{neutral}}$ = (-0.536±0.033)%/mbar.

From the information in Figure A-4t the correction coefficient by pressure for the S3charged channel is $\beta_{S3_{charged}}$ = (-0.544±0.027)%/mbar was obtained.

From the information in the Figure A-5 the correction coefficient by temperature for the S3charged is $\beta_{S3_{charged}}$ = (-0.138±0.008)"%/mbar was obtained.

From the information in Figure A-6 the correction coefficient by temperature for the S3charged channel is $\beta_{S3_{charged}}$ = (-0.122±0.006)%/mba was obtained.

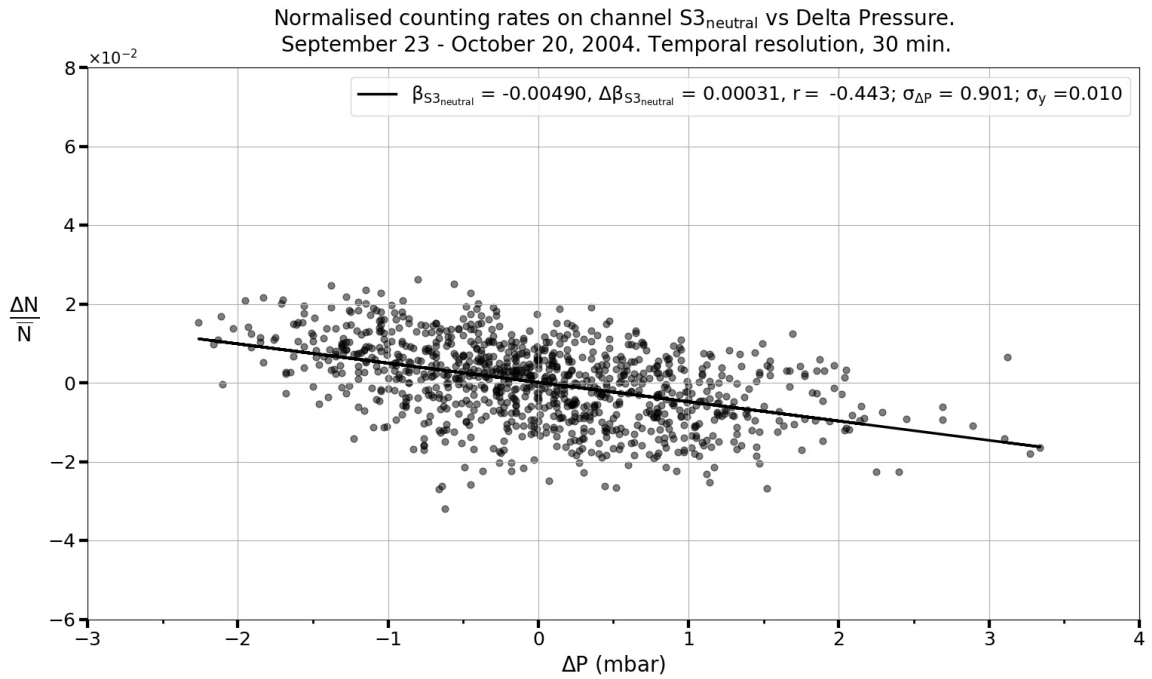

Figure A-1. Normalised counting rates on channel S3 for neutral particles vs the variation of the pressure with respect to its average value for the interval of 23 of September to 20 of October of 2004. The straight line is the result of a linear correlation whose calculated parameters are in the upper insert.

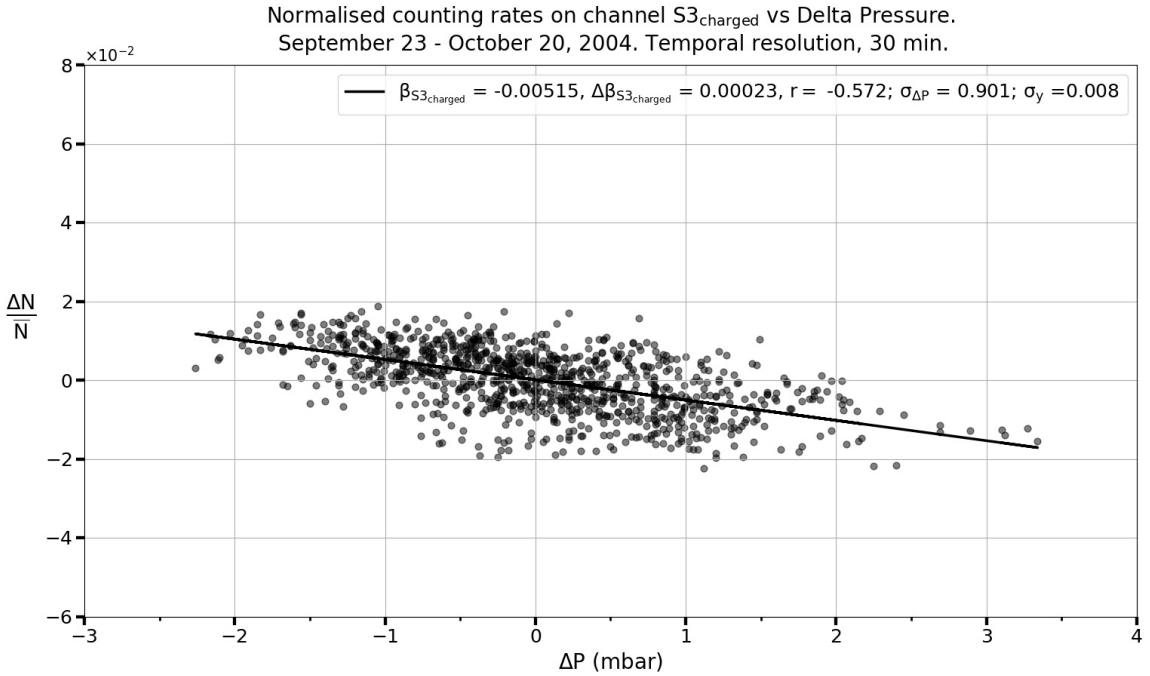

Figure A-2. Normalised counting rates on S3 channel of charged vs. the variation of the pressure with respect to the mean value for the interval from September 23 to October 20, 2004.

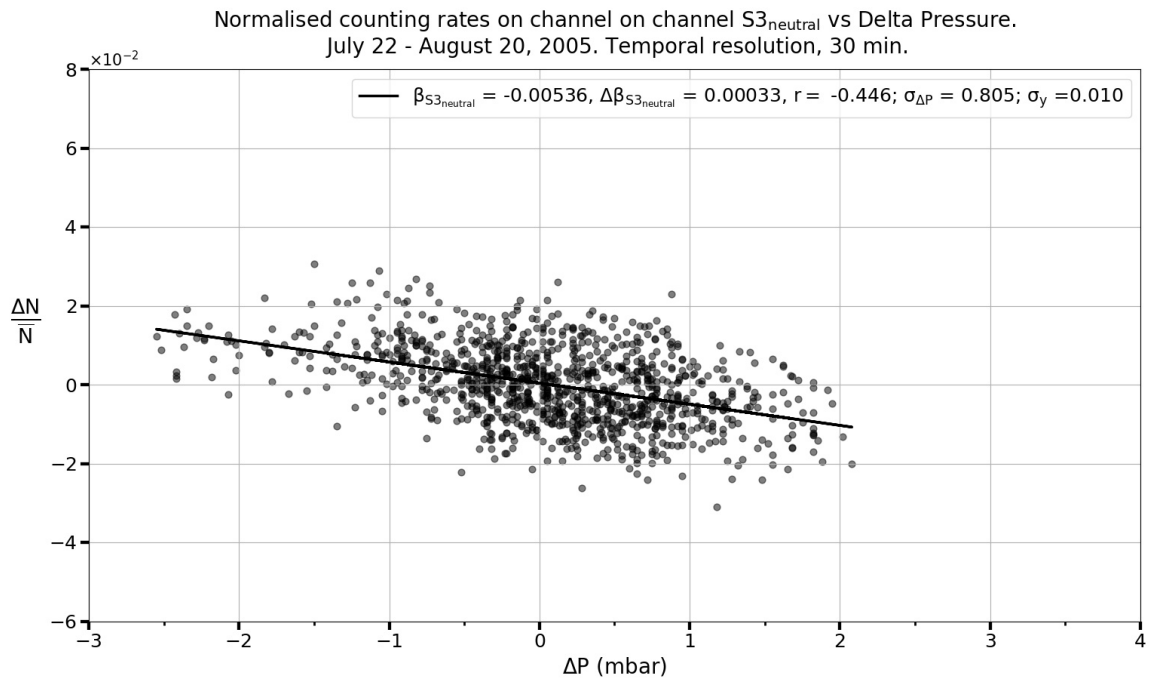

Figure A-3. Normalised counting rates on channel S3 neutral vs variation of pressure, from July 22 to August 20, 2005.

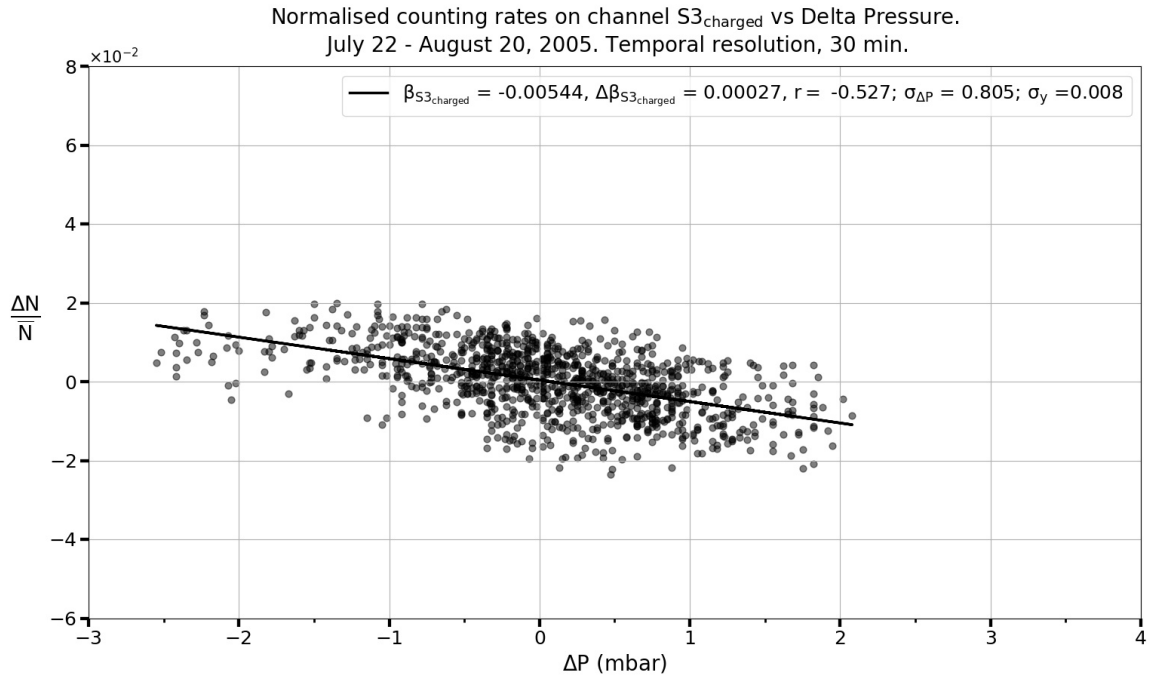

Figure A-4. Normalised countig rates on S3 channel of charged vs. the variation of the pressure with respect to the mean value for the interval from September 23 to October 20, 2004, of the pressure data recorded by the INAOE-SN station.

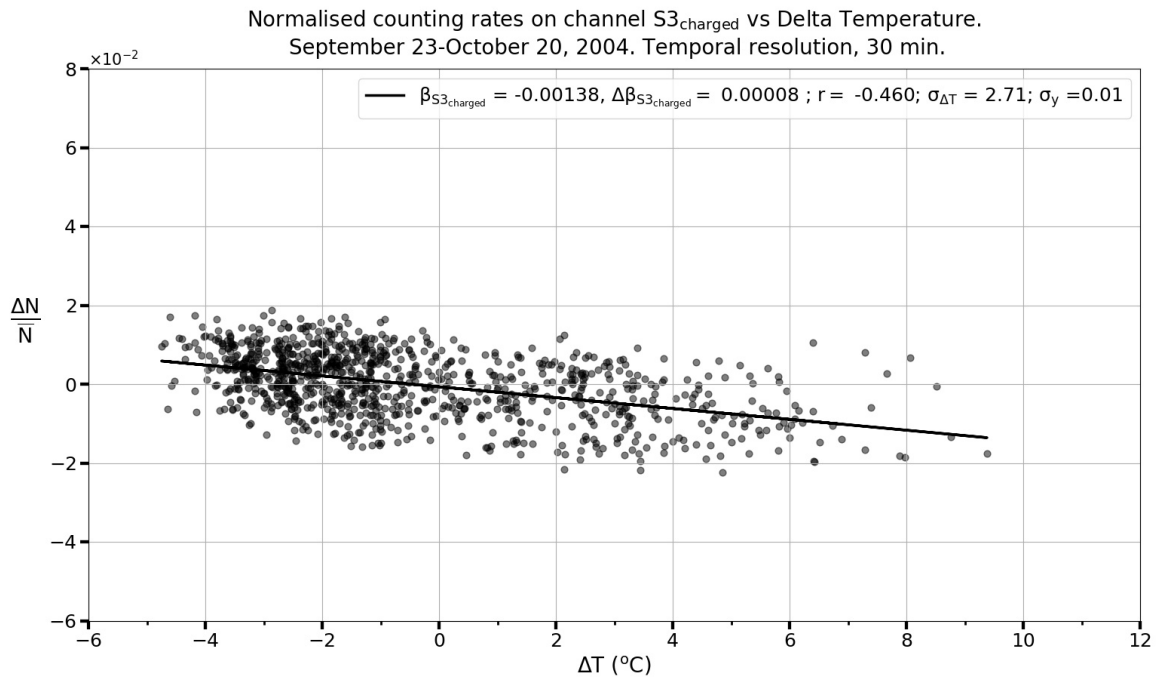

Figure A-5. Normalised countig rates on S3 channel of charged vs. ΔT with respect to the mean value for the interval from September 23 to October 20, 2004, of the pressure data recorded by the INAOE-SN station.

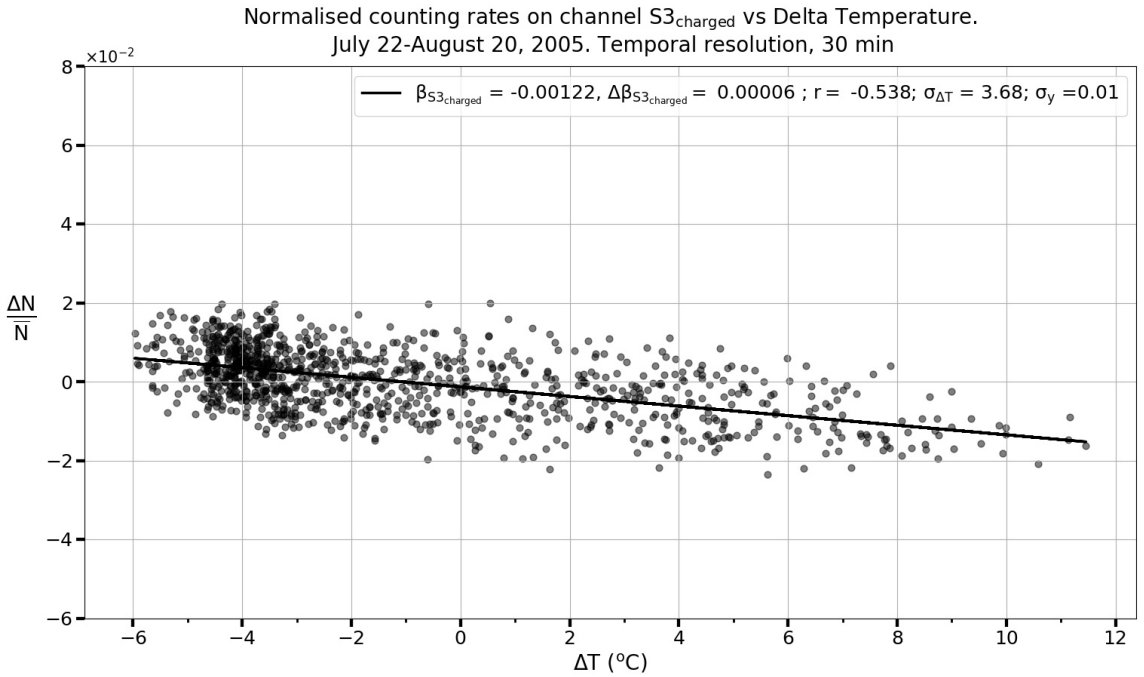

Figure A-6. Normalised countig rates on S3 channel of charged vs. Delta Temperature with respect to the mean value for the interval from July 22 to August 20, 2005.

Geofísica Internacional (2018) 57-4: 275-287

Original paper

Integration of electrical resistivity tomography with electromagnetic and soil radon measurements for characterizing the leakage problem in Afamia B dam, Syria

Walid Al-Fares and Mohamed Al-Hilal*

Received: April 13, 2017; accepted: Sepotember 09, 2018; published on line: October 03, 2018

Resumen

Para comprobar las causas de fuga en la presa Afamia B, y proponer un modelo conceptual, se aplicaron tres técnicas complementarias que incluyen datos tomográficos de resistividad eléctrica (ERT, por sus siglas en inglés), electromagnetismo (EM) y radón gaseoso del suelo. Los datos se acompañan por una investigación geológica y tectónica extensa, las cuales ayudaron a delimitar ciertas vías para una posible filtración de agua desde la cuenca de la presa del lago. Se localizaron zonas significativamente débiles, que incluyen lineamientos tectónicos subsuperficiales, roca fracturada, superficies erosionadas y algunas otras estructuras deformadas. Un análisis adicional de los datos indicó que la estructura geológica subyacente de la cuenca de la presa se compone principalmente de un lecho litológico sucesivo que consiste en capas permeables (arenas y gravas), que se alternan con lechos de margas calcáreas impermeables. La composición heterogénea de tales litofacies puede proporcionar una razón adicional que podría mejorar efectivamente las pérdidas de agua a través de las unidades permeables a lo largo del valle principal. Los resultados generales de las técnicas combinadas han mostrado una correlación positiva entre los métodos aplicados y confirmaron la utilidad de este enfoque para trazar estructuras deformadas ocultas y zonas débiles. Además, la existencia de numerosas ruinas arqueológicas, como tumbas y pozos distribuidos en toda la cuenca de la presa, puede aumentar considerablemente la fuga de agua del lago. En consecuencia, se ha encontrado que el lecho de roca erosionado, la heterogeneidad de los lechos alternados y otras características superficiales detectadas están desempeñando un papel crucial en los procesos de fuga vertical y subhorizontal que ocurren dentro de las formaciones de Neogene y pasan a carbonato cárstico profundo y de rocas de la edad cretácica.

Palabras clave: Técnicas geofísicas, ERT, EM, Levantamiento de radón del suelo, fugas de agua, presa de Afamia, Siria.

Abstract

Three complementary techniques, including Electrical Resistivity Tomography (ERT), Electromagnetic (EM) and soil gas radon measurements were applied in order to propose a conceptual model that may describe the main causes of water leakage in Afamia B dam. The survey was accompanied by extensive geologic and tectonic field investigations which assisted the delineation of certain pathways for possible water leakage from the basin of the lake's dam. Significant weak zones including subsurface tectonic lineaments, fractured bedrock, eroded surfaces, and some other deformed structures were characterized. Further analysis of the resultant data indicates that the underlying geological structure of the dam basin is primarily composed of a successive lithological bedding consisting of permeable layers (sands and gravels) alternating with impermeable calcareous marl beds. The heterogeneous composition of such lithofacies may provide an additional reason which could effectively enhance the water losses through the permeable units along the shoulders of the main valley. The overall results of the combined techniques have shown a positive correlation between the applied methods, and they confirmed the usefulness of such approach for mapping out hidden deformed structures and weak zones. Moreover, the existence of numerous archeological ruins such as graves and wells distributed throughout the dam basin may greatly increase the water leakage from the lake. Consequently, it has been found that the eroded bedrock, the heterogeneity of alternating beddings and other detected subsurface features are all playing a crucial role in the subhorizontal and vertical leakage processes that occurring within the Neogene formations and passing down to deep-seated karstified carbonate rocks of Cretaceous age.

Key words: Geophysical techniques, ERT, EM, Soil radon survey, Water leakage, Afamia dam, Syria.

W. Al-Fares
M. Al-Hilal*
Department of Geology
Atomic Energy Commission of Syria
P.O Box 6091, Damascus, Syria
*Corresponding author: cscientific8@aec.org.sy

Introduction

Afamia dams are located on the eastern margin of the Ghab plain in the northwestern part of Syria, close to Qalet Al-Madiq town (Figure 1). The Ghab plain constitutes a prominent fertile terrain in western Syria that suitable for growing a wide range of agricultural activities. Hence, three adjacent earth-filled dams, (A, B and C), were constructed nearby the great ancient city of Afamia, at about 3 km eastern margin of the Ghab basin. In fact, the Afamia dams were built in this area essentially to divert some water out of the Orontes River (Nahr El-Aasi) to be stored and used afterward for irrigation and other domestic uses during drier months of late summer and autumn. The dam B, which has the maximum storage capacity of 37 millions cubic meters, is subjected to serious problems of leakage through the bedrock of its reservoir. It is worth to mention that the dam body extends along 2870m, with 55m high and it has a constant elevation of 282m above sea level (a.s.l.). In 1999, the dam was set in operation and filled up with water for the first time in order to check its validity for water storage. However, the water level in the lake has shown a clear sign of water loss ranged between 17 and 20 cm per day. Therefore, several geological and geophysical investigations, including vertical electrical soundings (VES) and electrical profiling (EP) surveys, have been carried out in dam by the Syrian General Company of Hydraulic Studies (2001). The objective of their surveys was to characterize the geological and tectonic settings of the dam site. Additionally, some foreign consulting companies performed more hydrogeological and geophysical investigations (Minasian, 2001). The results of these studies revealed various anomalies which indicate some probable scattered zones of infiltration distributed in many parts of the dam lake, but the exact pathways of leakage were not defined precisely. Further assessments of the pervious works were fulfilled by a Swiss company in attempt to identify the problem and to better understand the origin of water leakage (Joos and Bussard, 2004).

Moreover, new contribution was achieved in order to solve the leakage issue in the dam using more adequate geophysical techniques including electrical resistivity tomography (ERT) and electromagnetism (EM), surveys in addition to soil gas radon measurements (Al-Hilal and Al-Ali, 2010; Al-Fares, 2011). The objectives of these approaches were to characterize the subsurface structure of the dam floor and thereby delineate the main geologic and tectonic features that might be responsible for water leakage in the concerned dam.

The electrical resistivity tomography technique is recognized as one of the most important geophysical method which has been rapidly developed and widely used in the last few years (Demanet *et al*., 2001; Van Schoor, 2002; Paula *et al*., 2004; Nguyen *et al*., 2007; Lin *et al*., 2013; Torres-Rondon *et al*., 2013; Khaki *et al*., 2014; Farzamian *et al*., 2015). This technique became quite common method particularly in hydrogeological studies, dam leakage problems and for characterizing subsurface geological structure. This is due to the quality of the acquired data, and the ability of obtaining a continuous underground coverage with more details in 2D and 3D spaces (Panthulu *et al*., 2001; Pham *et al*. 2002; Cho and Yeom, 2007; Sjodahl *et al*., 2010; Al-Fares, 2014; Gutierrez *et al*., 2015). On the other hand, the Slingram electromagnetic technique (EM) can be considered as a practical tool for performing a fast geoelectrical survey in dam's terrains. This technique is proved to be suitable in various geological and hydrogeological conditions, in addition to the detection of different subsurface objects such as buried channels, underground caves and other buried archaeological occurrences (McNeill, 1990; Guerin *et al*., 2004; Perez-Gracia *et al*., 2009; Novo *et al*., 2012; Anchuela *et al*. 2015). Soil gas radon is broadly recognized as a significant natural tracer which can be used for locating a potential fault zone and providing an insight into some hidden structural features that are covered by a thick cover of recent sediments (King *et al*. 1996; Ciotoli *et al*. 1999; Baubron *et al*. 2002; Al-Hilal and Aissa 2015). Moreover, the application of integrated geophysics and soil gas radon surveys was proved as a reliable approach for the delineation of buried fault zones (Zarroca *et al*. 2012; Claudia Schütze *et al*. 2016). Accordingly, the current work represents a joint effort of integrating the results of the electrical resistivity tomography and electromagnetic surveys in combination with soil gas radon measurements, in attempt to identify the accurate locations of the leakage zones close to the Afamia B dam body

Geological and Hydrogeological Settings

The study region is generally situated within a geologic calcareous syncline of Cretaceous age, covered by thick continental formation of Neogene sediments, on which the Afamia dams have been constructed (Figure 1). The area is separated by a number of striking faults that led

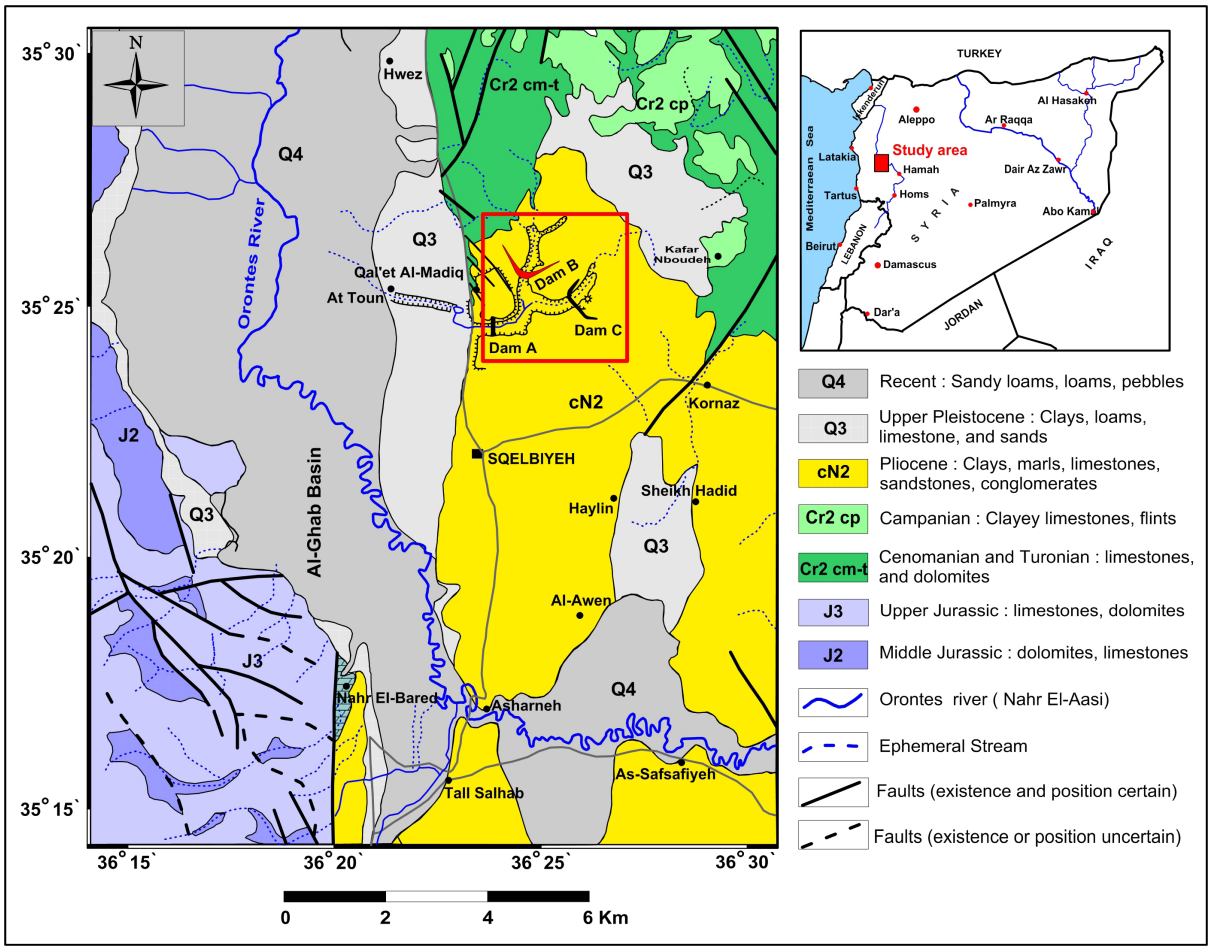

Figure 1. Simplified geological map of the study area showing the locations of Afamia dams (modified after Ponikarov, 1966).

to the formation of several distinct lineaments and tectonic blocks. Locally, the dam's site represents gently rolling hills characterized by thick Pliocene lacustrine sediments that developed in low areas, and covered by a thin sheet of Pleistocene and Recent formations. The prevailing Neogene deposits consist basically of marls and calcareous marls alternating with sands, gravels and conglomerate formations, with a total thickness of more than 100m. The Neogene formations are covered by thin unconsolidated layers of Quaternary deposits which are composed mainly of reddish clays, silts, sandy clays and alluvium sediments. Cretaceous rocks of Cenomanian and Turonian ages consist mostly of fractured and karstified limestone and dolomite rocks. These calcareous formations are partially outcropped on the northwest flank of the dam's area, and they appear to extend underneath the Neogene sediments forming the bottom of the stratigraphic succession in the area (Ponikarov, 1966). From tectonic point of view, the dam's area is located close to the Ghab pull-apart basin that formed initially as a result of the tectonic evolution of the northern left-lateral Dead Sea Fault System (DSFS) in western Syria (Brew *et al*., 2001). In view of that, the study site is struck by many distinctive fault segments some of which are bounding the Ghab basin and some others are branching out from the main extension of the northern DSFS. Additionally, the probable occurrences of karstification especially in the subsurface calcareous rocks may indicate that the underlying structure of the dam's area is highly fractured, and thereby the permeability is feasible for water infiltration through the floor of the reservoir. Since these geologic features and tectonic lineaments are not obviously visible at the surface of the dam basin, so it is very important to trace their pathways and pursue their subsurface extensions towards B dam particularly where the most loss of water is taking place. From hydrogeological point of view, the main groundwater aquifer in the study

region belongs to the Cenomanian-Turonian fractured rocks, where a number of natural karstic springs are emerging from the eastern bounding fault of the Ghab basin. The second aquifer is related to the Neogene sediments, which appears on the surface through several springs, scattered in the study area. The absolute water table level of the Neogene aquifer ranges between 215 to 220m (a.s.l.), and the general direction of the ground water flow is trending from east towards west, with slight hydraulic gradient (Ponikarov, 1966).

Methodology

Electrical Resistivity Tomography (ERT)

Electrical resistivity tomography (ERT) is a sufficient and reliable geophysical technique for recognizing shallow subsurface structures. The method provides qualitative information of the electrical characteristics of the penetrated geological formations, and it delineates an expressive image of the subsurface features. An ERT survey is a combination of sounding and profiling configurations, which includes a number of electrodes with a fixed inter-electrode spacing. This technique depends on the measurement of subsurface apparent resistivity ρ_a (Ω.m) of the ground according to Ohm's law:

$$\rho_a = k\,(\Delta v/I)$$

Where k: a geometric constant that depends on the inter-electrodes spacing; Δv: the measured potential difference in mV; and I: the applied electric current in mA.

The measured apparent resistivity is converted into true resistivity using inversion software in order to obtain a 2D geoelectrical cross-section, which can be thereafter interpreted from geoelectrical or geological point of view. In the present work, the Wenner-Schlumberger configuration were applied. The advantages of this configuration are the stability and the ability to identify horizontal and vertical subsurface features. In addition, the Wenner-Schlumberger configuration provides a good signal/noise ratio for the measurements and permits getting full density of data at different levels of depth. (Dahlin and Zhou, 2004; Candansayar, 2008).

In the framework of this study, two main profiles (ERT-P1 and ERT-P2) were chosen in the lake close to the dam body (Figure 2). The first one is extending close to the central part of the dam body and it is perpendicular to the main valley, while the second is stretching along the left bank of the dam basin in parallel line to the course of the main valley. The geoelectrical instrument Syscal Swich-72 multi-core cable was used to carry out the ERT profiles. According to the applied configuration, the ERT profile was consisting of a main sequence of 72 electrodes straightly arranged along the measurement profile. The main sequence is almost followed by many roll-along sequences of 36 electrodes for each one depending on the length of the profile. The two performed ERT profiles have a length of 430 and 320m, with 3m as an electrode spacing step. The raw data were recorded using Schlumberger-Wenner sequence, where the penetration depth could reach, in this case, up to 30m. This sequence includes 759 measurement points distributed on 16 levels of depth. The acquired data were inverted into 2D real resistivity section using the RES2DINV software (Loke and Barker, 1996). The coordinates and the topographical survey of each profile were determined by using the GPS system with Universal Transversal Mercator (UTM) projection.

Electromagnetic survey

The Slingram electromagnetic method was used, in this study, as an additional and supportive tool in order to characterize the shallow subsurface zones or non homogenous geological mediums. This technique has been proven its performance as a practical tool combined with ERT technique in many occasion around the world (Soupios *et al*., 2007; Cygal *et al*., 2016; Osinowo *et al*., 2018).

The measurements carried out by using the CM-031 device, made by the Czech GF-Instrument. This device is practical and fast for performing a geoelectrical survey because it doesn't require any direct connection with the ground. The investigation depth which could be achieved is about six meters and the operating frequency is 9.8 kHz. Two EM profiles (EM-P1 and EM-P2) fulfilled in accordance with the ERT sections (Figure 2), in order to verify some anomalous features obtained by the ERT survey. The length of each EM profile is about 200m, and they both run in parallel lines with the ERT profiles, with 3 to 4m interval distance.

Radon measurement technique

The application of soil gas radon technique for detecting hidden deformed structures is based on the principle that anomalously high radon emission is commonly observed on the surface above fractured zones because of the higher permeability of such structures compared to the surrounding geologic medium.

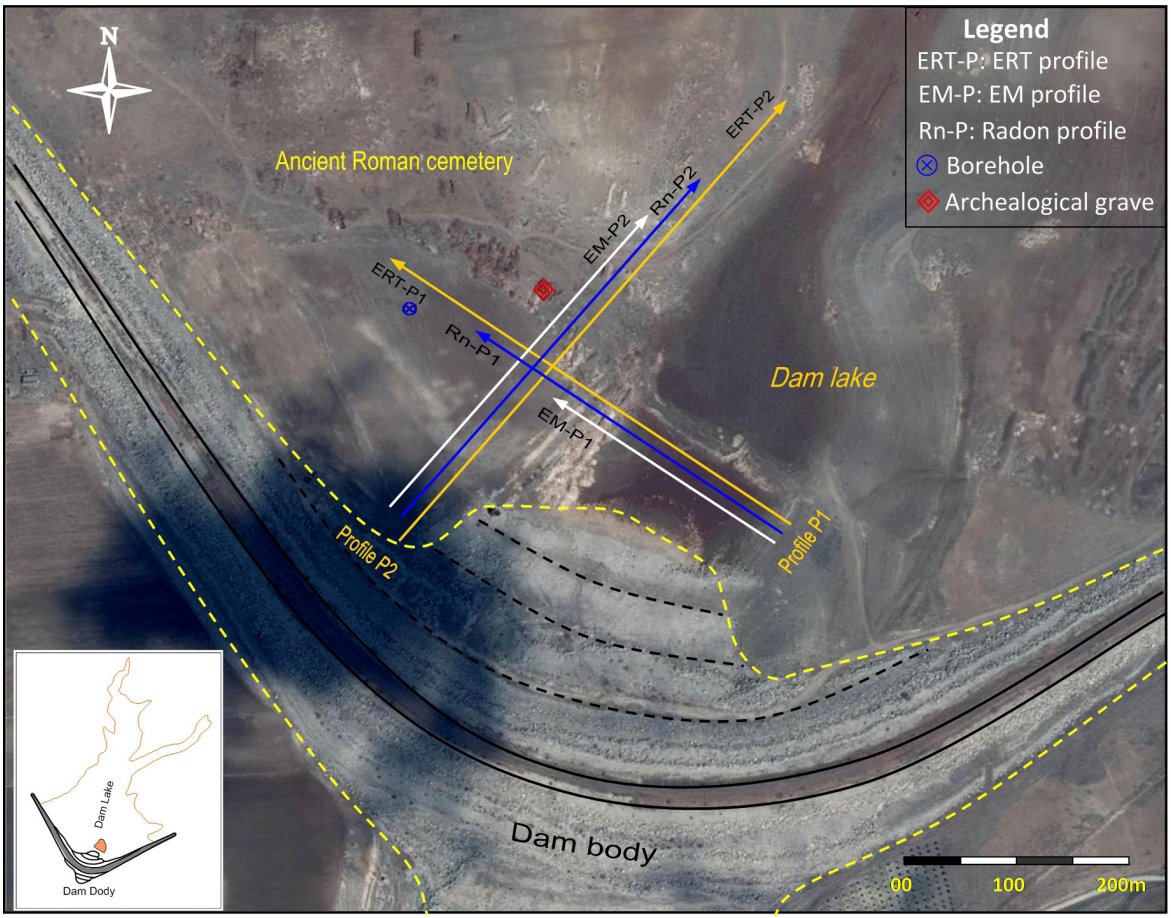

Figure 2. Locations of the ERT, EM and soil radon measurement profiles carried out in the lake of Afamia B dam.

Therefore, the method has been proven as a useful tool for locating the position and trend of buried faults in many tectonic regions throughout the world (Fu *et al*., 2005; Swakon *et al*., 2005; Al-Hilal and Abdul-Wahed 2016).

Direct active method was applied in this survey for determining the concentration of radon in soil gas. The method is based on the use of a portable vacuum soil probe assembly, which allows direct quantitative radon soil gas determinations in the field. The system consists of three attached parts including a portable soil probe assembly model (Pylon-154), a vacuum hand pump and a scintillation Lucas cell model (Pylon-110A). Radon sampling stations were arranged along a measuring profile with a certain interval distance between points. In the field, a hole of 60 cm depth and 5cm diameter is dug in the ground at each sampling station and a special PVC tube is planted inside the hole in order to prevent collapse of the soil. The soil gas is sampled into an evacuated scintillation cell by inserting the vacuum soil probe into the hole and slowly opening the probe valve until the system comes to the atmospheric pressure. After each measurement, the radon sample must be allowed to decay inside the scintillation cell for three hours so that the radon daughters come into equilibrium with the radon. Then, the scintillation cell is placed into the counter (RM 1003-Radon Detector), where the alpha activity is measured in count per minute basis, and then converted to concentration as Bq/m^3. In this study, two radon measurements profiles (Rn-P1 and Rn-P2) were carried out in parallel line with the ERT and EM profiles (Figure 2). Each radon profile consists of 21 sampling points at interval distance of 10-15m.

Results and discussion

The overall obtained results of the integrated techniques of the ERT, EM and Rn measurements revealed a fairly good correlation which may possibly point to some important subsurface deformed structures or buried fractured zones (Figures 3 and 5). The geophysical survey of

the included methods carried out along two intersected measuring profiles, denoted as P1 and P2, traversing the main basin of the Afamia dam lake as shown in figure (2). The following sections include detailed discussion and interpretation of the results obtained along both measuring profiles.

Interpretation of the P1 profile

The figure (3) shows the interpretation of the P1 profile, which includes the combination of the ERT-P1, EM-P1 and Rn-P1measuements. The geoelectrical ERT section reveals the presence of thick clay and alluvial deposits layer covering most of the main valley which extends along a distance of 144m. The thickness of these deposits reaches up and more than 10m in some parties. In the middle of the main valley (X= 96m of the ERT section), the alluvial deposits extend downward towards the deeper formations. The extension of the alluvial deposits, in this form, could be resulted by the effect of the leakage of water laden with sediments towards the underline eroded layers (Figure 3).The resistivity values of these deposits seems to be relatively low and vary between 7-20 Ω.m. These deposits lay over eroded and fractured bedrock which is consisted essentially of marls and calcareous marls. The resistivity values of this bedrock are ranging between 50 and 120Ω.m with a thickness could reach more than 20m depending to the applied configuration and the used electrodes spacing step (Wilkinson *et al*., 2006; Szalai *et al*., 2013).

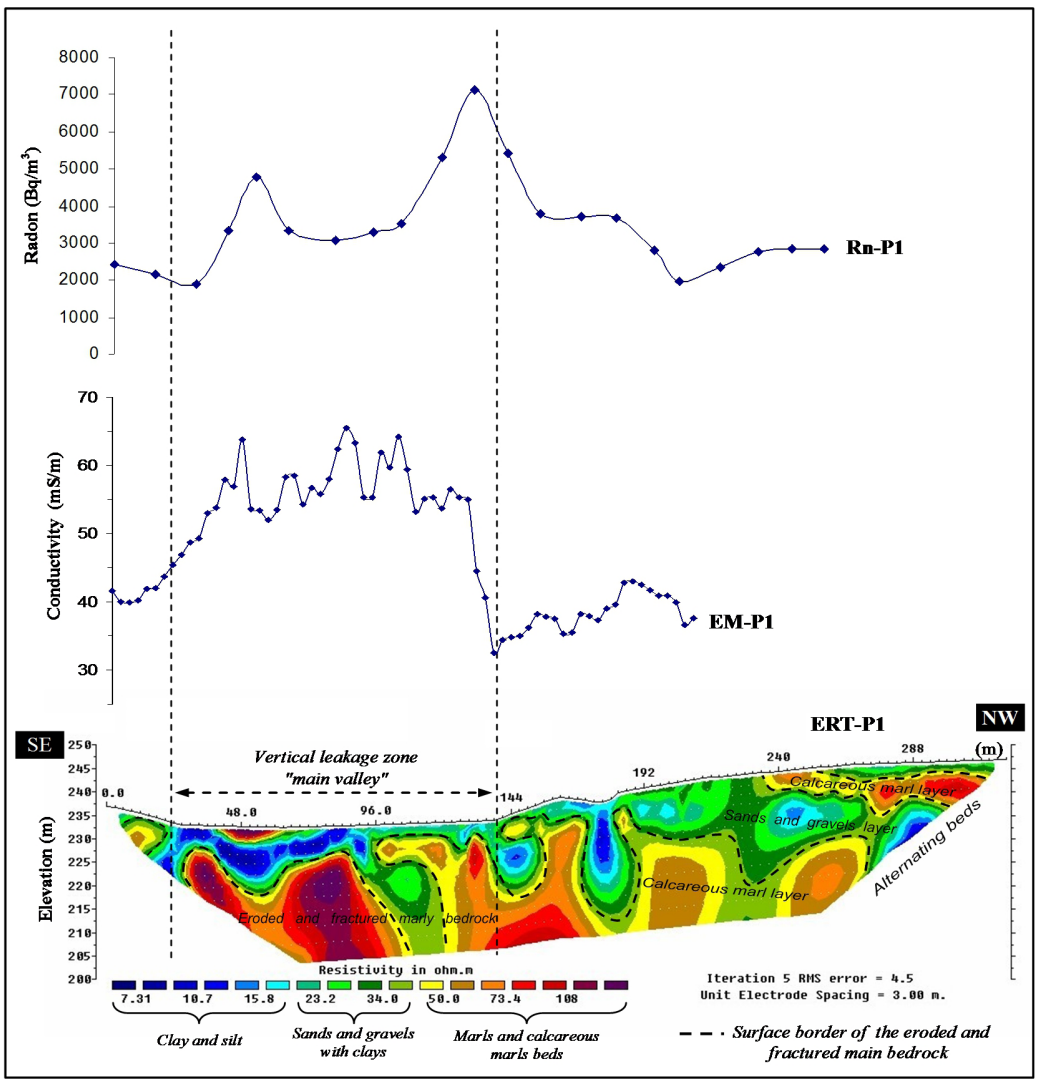

Figure 3. Interpretation of the P1 profile which includes the ERT, EM and soil radon measuements that carried out in Afamia B dam.

In principle, the marly and calcareous marly bed is supposed to be compact and impermeable, but the erosion and tectonic activities deformed its natural feature. It is evident that, the erosion and deformation processes applied on the marly and calcareous bedrock made it permeable and enhance the water to be leached towards the deeper formations. Moreover, the edges of the main valley seem to be associated with local tectonic features, which eventually led to the formation of the present valley in the site. The margins of the valley as well as the irregularity of the marly bedrock surface, which are effectively eroded and deformed, appear to be the principle causative of the vertical leakage in the dam lake. Moreover, the geoelectrical ERT section reveals also a clear alternating lithological succession between sands, gravels and clay layers alternating with marls and calcareous marls beds (Figure 3). The heterogeneity of these beds contributes in certain way by the occurrence of sub-horizontal water leakage through the permeable formations (sandy and gravels sediments) especially when the water storage level begins increasing in the lake. This kind of leakage is almost transformed afterwards to a vertical leakage through the eroded and fractured zones. The alternating bedding, which has been revealed by the ERT section, is confirmed through the comparison with real information of a borehole lithological column drilled close to the dam body (Figure 2 and Figure 4).

With respect to the curve of the EM conductivity (Figure 3), it seems to be well correlated with the inverted ERT-P1 section. The high electrical conductivity values are related with the clay deposits that accumulate within the course of the main valley, where the values reach 70mS/m (≈14Ω.m). However, a sudden decrease of the EM curve appeared to be well corresponded with the margins of the main valley. This decrease could be due to lithological changes between clay deposits from one hand and sands and gravels from other hand, where the conductivity values decrease to reach less than 30 mS/m (≈ 33 Ω.m).

Concerning the radon concentration along the measuring profile (Rn-P1), two notable increases values were noticed at distances of 60m and 145m from the start point of the ERT-P1 section. The first small radon peak was found to be directly correlated with a higher permeability structure due to the presence of subsurface fractured zones close to the left edge of the main valley. The second anomalous soil radon signature was also recorded above the site of a major fracture, which

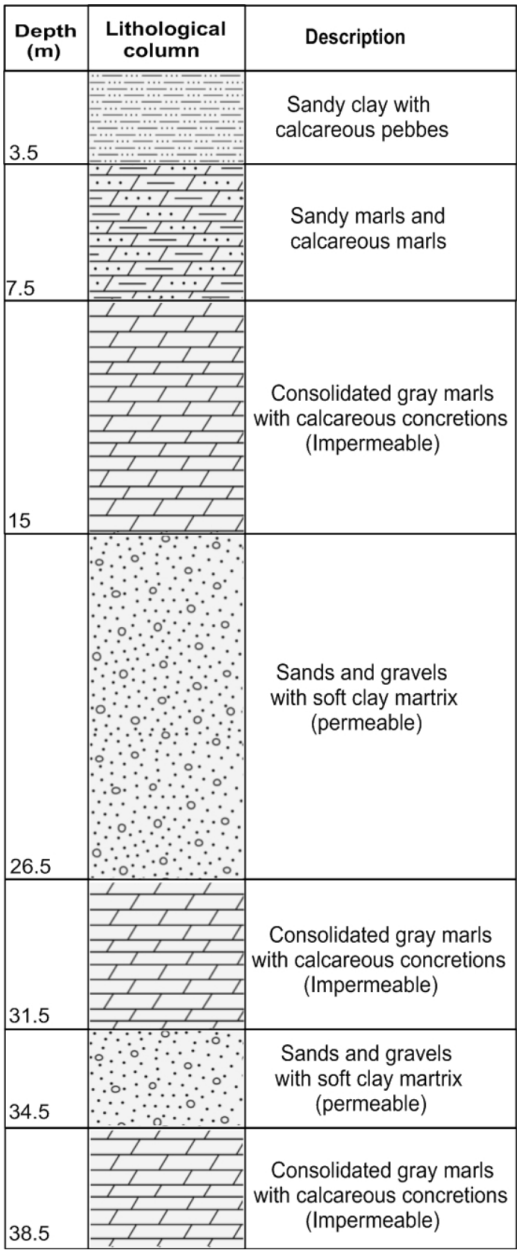

Figure 4. A borehole column illustrates the lithological succession close to the dam body (after the Syrian General Company of Hydraulic Studies, 2001).

was delineated by the ERT-P1 geoelectrical section at the right margin of the main valley (Figure 3). These relatively high radon signals may reveal the existence of possible spatial relationship with the underlying permeable geologic medium that is associated with the expected fractured zones. Further, this finding may indicate the possibility of using soil gas radon technique as a useful tool for tracing unknown subsurface faults. In view of the geological environment of the studied dam, the

clay materials tend to fill cracks and fractures by sliding downward through run off surface water. Based on this observation, the soil gas concentration in such environments may sometimes reflect the presence of clay, which is commonly characterized by higher level of natural radioactivity.

Interpretation of the P2 profile

With regard to the ERT-P2 section (Figure 5), it seems to be structural different from the previous ERT-P1 profile because it does not has the same direction locality with respect to the general bedding trends. The most important thing which characterizes the geoelectrical ERT-P2 section is the existence of an abnormal subsurface feature located at the first third of the section. This anomalous feature has a special geometric shape and located at a depth of 10m from the surface with downward extension. The real nature of this structure did not precisely determined and it could be related to compact massive rocks or archeological remains such as road or tunnel. Thus, more geophysical and archeological investigations are needed to confirm the true nature of this anomaly since the dam's lake is located within the geographic zone of the ancient Roman Afamia city and the site is filled by hundreds of buried Roman graves, wells and others subsurface archaeological monuments. The resistivity of the detected anomalous feature is relativity high and reaches more than 1200Ω.m, whereas it very low and does not exceed 20Ω.m for the clayey deposits that surround the outer edges of the feature. The structural discrepancy between the unknown feature and its surroundings may led to the development of an inhomogeneous

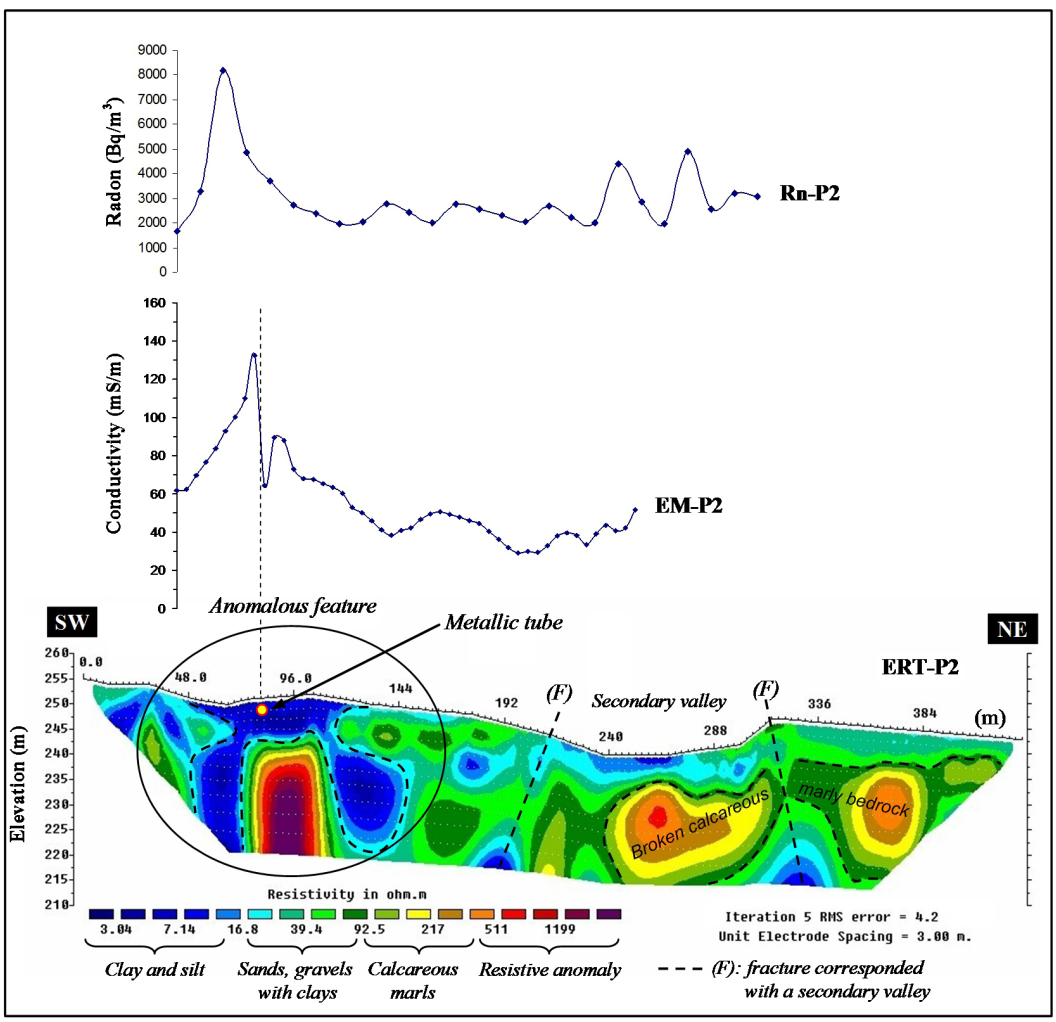

Figure 5. Interpretation of the P2 profile which includes the results of ERT, EM and soil radon measuements carried out in Afamia B dam.

situation and could play a negative role in permitting the water to leak down through the cracks that bounded the anomalous object. As the survey proceeds along the same profile (ERT-P2), another clay deposits were observed between the distances 240 and 300m from the start point of the profile. These deposits are lying through a small depression of branch valley that intersects perpendicularly with the linear course of the main valley in the area. However, the field observations indicate that such upright junction is mostly controlled by local tectonics where small fault segments are probably branching out from the main fault associated with the main valley. Moreover, it is clear that the local tectonic setting has led to the break the impermeable hard marl bed coincided with the secondary valley between the distances 210-310m of the ERT section (Figure 5). This finding may enhance in certain way to the occurrence of vertical leakage processes across the secondary valley.

Concerning the EM-P2 measurements, it has been observed that the electrical conductivity values increased notably above the detected anomalous feature reaching 140mS/m (7Ω.m). The high conductivity values can be attributed to the accumulation of the clay deposits above the aforesaid abnormal feature. The shifting point which is observed on the EM curve at a distance of 80m from starting point of the ERT-P1 section is mostly related to the existence of a buried metallic tube at 2m depth, which is connected to the filling tower for air evacuation uses. As the concerned metallic tube is completely surrounded by clayey deposits, thus it cannot be differentiated clearly by the ERT technique because there is no sufficient contrast in the electrical resistivity, while the EM technique is more sensitive and adequate for detecting buried metallic objects (Bevan, 2013; Dionne *et al*., 2011). On the other hand, a major radon anomaly with a peak value of more than twice higher than the average background level was also recorded at the same locality where the abovementioned subsurface anomalous feature was detected on the ERT-P2 section (Figure5). This anomalous radon observation is probably related to the surrounding environment of the detected object itself, which may provide an additional driving mechanism that could enhance the upward flow of radon gas through the outer boundary openings and fractures. The detected buried feature seemed to be coated by a thin layer of clay which seems to be shifted downwards through bounding fractures and by the flowing water and re-precipitated underneath the surface along the periphery of the object. Such process indicates mostly vertical discontinuity zones which may possibly

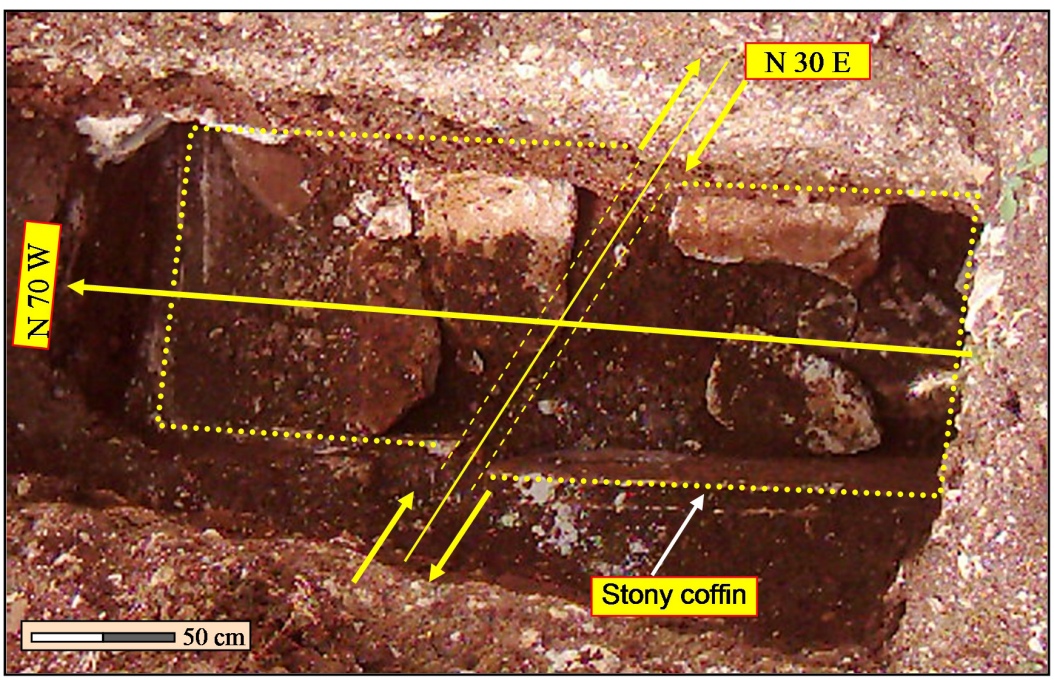

Figure 6. A photo of an archeological grave showing a diagonal fracture in a stony coffin found in the Afamia B dam's lake.

assist the downward leakage of water from the dam's lake. Another two smaller peaks of radon concentration with EM values were observed along the same measuring profile at a distance of 240m and 280m from the start point of ERT section (Figure 5). These two adjoining radon peaks appear to be consistent with the locality of a deformed structure at the margins of the secondary branch, where it intersects with the course of the main valley. Additionally, as it is mentioned above the Afamia dam's lake forms a distinctive archeological site where a hundreds of ruined graves other old vestiges of human activities are distributed throughout the lake. One of the field observations in this study, revealed the discovery of a tomb containing a stony coffin of 3m length and 1.25m width (Figure 6). This coffin is subjected to diagonal fracture in its middle part (N30E), this could be due to either the influence of the dynamic stress of the surrounding clays, or due to the effect of historic seismic activities which are commonly characterizing the region, where it is believed that one of these seisms is considered the responsible for the destruction of the ancient city of Afamia. The archeological occurrences could also play an additional role in increasing the permeability of the bottom of the reservoir through possible hydraulic connections between the surface and the deeper permeable karstified formations.

Finally, depending on the results of the geophysical surveys interpretations and some lithological column of boreholes drilled in Afamia dam, a conceptual model was proposed to describe the probable mechanism of water leakage in the dam (Figure 7). Accordingly, two types of leakages can be identified; the first one is a subhorizontal leakage which occurs basically through the permeable layers of sands and gravels. The subhorizontal leakage afterward follows vertical paths in certain locations especially when it meets fractured zones within the calcareous marly beds. The second type of water losses is a vertical leakage, which basically takes place through the base of the main valley and its margins. The marly bedrock which constitutes the bottom of dam's lake seems to be severely eroded and deformed, and thereby it strongly enhances the vertical water leakage processes, which represents the major component of the leakage in the dam.

Conclusions

The results presented herein demonstrated the usefulness of using a combination of various techniques including electrical tomography (ERT), electromagnetic (EM) and soil radon survey, for characterizing the main causes of water leakage in Afamia B dam. A positive

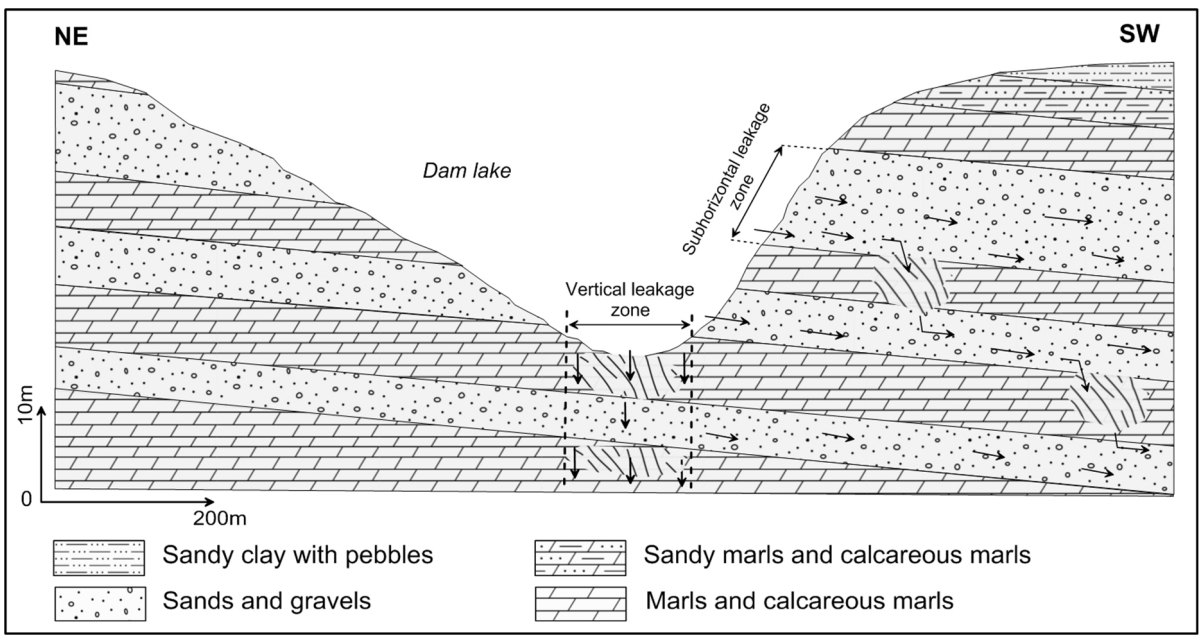

Figure 7. A conceptual model describes the mechanism of the water leakage in Afamia B dam depending on the interpretation of the geophysical and geological data.

correlation has been found between the signals obtained with the application of the three different methods. The interpretation of the ERT-P1 section revealed that the underlying geological structure of the dam basin is mainly consisted of successive lithological beddings of permeable sandy layers alternating with impermeable calcareous marly beds. The difference in permeability properties between the two lithological units is mostly led to a subhorizontal water leakage that occurs through the permeable layers, which form the shoulders of the main valley. This type of leakage is turned out to be a vertical seepage through a pattern of downward trending fractured zones (Figure 7). Moreover, the deformed bedrock and the notable erosion of its surface may play an essential role in developing the processes of vertical leakage through the bottom of the dam lake, especially at the margins of the valley. Such investigated structures could effectively contribute to the water outflow through the concerned dam basin. A notable anomalous subsurface object was detected at the beginning of the ERT- P2 profile, which constitute an additional factor that facilitates water losses close to the dam body. Furthermore, the site of Afamia dam contained numerous archeological ruins such as graves, olds wells and other vestiges human activities, which certainly increase the permeability through the bottom of the reservoir, and thereby enhance the leakage processes from the dam. Finally, the results of this study indicated the successful integrated interpretation of data from geophysical survey (ERT and EM) along with soil gas radon profiles in characterizing buried tectonic structures and delineating various hidden weak zones.

Acknowledgements

The authors gratefully acknowledge Professor I. Othman, Director General of Syrian Atomic Energy Commission (SAEC), for his constant encouragements. Thanks are also due to the staff of the geology department for their support. We gratefully acknowledge the anonymous reviewers for their important comments and suggestions which considerably enhanced the quality of the manuscript.

References

Al-Fares, W., 2011. Contribution of the geophysical methods in characterizing the water leakage in Afamia B dam, Syria. Journal of Applied Geophysics, 75, 464-471.

Al-Fares, W., 2014. Application electrical resistivity tomography technique for characterizing the leakage problem in Abu Baara earth dam, Syria. International Journal of Geophysics, Article ID 368128, 9P, doi:10.1155/2014/368128.

Al-Hilal M. Abdul-Wahed MK., 2016. Tectonic and geologic influences on soil gas radon emission along the western extension of Damascus fault, Syria. Environmental Earth Sciences 75(23):1-11. DOI: 10.1007/s12665-016-6292-z

Al-Hilal M. Aissa M., 2015. Characterizing the natural radiation levels throughout the main geological units of Sabkhat al Jabboul area, northern Syria. J Environ Radioact 140:1–10

Al-Hilal, M. and Al-Ali, A., 2010. The role of soil gas radon survey in exploring unknown subsurface faults at Afamia B Dam, Syria. Radiation Measurements, 45, 219-224.

Anchuela, O. P., Casas Sainz, A. M., Pocovi Juan, A. and Gil Garbi, H., 2015. Assessing karst hazards in urbanized areas. Case study and methodological considerations in the mantle karst from Zaragoza city (NE Spain). Engineering Geology, 184, 29-42.

Baubron, J.C., Rigo, A. and Toutain, J.P., 2002. Soil gas profiles as a tool to characterize active tectonic areas: the Jaut Pass example (Pyrenees, France). Earth Planet Sci. Lett., 196, 69-81.

Bevan, B.W., 2013. Electromagnetics for Mapping Buried Earth Features, Journal of Field Archaeology, 10:1, 47-54.

Brew, G., Barazangi, M., AL-Maleh, K. and Sawaf, T., 2001. Tectonic and Geologic Evolution of Syria. GeoArabia, 6, 3, 573-616.

Candansayar, M.E., 2008. Two-dimensional individual and joint inversion of three and four-electrode array dc resistivity data. Journal of Geophysics and Engineering, 5, 290-300.

Cho, I.K. and Yeom, J.Y., 2007. Crossline resistivity tomography for the delineation of anomalous seepage pathways in an embankment dam. Geophysics, 72, 31-38.

Claudia Schütze, Thomas Vienken, Ulrike Werban, Peter Dietrich, Anthony Finizola, Carsten Leven, 2016. Joint application of geophysical methods and Direct Push-soil gas surveys for the improved delineation of buried fault zones. Journal of Applied Geophysics, Elsevier, 2012, 82, pp.129-136

Ciotoli, G., G. Etiope, M. Guerra, and S. Lombardi, (1999) The detection of concealed faults in the Ofanto Basin using the correlation between soil-gas fracture surveys, *Tectonophysics*, 301, 321–332, 1999.

Cygal A., Stefaniuk M., Kret A., Kurowska M., 2016. The application of electrical resistivity tomography (ERT), induced polarization (IP) and electromagnetic conductivity (EMC) methods for the evaluation of technical condition of flood embankment corpus. Geology, Geophysics and Environment, 42, 279–287.

Dahlin, T., Zhou, B., 2004. A numerical comparison of 2-D resistivity imaging with 10 electrode arrays. Geophysical Prospecting, 52, 379-398.

Demanet, D., Pirard, E., Renardy, F. and Jongmans, D., 2001. Application and processing of geophysical images for mapping faults. Computers & Geosciences, 27,1031-1037.

Dionne, C., Schultz, J., Murdock, R., Smith, S., 2011. Detecting Buried Metallic Weapons in A Controlled Setting using a Conductivity Meter. Forensic Science International, 208, 18-24.

Farzamian, M., Monteiro, Santos, F.A. and Khalil, M. A., 2015. Application of EM 38 and ERT methods in estimation of saturated hydraulic conductivity in unsaturated soil. Journal of Applied Geophysics, 112,175-18.

Fu, C.C, Yang, T.F, Walia, V. and Chen, C.H., 2005. Reconnaissance of soil gas composition over the buried fault and fracture zone in southern Taiwan. Geochemical Journal, 39, 427-439.

General Company of Hydraulic Studies in Syria 2001. Technical geological report about the detailed investigations in Afamia C and B dams, internal report, 47p.

Guerin, R., Begassat, P., Benderitter, Y., David, J., Tabbagh, A. and Thiry, M., 2004. Geophysical study of the industrial waste land in Mortagnedu-Nord (France) using electrical resistivity. Near Surface Geophysics, 2, 137-143.

Gutierrez, F., Mozafari, M., Carbonel, D., Gómez, R. and Raeisi, E., 2015. Leakage problems in dams built on evaporites. The case of La Loteta Dam (NE Spain), a reservoir in a large karstic depression generated by interstratal salt dissolution. Engineering Geology, 185,139–154.

Joos, B., Bussard, Th., 2004. Report about treatment of seepage at Afamia Dams prepared by STUCKY Consulting Engineers Ltd. The General Company of Hydraulic Studies, Homs, Syria.

Khaki, M., Yusoff I. and Islami, N., 2014. Electrical resistivity imaging and hydrochemical analysis for groundwater investigation in Kuala Langat, Malaysia. Hydrological Sciences Journal, DOI:10.1080/02626667.2014.950578.

King, C.Y., King, B.S. and Evans, W.C., 1996. Spatial radon anomalies on active faults in California Appl. Geochem., 11, 497-510.

Lin, C.P., Hung, Y.C., Yu, Z.H., and Wu, P.L., 2013. Investigation of abnormal seepages in an earth dam using resistivity tomography. Journal of GeoEngineering, 8, 61-70.

Loke, M.H., Barker, R.D., 1996. Rapid least-square inversion of apparent resistivity pseudo-section by a quasi-Newton method. Geophysical Prospecting, 44, 131-152.

McNeill, J.D., 1990. Use of electromagnetic methods for groundwater studies. In: Ward, S.H. (Ed.), Geotechnical and Environmental Geophysics. Society of Exploration Geophysicists, USA. No. 5, 191-218.

Minasian, R., 2010. Technical report about the results of geophysical studies in Afamia Dams B&C. Hydroscope Scientific Productional Company Ltd, Republic of Armenia, in cooperation with the General Company of Hydraulic Studies in Syria. Contract No. 19/D/2001, unpublished internal report.

Nguyen, F., Garambois, S., Chardon, D., Hermitte, D., Bellier, O. and Jongmans, D., 2007. Subsurface electrical imaging of anisotropic formations slow active reverse fault, Provence, France. Journal of Applied Geophysics, 62, 338-353.

Novo, A., Vincent, M. L. and Levy, T. E., 2012. Geophysical surveys at Khirbat Faynan, an ancient mound site in southern Jordan,☐ International Journal of Geophysics, Article ID 432823, 8 pages. doi:10.1155/2012/432823.

Osinowo, O., Falufosi, M., Omiyale, E., 2018. Integrated electromagnetic (EM) and Electrical Resistivity Tomography (ERT) geophysical studies of environmental impact

of Awotan dumpsite in Ibadan, southwestern Nigeria. Journal of African Earth Sciences, 140, 42-51.

Panthulu, T.V., Krishnaiah, C. and Shirke, J.M., 2001. Detection of seepage paths in earth dams using self-potential and electrical resistivity methods. Engineering Geology, 59, 281-295.

Paula, G., Hammack, R., Harbert, W., Sams, J., Veloski, G. and Ackman, T., 2004. Delineating the subsurface: using surface geophysics to identify groundwater flow paths in a carbonate aquifer. Journal of Environmental Hydrology, 12, 1-10. Perez-Gracia, V., Caselles, J.O., Clapes, J., Osorio, R., Martinez, G. and Canas, J.A., 2009. Integrated near-surface geophysical survey of the Cathedral of Mallorca. Journal of Archaeological Science, 36,1289-1299.

Pham, V.N., Boyer, D., Le Mouël, J.L. and Nguyen, T.K.T., 2002. Hydrogeological investigation in the Mekong Delta around Ho-Chi-Minh City (South Vietnam) by electric tomography. C. R. Geoscience, 334, 733-740.

Ponikarov, V., 1966. The geology of Syria, Explanatory Notes on the Geological Map of Syria, Hama sheet, Scale 1:1200,000, V.O. Technoexport. Minestry of Industry, Damascus, Syria.

Sjodahl, P., Dahlin, T. and Johansson, S., 2010. Using the resistivity method for leakage detection in a blind test at the Rossvatn embankment dam test facility in Norway. Bull. Eng. Geol. Environ., 69, 643-658.

Soupios, P., Papadopoulos, N., Papadopoulos, I., Kouli, M., Vallianatos, F., Sarris, A., Manios, T., 2007. Application of integrated methods in mapping waste disposal areas. Environmental Geology, 53: 661. https://doi.org/10.1007/s00254-007-0681-2.

Swakon, J., Kozak, K., Paszkowski, M., Gradzinski, R., Janik, M. and Horwacik, T., 2005. Radon concentration in soil gas around local disjunctive tectonic zones in the Krakow area. Journal of Environmental Radioactivity, 78, 137-149.

Szalai, S., Koppán, A., Szokoli, K., Szarka, L., 2013. Geoelectric imaging properties of traditional arrays and of the optimized Stummer configuration. Near Surface Geophysics, 11, 51-62.

Torres-Rondon, L., Carriere, S. D., Chalikakis, K. and Valles, V., 2013. An integrative geological and geophysical approach to characterize a superficial deltaic aquifer in the Camargue plain, France. C. R. Geosciences, l, 241-250.

Van Schoor, M., 2002. Detection of sinkhole using 2D electrical resistivity imaging. Journal of Applied Geophysics, 50, 393-399.

Wilkinson, P., Meldrum, P., Chambers, J., Kuras, O., Ogilvy, R., 2006. Improved strategies for the automatic selection of optimized sets of electrical resistivity tomography measurement configurations. Geophysical Journal International, 167,1119-1126.

Zarroca, M., Linares, R., Bach, J., Roqué, C., Moreno, V., Font, Ll., Baixeras, C., 2012. Integrated geophysics and soil gas profiles as a tool to characterize active faults: the Amer fault example (Pyrenees, NE Spain). Environmental Earth Sciences, 67, 889–910.

Geofísica Internacional (2018) 57-4: 289-306

Original paper

Caracterización de asperezas de sismos recientes en la zona de subducción de Michoacán-Colima-Jalisco, México

M.R. Martínez López and C. Mendoza

Received: April 25, 2018; accepted: September 07, 2018; published on line: October 3, 2018

Resumen

Se determinaron de manera sistemática los modelos de deslizamiento de los sismos de magnitud Mw mayor a 7 ocurridos desde el año 1980 en la zona de subducción de Michoacán-Colima-Jalisco utilizando ondas P y SH registradas a distancias telesísmicas y una parametrización que permite una amplia flexibilidad en la duración de la dislocación sobre el plano de falla. Para los distintos eventos las áreas de valores altos de deslizamiento no se empalman y forman un patrón entrelazado de asperezas adyacentes con espacios entre ellas que podrían identificar zonas de mayor deslizamiento en sismos futuros. El análisis sistemático de los sismos permitió investigar las incertidumbres de las asperezas. Estas incertidumbres se determinaron utilizando un simple procedimiento de muestreo donde se realizaron 300 inversiones independientes para cada evento tomando en cuenta posibles errores en la geometría de la falla, la profundidad del hipocentro y la velocidad de ruptura. Las dimensiones de las asperezas parecen mantenerse dentro de un mismo rango, lo que implicaría la existencia de asperezas relativamente homogéneas en esta porción del contacto interplaca. Las duraciones de dislocación de las asperezas estan bien restringidas y se escalan con el tamaño del evento. Para eventos Mw ~7.5 las duraciones son de ~5s y para sismos de Mw 8.0 los valores son de ~12s. Las caídas de esfuerzo calculadas para las asperezas son menores a 2.0 MPa, consistente con valores estimados para sismos de subducción en general. Los resultados indican que el muestreo de los parámetros de entrada ofrece una alternativa para evaluar las propiedades e incertidumbres de las asperezas en zonas de subducción. Además los resultados tienen implicaciones importantes para la evaluación del potencial sísmico y para el desarrollo de leyes de escalamiento.

Palabras clave: modelos de deslizamiento, asperezas, incertidumbres.

Abstract

Slip models of earthquakes of magnitude Mw greater than 7 occurring since 1980 in the Michoacán-Colima-Jalisco subduction zone were determined using P and SH waves recorded at teleseismic distances and a fault parameterization that allows a wide flexibility in rise time. The high slip areas of the different events do not overlap, forming an interlocking pattern of adjacent asperities separated by regions that could identify areas of major slip in future earthquakes. The systematic analysis of the earthquakes allowed an investigation of the uncertainties in the asperity properties. These uncertainties were determined using a simple sampling procedure where 300 independent inversions were run for each event taking into account possible errors in fault geometry, hypocenter depth and rupture velocity. The dimensions and maximum slip of the asperities appear to lie within the same range, which would imply the existence of relatively homogenous asperities in this portion of the plate interface. The rise times of the asperities are well constrained and scale with the size of the event. For Mw ~7.5 events the durations are ~5s and for earthquakes of Mw 8.0 the rise times are ~12s. The stress drops calculated for the asperities are less than 2.0 MPa, consistent with values estimated for subduction earthquakes in general. The results indicate that the parameter-sampling procedure offers an alternative for identifying the properties and uncertainties of asperities in subduction regions. Also, the results have important implications for the evaluation of the seismic potential and the development of earthquake scaling laws.

Key words: slip models, asperities, uncertainties.

M.R. Martínez López[1]
Posgrado en Ciencias de la Tierra
Universidad Nacional Autónoma de México
Campus Juriquilla, Querétaro
México

C. Mendoza
Centro de Geociencias
Universidad Nacional Autónoma de México
Campus Juriquilla, Querétaro
México
Corresponding author:

Introducción

El contacto interplaca en las zonas de subducción constituye una de las principales fuentes de peligro sísmico en el mundo debido que en estas regiones se generan los sismos de mayor magnitud. En este contacto se producen grandes esfuerzos que se acumulan a lo largo del tiempo y eventualmente se liberan durante sismos mayores. Se piensa que estos esfuerzos se acumulan en áreas de alta fricción, llamadas asperezas, en la zona de contacto y eventualmente se liberan (Kanamori, 1978; Lay y Kanamori, 1981) irradiando la energía principal de las ondas sísmicas registradas en el campo lejano. En conjunto, las asperezas y las zonas débiles que las rodean representan el área de ruptura total (Kanamori, 1981, Lay *et al*., 1982) que excita las ondas sísmicas de más largo período y define el momento sísmico del evento.

México se encuentra en una región de gran deformación tectónica debido a la interacción de las placas de Rivera, Cocos y Norteamérica. Esta área incluye la región de Michoacán-Colima-Jalisco donde varios terremotos destructivos han ocurrido en el último siglo. La Figura 1 muestra los sismos de magnitud Mw mayor a 7 que han ocurrido en la región desde el año 1900, basado en los momentos sísmicos calculados para los eventos (Tabla 1). Estos sismos generalmente resultan de fallas inversas en el contacto interplaca y han causado daños significativos tanto tierra adentro como cerca de la costa. Los eventos incluyen el terremoto de Mw 8.1 de Jalisco del 3 de junio de 1932, el sismo interplaca más grande registrado instrumentalmente hasta la fecha en la zona de subducción de México. Singh *et al*. (1985) estimaron una longitud de ruptura de 220 km para el evento basado en la distribución de réplicas. El sismo Mw 8.1 del 19 de septiembre de 1985 que resultó en daños y pérdidas sin precedentes en la Ciudad de México (Esteva, 1988) también ocurrió en esta región. Recientemente, el evento del 9 de octubre de 1995 (Mw 8.0) generó daños importantes cerca al área epicentral en Manzanillo, Colima y en el noroeste del estado de Jalisco (Juárez-García *et al*., 1997).

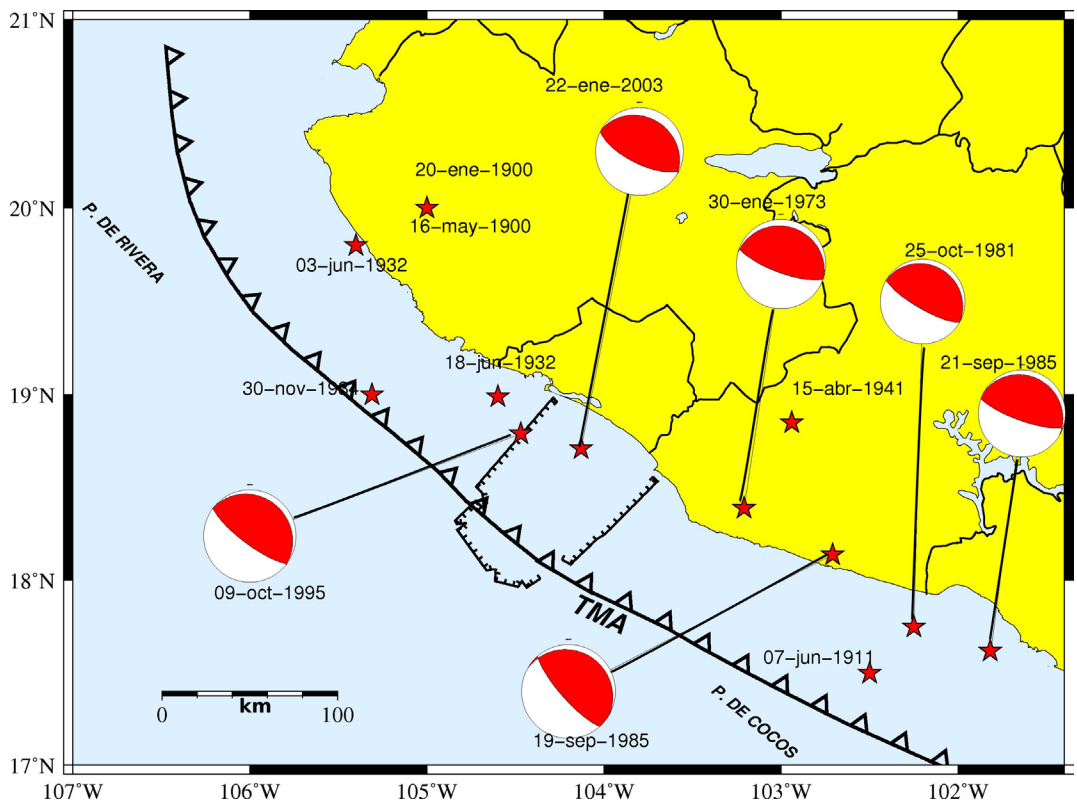

Figura 1. Sismos mayores a Mw 7 (estrellas) que han ocurrido en la zona de subducción de Michoacán-Colima-Jalisco desde 1900 entre las longitudes de -101.5º a -107.00º. Se muestran los mecanismos focales reportados por el Global Centroid Moment Tensor (www.globalcmt.org) para eventos ocurridos de 1973 a 2003. TMA es la trinchera mesoamericana.

Tabla 1. Sismos inversos Mw > 7 ocurridos en la zona de subducción de Michoacan-Colima-Jalisco, México (-101.5° a -107°, longitud) desde 1900.

Fecha	Lat (º)+	Lon (º)	Mw++
20-ene-1900	20.00	-105.00	7.4
16-may-1900	20.00	-105.00	7.0
07-jun-1911	17.50	-102.50	7.6
03-jun-1932	19.80	-105.40	8.1
18-jun-1932	18.99	-103.50	7.9
30-nov-1934	19.00	-105.31	7.1
15-abr-1941	18.85	-102.94	7.6
30-ene-1973	18.39	-103.211	7.6
25-oct-1981	17.75	-102.252	7.2
19-sep-1985	18.14	-102.713	8.1
21-sep-1985	17.62	-101.823	7.5
9-oct-1995	18.79	-104.474	8.0
22-ene-2003	18.71	-104.135	7.5

+ Los epicentros de eventos ocurridos antes de 1970 se tomaron de Santoyo et al. (2005).
Para eventos posteriores las referencias son: 1 Lomnitz, 1977; 2 Havskov et al., 1983; 3 UNAM Seismology Group, 1986; 4 Courboulex et al., 1997; 5 Yagi et al., 2004.

++ Magnitud Mw calculada del momento sísmico tomado de Anderson et al. (1989) y Pacheco y Sykes (1992) para eventos anteriores a 1990.
Para eventos posteriores la magnitud Mw es del gCMT (www.globalcmt.org).

Se han publicado modelos de deslizamiento para varios de los sismos Mw > 7 ocurridos en la zona de subducción de Michoacán-Colima-Jalisco utilizando registros sísmicos (p. ej. Mendoza y Hartzell, 1988; 1989; Mendoza, 1993; Mendoza, 1995; Courboulex *et al*., 1997; Mendoza y Hartzell, 1999; Yagi *et al*., 2004; Santoyo *et al*. 2005; Mendoza *et al*., 2012; UNAM Seismology Group, 1986; 2015; Mendoza y Martínez-López, 2017). Estos modelos delinean la ruptura del terremoto e identifican áreas de concentración de deslizamiento que se han interpretado como asperezas en el contacto interplaca. Sin embargo, los estudios han utilizado metodologías con diferentes tipos de datos, incluyendo registros telesísmicos y en algunos casos, estaciones locales o regionales. Además, los parámetros utilizados para definir las fallas no han sido siempre consistentes entre sí. Los estudios más antiguos, por ejemplo, no han permitido suficiente flexibilidad en el tiempo que tarda el deslizamiento en llegar al valor final (duración de la dislocación), debido principalmente a la capacidad computacional disponible en el momento. Estos diferentes enfoques dificultan una comparación adecuada entre eventos y una evaluación apropiada del comportamiento de las asperezas.

Los sismos mayores a Mw 7 ocurridos desde el año 1980 en la zona de subducción de Michoacán Colima Jalisco han sido registrados a distancias telesísmicas por instrumentos digitales que proporcionan formas de onda de cuerpo de alta calidad que se pueden examinar para identificar las propiedades de la fuente sísmica. Estos registros digitales se han utilizado en algunos casos para la distribución del deslizamiento cosísmico. En este trabajo proponemos analizar estos datos globales para determinar de manera uniforme la historia de ruptura de cinco sismos recientes mayores a Mw 7 que han ocurrido en la zona de subducción de Michoacán-Colima-Jalisco desde el año 1980. Estos incluyen los sismos de Playa Azul del 25 de octubre de 1981 (Mw 7.2), de Michoacán del 19 de septiembre de 1985 (Mw 8.1), de Zihuatanejo del 21 de septiembre de 1985 (Mw 7.5), de Colima-Jalisco del 9 de octubre de 1995 (Mw 8.0), y de Tecomán del 22 de enero de 2003 (Mw 7.5). Se aplica el mismo método de inversión de la fuente utilizando parámetros similares de la falla con el fin de comparar distribuciones similares del deslizamiento cosísmico para los distintos eventos. Utilizamos el esquema de inversión de falla finita de Hartzell y Heaton (1983; 1986), modificado por Mendoza

y Hartzell (2013) para identificar directamente el nivel de estabilización y obtener la solución en un solo paso. Recientemente, Mendoza y Martínez-López (2017) aplicaron esta misma metodología a las ondas P y SH registradas a distancias telesísmicas para el sismo Mw 7.3 del 18 de abril 2014 en Papanoa, Guerrero.

La determinación consistente de los modelos telesísmicos nos permite además examinar las posibles incertidumbres debidas al conocimiento incompleto de los parámetros que se utilizan para definir la falla. Variaciones en estos parámetros afectan los resultados obtenidos (Hartzell, 1989; Hartzell y Langer, 1993; Beresnev, 2003; Lay *et al*., 2010). Por ejemplo, Hartzell y Langer (1993) sugieren que se pueden generar resultados erróneos si se utiliza una parametrización de la falla que no permita suficiente variación espacial en la amplitud de deslizamiento, en la duración de la dislocación y en el tiempo de inicio de la ruptura. Errores en la geometría de la falla que se utiliza para modelar la ruptura también contribuyen a la incertidumbre del modelo de deslizamiento determinado. En un estudio telesísmico de los eventos del 9 de octubre 1995 (Mw 8.0) y del 22 de enero 2003 (Mw 7.5), Mendoza *et al*. (2012) observaron que los errores en el buzamiento y la profundidad de nucleación afectan más la precisión de la fuente inferida que los errores que se tienen en el rumbo y en el ángulo de deslizamiento. Por otra parte, Hartzell *et al*. (2013) invirtieron formas de ondas registradas a distancias telesísmicas y regionales para obtener distintos modelos de deslizamiento para el evento Mw 5.8 de 2011 occurrido en Mineral, Virginia, EUA. Ellos aplicaron a cada solución un procedimiento simple donde variaron el alineamiento entre datos observados y teóricos de manera sistematica asumiendo una distribución Gaussiana que les permitió calcular la variabilidad del deslizamiento. Mencionan que esta manera de abordar la variabilidad de los errores podría ser útil en el análisis de las incertidumbres variando otros parámetros del modelo (Hartzell *et al*., 2013). En este trabajo adoptamos este procedimiento para examinar la incertidumbre en los modelos telesísmicos de deslizamiento de sismos recientes en Michocán-Colima-Jalisco debido a posibles errores en los parámetros de la falla. En nuestro caso, variamos el rumbo, el buzamiento, el ángulo de deslizamiento, la profundidad del hipocentro y la velocidad de ruptura utilizando una distribución uniforme de los parámetros. Los resultados de la redeterminación de patrones de ruptura y sus posibles incertidumbres permiten una evaluación de la ubicación e interacción entre asperezas en esta sección de la zona de subducción de México. Además aportan información consistente de las rupturas sísmicas recientes en esta zona que podrían ser de utilidad en la definición de leyes de escalamiento.

Datos

Para determinar los modelos de deslizamiento se invirtieron las ondas de cuerpo telesísmicas registradas en las estaciones digitales mundiales disponibles del Incorporated Research Institutions for Seismology (IRIS, http://www.iris.edu/). Utilizamos las ondas P registradas entre 25 y 95 grados y las ondas SH registradas entre 35 y 80 grados para minimizar los efectos de difracción del núcleo, la propagación en el manto superior y las triplicaciones del manto. Las ondas P se obtuvieron a partir de los registros verticales, y las ondas SH se recuperaron mediante la rotación de los componentes horizontales, corrigiendo los registros P y SH por la respuesta instrumental para obtener observaciones en desplazamiento. Utilizamos el ancho de banda más amplio posible para las observaciones. Para eventos ocurridos después del año 1990 estos corresponden a datos de banda ancha registrados por la Red Sísmica Global (GSN, por sus siglas en ingles). Antes de 1990, las estaciones digitales registraban señales en varias bandas de frecuencias para producir componentes de período largo, período intermedio y período corto. Para esos eventos se utilizaron los registros de periodo largo e intermedio. Sin embargo, había muy pocas estaciones de registro intermedio al inicio de la decada de los ochenta y se consideraron además registros de periodo corto para el sismo de Playa Azul de 1981. Para los registros de banda ancha y de periodo intermedio, aplicamos un filtro pasa banda en un intervalo de periodo entre 1- 60s y remuestreamos las formas de onda a 0.25s. Los registros de período largo se filtraron entre 10-80s y se remuestrearon a 1s. Los registros de periodo corto registrados para el sismo de Playa Azul de 1981 se filtraron entre 1-5s y se remuestrearon a 0.1s.

Metodología

Se aplicó la metodología de falla finita originalmente desarrollada por Hartzell y Heaton (1983) que se ha utilizado en el estudio de sismos mayores en la zona de subducción de la costa del Pacífico Mexicano (p. ej. Mendoza y Hartzell, 1988; 1989; Mendoza, 1993; Mendoza, 1995; Mendoza y Hartzell, 1999; Mendoza y Martinez-Lopez, 2017). La metodología se basa en una parametrización cinemática de la falla para identificar la distribución del deslizamiento cosísmico que mejor reproduce las formas de onda registradas. En la aplicación del método se identifica un plano de falla

con orientación y geometría basadas en el mecanismo focal del sismo. Se subdivide la falla en un número específico de celdas y se fija la ubicación del hipocentro. Posteriormente, se calculan los sismogramas sintéticos para cada celda asumiendo que cada una de estas está compuesta de fuentes puntuales distribuidas uniformemente a lo largo y ancho de sus dimensiones. Se asume que cada una de las fuentes puntuales se dispara cuando el frente de ruptura, que viaja a una velocidad constante a lo largo de la falla desde el hipocentro, llega a ese punto. Las respuestas para cada fuente puntual (funciones de Green) se calculan utilizando una función rectangular (boxcar) de duración fija usando un modelo de corteza basado en los resultados obtenidos por Stolte *et al*. (1986) para la región de Michoacán-Guerrero. Las funciones de Green se retardadan por el tiempo de ruptura y se suman para obtener el sismograma sintético de cada celda.

El problema numérico de inversión es completamente lineal y se construye poniendo los sismogramas generados para cada celda de todas las estaciónes una tras otra para formar las columnas de una matriz **A** de amplitudes sintéticas. El número de columnas entonces corresponde al número de celdas que se consideran en la inversión. Las formas de onda observadas en todas las estaciones similarmente se juntan una tras otra para formar un vector de datos **b**. Los detalles de la construcción de esta matriz y el vector de datos se puede consultar en el trabajo de Hartzell y Heaton (1983). Los datos y los sintéticos forman un sistema sobredeterminado de ecuaciones lineales $C_d^{-1}\mathbf{Ax}=C_d^{-1}\mathbf{b}$ donde C_d^{-1} es una matriz de covarianza de datos que normaliza cada registro de estación a su amplitud máxima. El vector solución **x** contiene los deslizamientos requeridos en cada celda para reproducir las observaciones. Para permitir flexibilidad en el tiempo de inicio de ruptura en cada celda, se añaden columnas adicionales a la matriz de coeficientes $C_d^{-1}\mathbf{A}$ donde los sintéticos normalizados de cada celda se retrasan por el ancho de la función rectangular que se utilizó para generar las funciones de Green. El número de veces que los sintéticos de cada celda se retrasan y se añaden a la matriz de coeficientes corresponde al número de ventanas de tiempo utilizadas para discretizar la duración de la dislocación sobre la falla. La inversión recupera el deslizamiento en cada celda para cada una de estas ventanas de tiempo. Típicamente el deslizamiento mayor se observa en las ventanas iniciales y a partir de cierto tiempo no hay más contribuciones al deslizamiento. Este tiempo define la duración de dislocación requerida por las observaciones.

El problema inverso se estabiliza mediante la adición de ecuaciones de restricción de la forma $\lambda\mathbf{Fx}= 0$ al sistema lineal

$$\begin{bmatrix} C_d{}^{1}A \\ \lambda F_1 \\ \lambda F_2 \end{bmatrix} \mathrm{x} = \begin{bmatrix} \mathrm{C}_d{}^{-1}b \\ 0 \\ 0 \end{bmatrix}$$

donde F_1 representa la diferencia de deslizamiento entre celdas adyacentes, y F_2 es la matriz identidad. La primera restricción impone una transición suave de deslizamiento entre celdas, y la segunda restricción reduce la longitud del vector de solución **x**, minimizando el momento sísmico total. El parámetro λ controla el compromiso entre aplicar las restricciones y ajustar las observaciones y se estima usando la relación $\lambda=90|\mathbf{a}|_{avg}$ sugerida por Mendoza y Hartzell (2013), donde $|\mathbf{a}|_{avg}$ es la media de los valores absolutos de los elementos de la matriz normalizada de coeficientes $C_d^{-1}\mathbf{A}$. Esta relación se obtuvo a partir de una revisión de la variación de los valores de suavizamiento de varios sismos mayor a Mw 6 con modelos de deslizamiento determinados utilizando ondas P telesísmicas (Mendoza y Hartzell, 2013).

Los modelos de deslizamiento obtenidos en este estudio se determinaron tomando el plano nodal con buzamiento noreste del mecanismo focal reportado por el gCMT Project (http://www.globalcmt.org). Se utilizó el epicentro mejor conocido para cada evento obtenido de estudios previos (Tabla 1). Para los eventos con magnitud Mw entre 7.2 y 7.5 se utilizaron 10 ventanas de tiempo con longitudes de 1 s cada una, permitiendo una dislocación máxima de 10s. Para los eventos con magnitudes Mw 8.0 se utilizaron 10 ventanas de tiempo con una longitud de 2s, permitiendo dislocaciones máximas de 20s. Las dimensiones de las celdas son de 5x5 km y de 10x10 km para sismos de Mw ~7 y de Mw 8, respectivamente. Se limito la profundidad máxima de la falla a 40 km para los eventos Mw 8.0 considerando el límite inferior de la zona de acoplamiento sismogénico determinado por Martínez-López y Mendoza (2015) para la región de Michoacán-Colima-Jalisco.

Para estimar las incertidumbres debido a posibles errores en los parámetros de entrada se aplicó un procedimiento similar al proceso de muestreo que utilizaron Hartzell *et al*. (2013) para analizar el sismo de 2011 en Virginia, EUA. En nuestro caso consideramos errores aleatorios en la geometría de la falla, la profundidad del hipocentro y la velocidad de ruptura. Los valores se varian en un rango de

±5° en el rumbo, ±5° en el buzamiento, ±5° en el ángulo de deslizamiento, ±4 km en la profundidad del hipocentro, y ±0.5 km/s en la velocidad de ruptura y distribuidos de manera uniforme con respecto a los valores de entrada. Para los eventos analizados se observó que tanto los residuales numéricos como los ajustes a los sismogramas son similares para modelos determinados con parámetros de entrada en estos rangos, por lo que consideramos que los rangos representan el mínimo error para cada uno de los parámetros. Se hicieron 300 inversiones independientes para cada evento utilizando las diferentes combinaciones de los parámetros de entrada. Los 300 modelos de deslizamiento obtenidos a partir de este proceso se utilizaron para calcular la desviación estándar del deslizamiento en cada celda.

Modelos de Deslizamiento

Sismo del 25 de octubre de 1981 (Mw 7.2)

Para el sismo de Playa Azul del 25 de octubre de 1981, Mendoza (1993) obtuvo un modelo de deslizamiento utilizando ondas P telesísmicas con una sola ventana de tiempo de 1s. En este estudio incrementamos el número de ventanas a 10 para permitir flexibilidad en la duración de la dislocación sobre el plano de falla. Utilizamos un conjunto de estaciones similar al que utilizó Mendoza (1993), incluyendo además 4 registros de periodo corto y una forma de onda SH. Se invirtieron registros de 65s en longitud disminuyendo la amplitud exponencialmente a los 20s, 35s, y 40s después del inicio de los registros de período corto, período intermedio y período largo, respectivamente, para minimizar los efectos de propagación no relacionados a la fuente. Se utilizó una falla de 80 km por 80 km dividida en 256 celdas de 5 km x 5 km con un rumbo de 287**°**, un buzamiento de 20**°** y un ángulo de deslizamiento de 82**°**. El hipocentro se coloca en el centro de la falla y se utiliza una velocidad de ruptura de 2.6 km/s para calcular los sismogramas sintéticos de cada celda.

Se analizaron varias profundidades hipocentrales tomadas entre los rangos de profundidad reportados por diferentes autores. Estas pruebas indican que una profundidad de 17.5 km es la que mejor ajusta los datos observados. La Figura 2a muestra la distribución de deslizamiento cosísmico obtenida para el evento y la Figura 2b muestra los ajustes de registros para un momento sísmico total de $7.6x10^{19}$ Nm (Mw 7.2). En la zona de ruptura se puede observar una región de alto deslizamiento definida por valores mayores a 45% del pico de 132 cm. Esta zona de alto deslizamiento (A) tiene un deslizamiento promedio de 91 cm y un área de 1050 km². Si consideramos esta área equivalente a un área circular podemos calcular la caída de esfuerzo (**Δσ)** utilizando la relación **Δ**σ= (7/16)Mo/r^3 desarrollada por Eshelby (1957), donde **Mo** es el momento sísmico del área en dinas-cm y **r** es su radio en cm. Esto nos da un valor **Δ**σ de 0.3 MPa. Además, se puede identificar una duración de dislocación de 6s para esta misma zona tomando el promedio de los valores obtenidos para cada celda que se encuentra dentro del polígono de la Figura 2a. La Figura 2c muestra la desviación estándar del deslizamiento observado en cada celda a partir de las 300 inversiones. La mayor incertidumbre (30-40 cm) se observa cerca del hipocentro, donde los valores de deslizamiento en el modelo cosísmico son altos.

Sismo del 19 de septiembre de 1985 (Mw 8.1)

Mendoza y Hartzell (1988;1989) obtuvieron un modelo de deslizamiento del evento de Michoacán del 19 de septiembre de 1985 a partir de una inversión conjunta de datos locales y formas de onda P telesísmicas donde permitieron una duración máxima de dislocación de 6s. En este trabajo se redeterminó el modelo de deslizamiento utilizando 10 ventanas de tiempo de 2s cada una, permitiendo así un intervalo máximo de dislocación de 20s. Se invirtieron 12 formas de onda P de período intermedio y período largo, y 3 formas de onda SH de período intermedio. Se utilizó una longitud de registro de 120s con una disminución exponencial de amplitud después de 60s y 70s para las ondas P y SH, respectivamente. Se utilizó un plano de falla con rumbo de 301°, buzamiento de 18°, y ángulo de deslizamiento de 105°. La falla tiene una longitud de 220 km y un ancho de 120 km, dividida en 264 celdas de 10 km x 10 km. La velocidad de ruptura es de 2.6 km/s.

La profundidad hipocentral que mejor ajusta los datos observados es de 18 km. En la Figura 3a se muestra el modelo de deslizamiento para esta profundidad. Se observan dos fuentes principales separadas por aproximadamente 30 km, una con un deslizamiento máximo de ~550 cm cerca al hipocentro, y otra al sureste con un deslizamiento máximo de ~300 cm. La zona **A** de alto deslizamiento que se localiza cerca del hipocentro tiene un deslizamiento promedio de 356 cm, un área de 1200 km² y una caída de esfuerzo de 0.95 MPa. En la zona **B** de alto deslizamiento al sureste del hipocentro el deslizamiento promedio es 277 cm sobre un área de 900 km² con una caída de esfuerzo de 0.85 MPa. La duración de dislocación en ambas zonas de máximo deslizamiento es 12s. En la Figura 3b se muestran los ajustes de los registros para un momento sísmico total de 9.8×10^{20} Nm

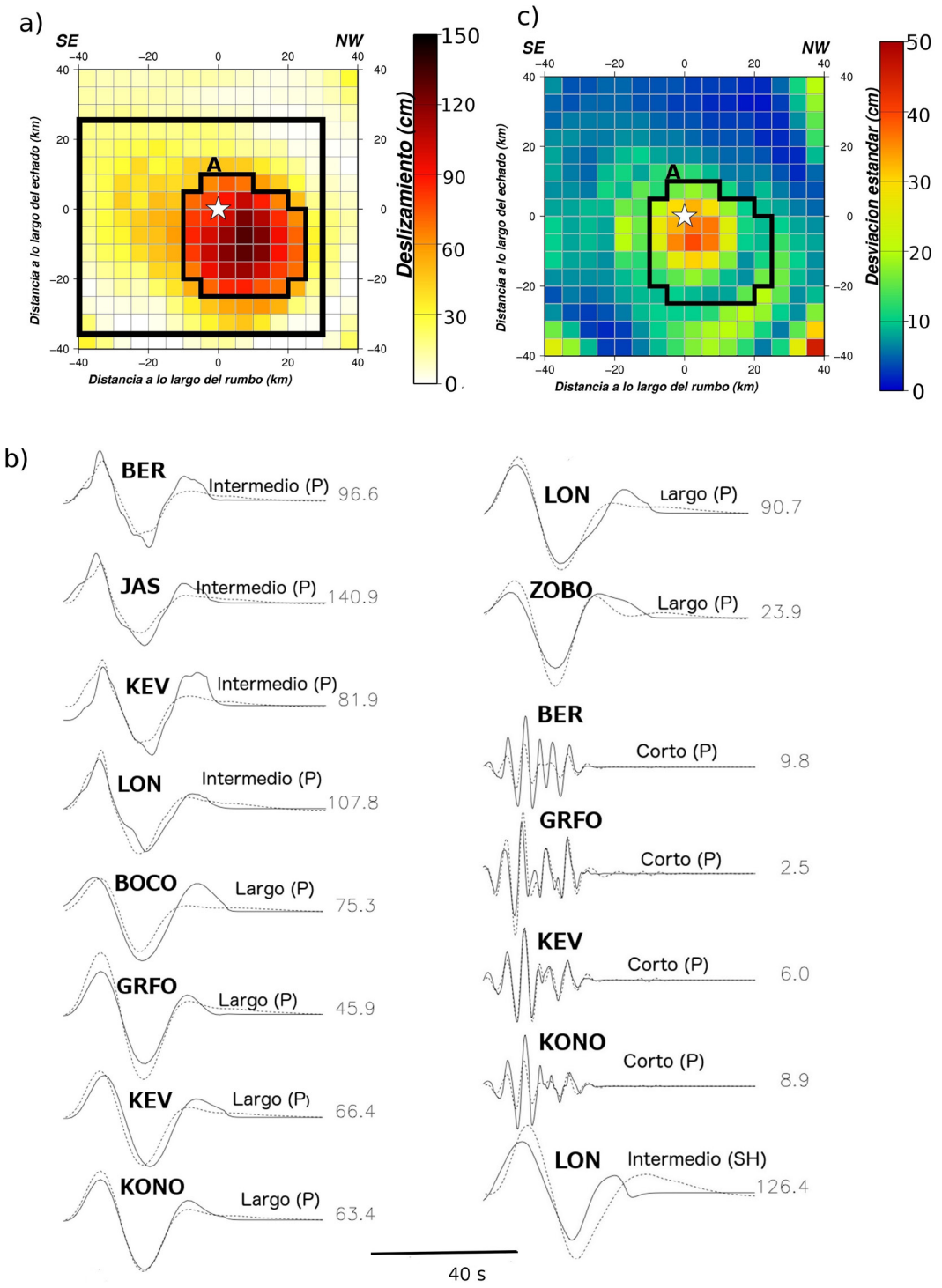

Figura 2. a) Modelo de deslizamiento obtenido para el evento del 25 de octubre de 1981 a partir de la inversión de datos telesísmicos de ondas P y SH. El rectángulo corresponde a la zona de ruptura definida con el procedimiento de Somerville *et al*. (1999). El polígono incluye las celdas con valores mayores al 45% del deslizamiento máximo y la estrella representa el hipocentro. b) Ajustes entre datos observados (línea continua) y teóricos (línea discontinua) para un momento sísmico de 7.6 x 10^{19} Nm (Mw 7.2). Los numeros a la derecha de cada estación corresponden al pico de amplitud (en micrones) del registro observado. c) Desviación estandar del deslizamiento estimado para celda después de 300 inversiones independientes variando el rumbo, buzamiento, ángulo de deslizamiento, profundidad y velocidad de ruptura.

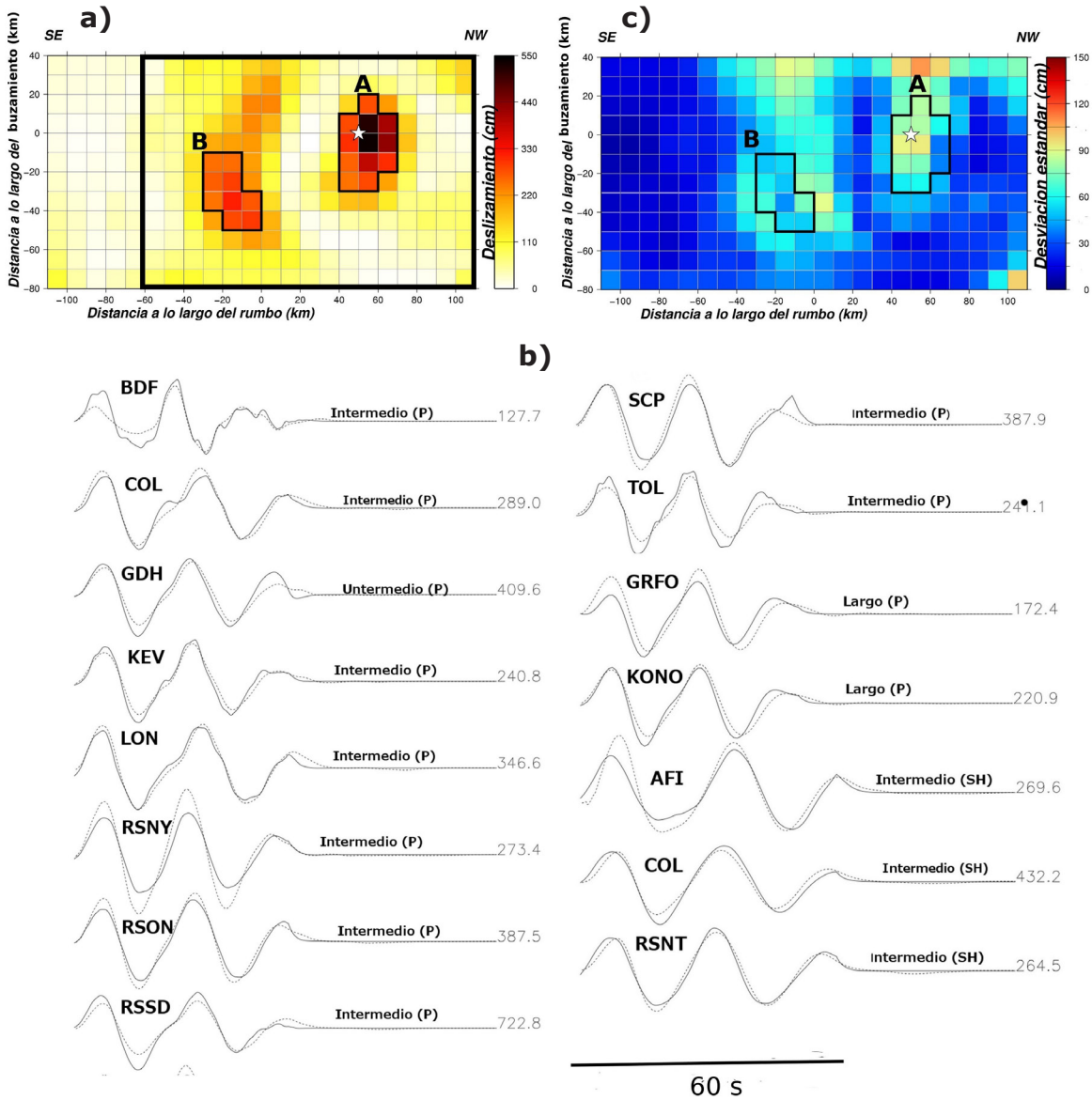

Figura 3. a) Modelo de deslizamiento obtenido para el evento del 19 de septiembre de 1985 a partir de la inversión de ondas P y SH telesismicas. El rectángulo corresponde a las zona de ruptura definida con el procedimiento de Somerville *et al*. (1999). Los polígonos marcan las celdas con deslizamiento mayor al 45% del deslizamiento máximo de cada fuente principal. La estrella representa el hipocentro. b) Los ajustes entre registros observados (línea continua) y teóricos (línea discontinua) para un momento sísmico de 9.8 x 10^{20} Nm (Mw 8.0). Los numeros a la derecha corresponden a la amplitud máxima (en micrones) del registro observado. c) Desviación estandar del deslizamiento estimado para celda después de 300 inversiones independientes variando el rumbo, buzamiento, ángulo de deslizamiento, profundidad y velocidad de ruptura.

(Mw 8.0). La Figura 3c muestra la desviación estándar del deslizamiento observado en cada celda a partir de las 300 inversiones. Para la zona **A** los valores de desviación estándar varían entre 40 y 95 cm. Para la zona **B** los valores varían entre 40 y 75 cm.

Sismo del 21 de septiembre de 1985 (Mw 7.5)

Mendoza (1993) determinó un modelo de deslizamiento para el evento de Zihuatanejo del 21 de septiembre de 1985 usando formas de onda P y SH telesísmicas y una sola ventana de tiempo de 1s. En este estudio se redeterminó el modelo telesísmico de deslizamiento utilizando 10 ventanas de tiempo permitiendo una duración

máxima de dislocación de 10s. Se invirtieron 13 registros de onda P de período largo e intermedio y 4 formas de onda SH de periodo intermedio. Se utilizó una longitud de registro de 75s con una disminución exponencial en amplitud a 40 y 50s para P y SH, respectivamente. Se uso una falla de 100 km x 100 km dividida en 400 celdas de 5 km x 5 km. Se utilizó un plano de falla con rumbo de 296°, buzamiento de 17°, y ángulo de deslizamiento de 85°. El hipocentro se colocó en el centro de la falla y se utilizó una velocidad de ruptura de 2.6 km/s.

Resultados de las pruebas utilizando diferentes profundidades indican que la profundidad de nucleación que mejor ajusta los datos observados es de 24 km. El modelo obtenido para esta profundidad se muestra en la Figura 4a. En esta se observa una zona de alto deslizamiento con un deslizamiento promedio de 245 cm, un área de 775 km² y una caída de esfuerzo de 0.8 MPa. La duración de dislocación en la zona de alto deslizamiento es de 6s. El momento sísmico total es de 1.7 x 10^{20} Nm (Mw 7.4), correspondiente a los ajustes que se muestran en la Figura 4b. La Figura 4c muestra la desviación estándar observada en cada celda a partir de las 300 inversiones. En la zona de alto deslizamiento del modelo obtenido se observan desviaciónes estándar entre 40 y 120 cm.

Sismo del 9 de octubre de 1995 (Mw 8.0)

Mendoza y Hartzell (1999) determinaron un modelo de deslizamiento para el sismo de Colima-Jalisco del 9 de octubre de 1995 (Mw 8.0) usando formas de onda P telesísmicas de banda ancha y 10 ventanas de tiempo de 2s cada una. Aquí hacemos una inversión similar con el mismo número de ventanas, invirtiendo registros banda ancha incluyendo 31 formas de onda P y 9 formas de onda SH. Se utilizan registros de 120s aplicando una disminución exponencial en amplitud a partir de 65s y 70s para las ondas P y SH, respectivamente. Se tomó la geometría de falla del gCMT con rumbo de 302**°**, buzamiento de 9**°** y ángulo de deslizamiento de 92**°**. La longitud y ancho de la falla son 220 km y 100 km, respectivamente. La falla fue dividida en 220 celdas de 10 km x 10 km. La velocidad de ruptura utilizada es de 2.8 km/s.

Resultados de la inversión usando diferentes profundidades hipocentrales indican que la profundidad que mejor ajusta los datos observados es de 15 km. El modelo correspondiente se muestra en la Figura 5a. Se observan tres fuentes principales, una cerca del hipocentro (**A**) con un pico de deslizamiento de ~175 cm, una segunda fuente (**B**) 50 km al noroeste con un deslizamiento máximo de ~310 cm y una tercer fuente (**C**) más al noroeste con un deslizamiento máximo de ~210 cm. Las fuentes **B** y **C** se encuentran separadas por ~20 km. La zona **A** tiene un deslizamiento promedio de 160 cm, un área de 900 km² y una caída de esfuerzo de 0.5 MPa. La zona **B** tiene un deslizamiento promedio de 175 cm, una área de 1500 km² y una caída de esfuerzo de 0.4 MPa. La tercera fuente (**C**) tiene un deslizamiento promedio de 180 cm, una área de 600 km² y una caída de esfuerzo de 0.7 MPa. En la Figura 5b se muestran los ajustes a los registros observados y corresponden a un momento sísmico de 6.0 x 10^{20} Nm (Mw 7.8). La Figura 5c muestra la desviación estándar del deslizamiento observado en cada celda a partir de las 300 inversiones. Para la fuente **A** se observa una desviación estándar de 30 a 60 cm. En la zona **B** los valores de desviación estándar varían entre 30 y 80 cm. El valor más alto de desviación estándar se observa en la celda de máximo deslizamiento de la Figura 5a. En la zona **C** los valores de desviación estándar se encuentran entre 55 y 75 cm.

Sismo del 22 de enero de 2003 (Mw 7.5)

Yagi *et al*. (2004) obtuvo un modelo de ruptura para el evento de Tecomán del 22 de enero de 2003 a partir de una inversión de datos locales y ondas P y SH telesísmicas. Ellos utilizaron 13 ventanas de tiempo de 1s cada una aplicando una metodología similar a la que se utiliza en este estudio. Aquí utilizamos 10 ventanas de tiempo de 1s cada una para invertir 31 registros banda ancha de onda P y 11 de onda SH. Se invirtió una longitud de registro de 80s con una disminución exponencial de amplitud después de 40s y 48s para ondas P y SH, respectivamente. Se utilizaron dimensiones de la falla de 100 km de largo y 80 km de ancho, dividida en 320 celdas de 5 km x 5 km. El hipocentro se ubica a 30 km del borde sureste y 50 km de la parte superior de la falla. Se tomó un plano de falla con rumbo de 308**°**, buzamiento de 12**°** y ángulo de deslizamiento de 110**°**. Se utilizó una velocidad de ruptura de 3.0 km/s.

Se realizaron pruebas para determinar la profundidad que mejor ajusta los datos observados, identificando una profundidad hipocentral de 22 km. La Figura 6a muestra el modelo de deslizamiento para esta profundidad. Se observan dos fuentes principales, una en la parte superior de la falla (**A**) con un deslizamiento máximo de 263 cm y otra (**B**) en la parte inferior con un deslizamiento máximo de 270 cm. En la zona **A** el deslizamiento promedio es de 205 cm dentro de un área de 250 km² con una caída de esfuerzo de 1.2 MPa. En la zona B el

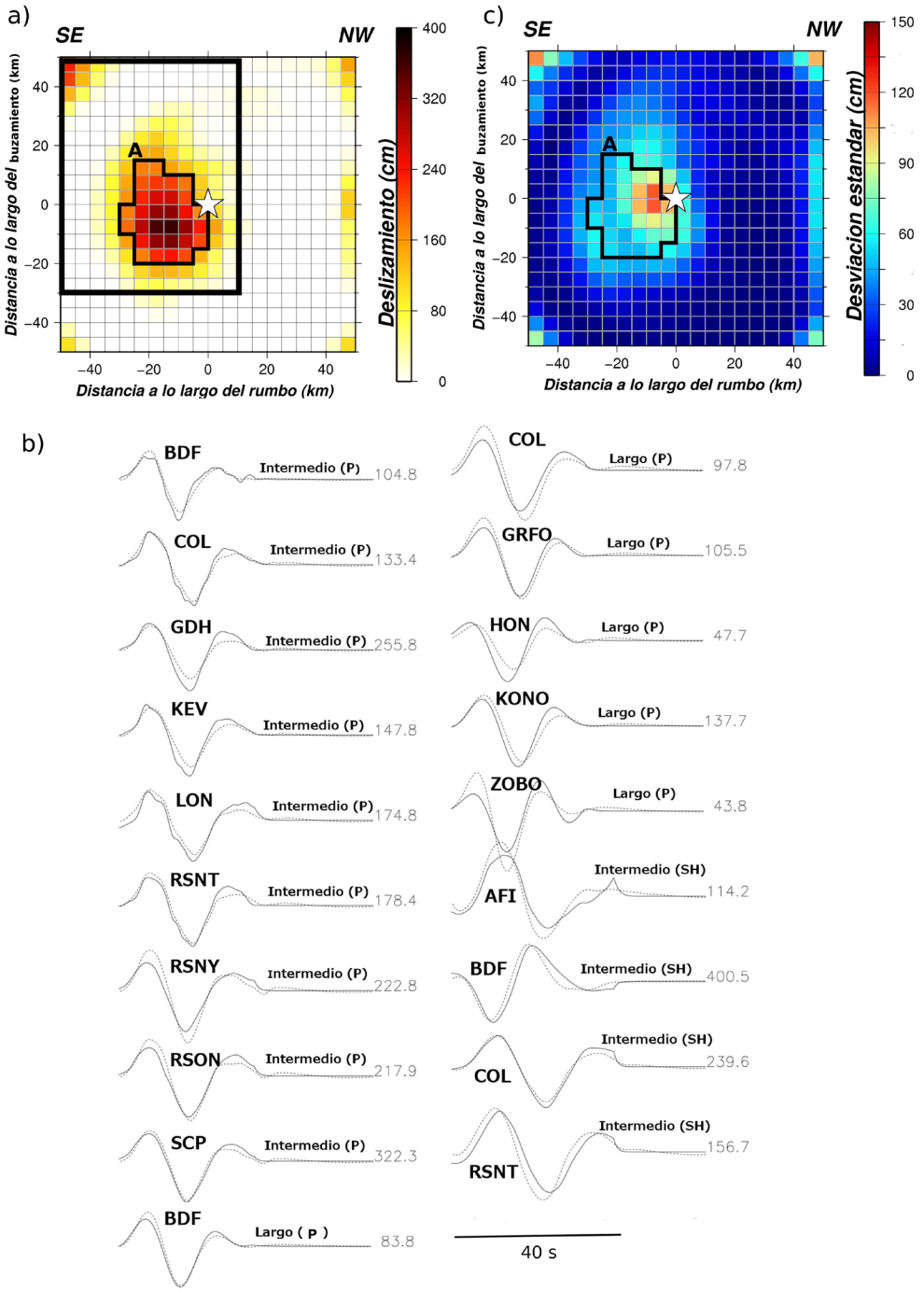

Figura 4. a) Modelo de deslizamiento obtenido para el evento del 21 de septiembre de 1985 a partir de la inversión de ondas P y SH telesísmicas. El rectángulo corresponde a la zona de ruptura definida con el procedimiento de Somerville *et al*. (1999). El polígono incluye las celdas con deslizamiento mayor al 45% del deslizamiento máximo y la estrella representa el hipocentro. b) Ajustes entre los datos observados (línea continua) y teóricos (linea discontinua) para un momento sismico de 1.7 x 10^{20} Nm (Mw 7.4). Los numeros a la derecha corresponden al pico de amplitud (en micrones) del registro observado. c) Desviación estándar del deslizamiento estimado para celda después de 300 inversiones independientes variando el rumbo, buzamiento, ángulo de deslizamiento, profundidad y velocidad de ruptura.

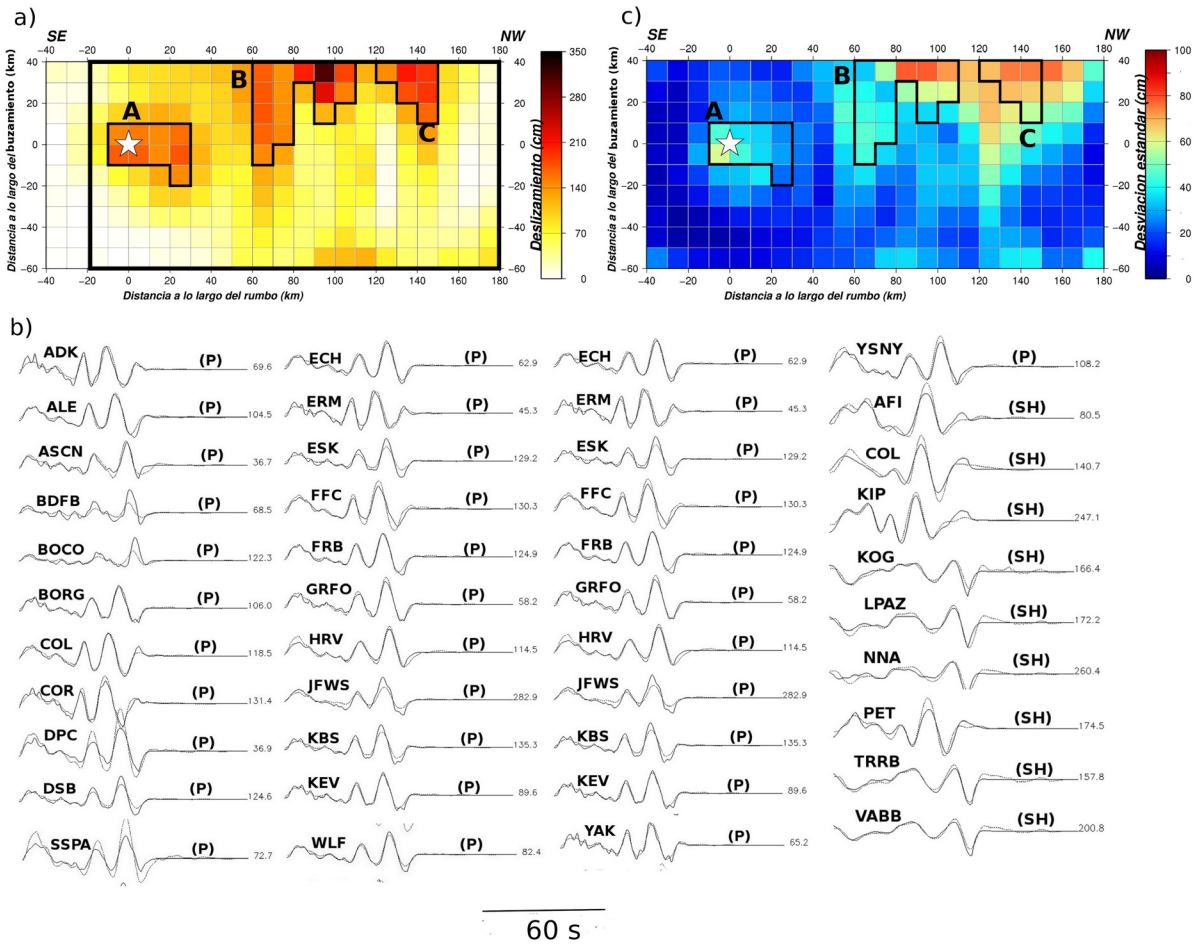

Figura 5. a)Modelo de deslizamiento obtenido para el evento del 9 de octubre de 1995 a partir de la inversión de ondas P y SH telesismicas. El rectángulo corresponde a la zona de ruptura definida con el procedimiento de Somerville *et al*. (1999). Los polígonos marcan las celdas con deslizamiento mayor al 45% del deslizamiento máximo de cada fuente principal. La estrella representa el hipocentro. b) Ajustes entre las formas de onda observadas (línea continua) y las teóricas (línea discontinua) para un momento sísmico de 6.0 x 10^{20} Nm (Mw 7.8). Los numeros a la derecha corresponden al pico de amplitud (en micrones) del registro observado. c) Desviación estandar del deslizamiento estimado para cada celda despues de 300 inversiones independientes variando el rumbo, buzamiento, angulo de deslizamiento, profundidad y velocidad de ruptura.

deslizamiento promedio es de 190 cm en un área de 500 km² con una caída de esfuerzo de 0.8 MPa. La duración de dislocación en las zonas **A** y **B** es de 6s y 4s, respectivamente. En la Figura 6b se muestran los ajustes que corresponden al momento sísmico estimado de 1.2 x 10^{20} Nm (Mw 7.3). La Figura 6c muestra la desviación estándar del deslizamiento observado en cada celda a partir de las 300 inversiones. Se observan valores altos de desviación estándar (~90 cm) en la parte superior de la falla. En la zona **A** se observan desviaciones estándar que varían de 35 a 90 cm. En la zona **B** se observan desviaciones entre 35 y 100 cm.

Distribución e incertidumbres de las asperezas

Los modelos telesísmicos de deslizamiento obtenidos en este estudio identifican zonas de alto deslizamiento que se interpretan como asperezas en el contacto interplaca. Estas asperezas se muestran en la Figura 7, representadas por los polígonos marcados en las Figuras 2 a 6 para cada evento. Se muestran además zonas de ruptura obtenidas utilizando el procedimiento de Somerville *et al*. (1999). Este procedimiento descarta filas y/o columnas de los modelos que no contribuyen de manera significativa al momento sísmico total y sirve para delinear de manera general la ubicación de

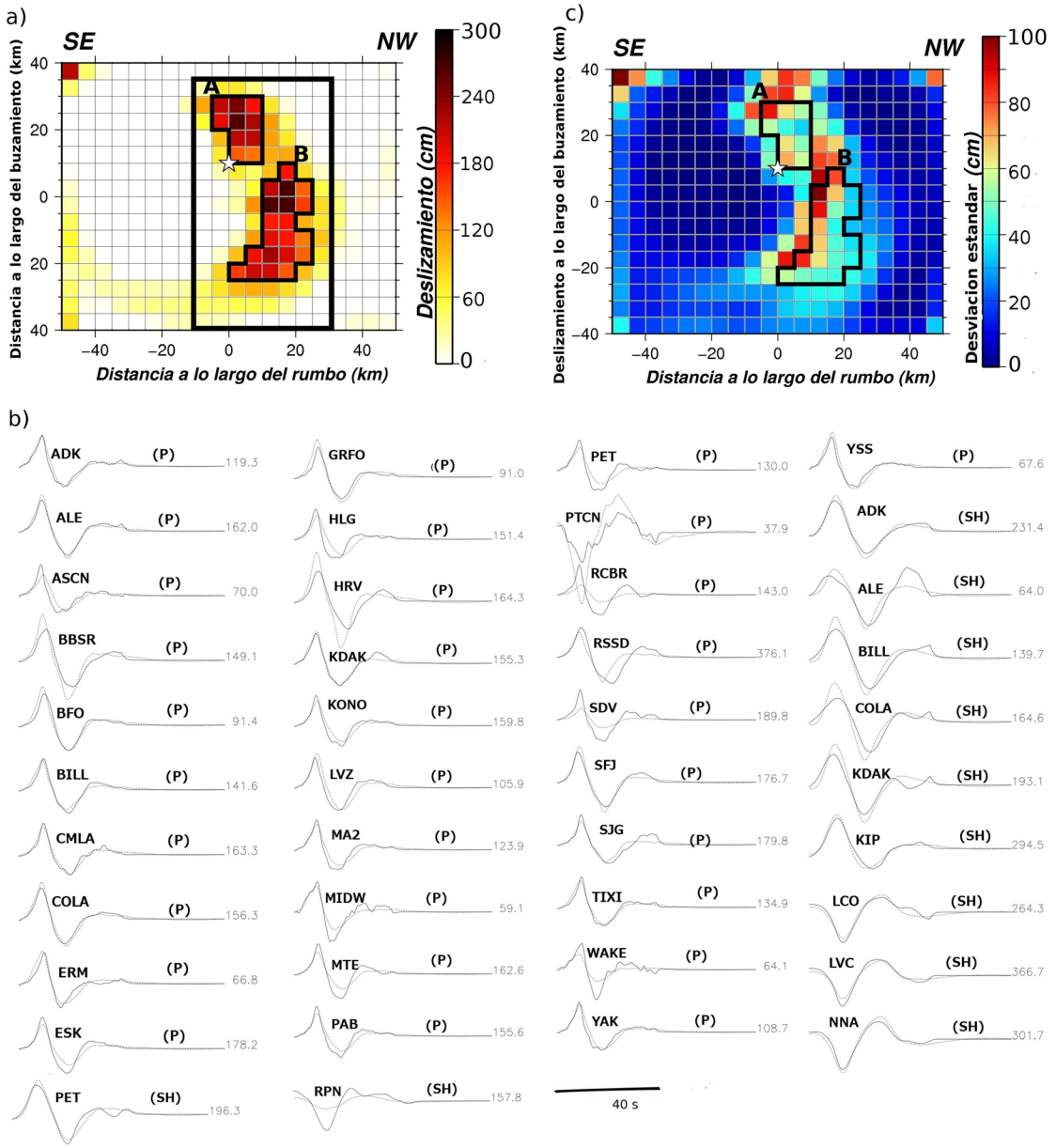

Figura 6. a) Modelo de deslizamiento obtenido para el evento del 22 de enero de 2003 a partir de la inversión de ondas P y SH telesismicas. El rectángulo corresponde a la zona de ruptura definida con el procedimiento de Somerville *et al*. (1999). Los polígonos incluyen las celdas con deslizamiento mayor al 45% del deslizamiento máximo observado para cada fuente principal. La estrella representa el hipocentro. b) Ajustes a los registros observados (línea continua) para un momento sismico de 1.2 x 10^{20} Nm (Mw 7.3). Los numeros a la derecha corresponden a la amplitud máxima (en micrones) del registro observado. c) Desviación estándar del deslizamiento estimado para celda después de las 300 inversiones independientes variando el rumbo, buzamiento, ángulo de deslizamiento, profundidad y velocidad de ruptura.

la ruptura en la zona de subducción. En general se observa que las rupturas de los sismos Mw ≥ 7 recientes (desde 1980) no se empalman, con excepción del evento de Playa Azul 1981 que se encuentra dentro de la zona de ruptura del sismo de Michoacán 1985. Sin embargo, las dos fuentes principales del evento de Michoacán 1985 excluyen la ruptura del evento de 1981 (p. ej., Astiz *et al*., 1987; Mendoza y Hartzell, 1989; Mendoza, 1993), consistente con la distribución de asperezas que se observa para los dos eventos en la Figura 7. En esta región también ocurrió el sismo histórico de Mw 7.6 del 7 de junio de 1911 pero la localización de este evento no está bien definida (Singh *et al*., 1981, Astiz *et al*., 1987) y es difícil examinar su relación con los eventos de 1981 y 1985.

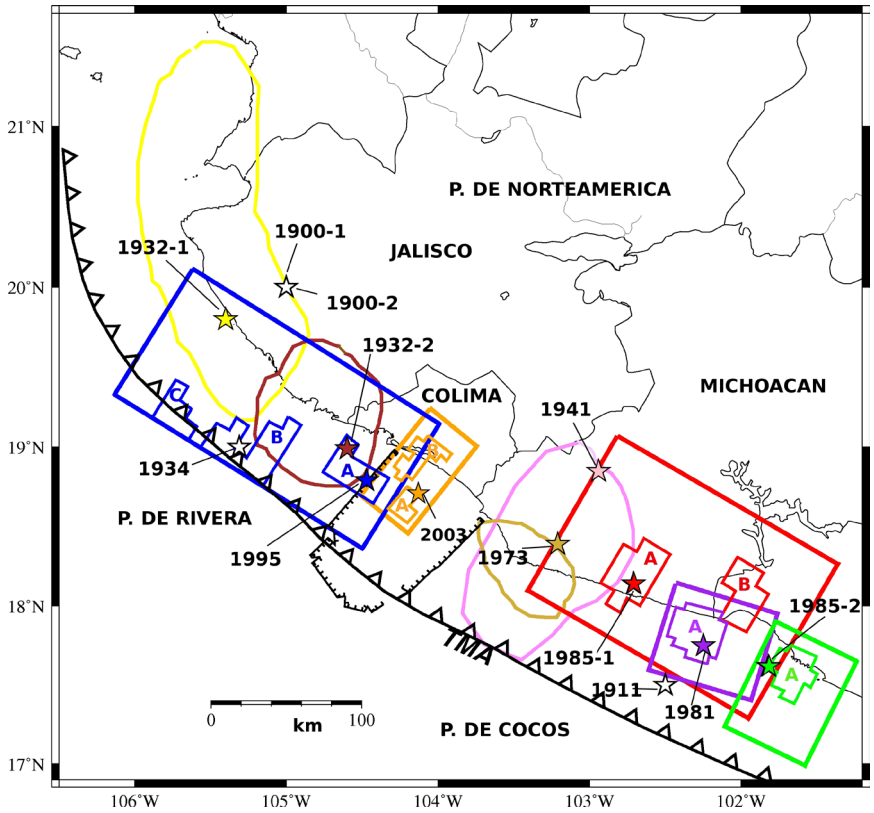

Figura 7. Asperezas en la zona de subducción Michoacán-Colima-Jalisco definidas a partir de los polígonos de alto deslizamiento identificados en los modelos de deslizamiento determinados en este estudio. Los rectángulos corresponden a las zonas de ruptura marcadas en las figuras 2 a 6. Se muestran además las áreas de réplicas que se conocen para los sismos del 3 de junio de 1932 (1932-1), del 18 de junio de 1932 (1932-2), del 15 de abril de 1941 y del 30 de enero de 1973 [tomadas de Ramírez-Herrera *et al*. (2010) y de Kelleher *et al*. (1973)].

La Figura 7 también muestra las áreas de réplicas que se conocen para sismos históricos ocurridos desde el año 1900. Estas áreas parecen coincidir con algunas de las zonas de ruptura de sismos recientes. Por ejemplo, la ruptura del evento del 9 de octubre de 1995 cubre la parte sur del área de réplicas del evento del 3 de junio de 1932 y las réplicas del sismo del 18 de junio de 1932 en la costa de Jalisco. Sin embargo, las réplicas de los eventos de 1932 se encuentran fuera de las asperezas del sismo de 1995. Esto es consistente con la conclusión de Pacheco *et al*. (1997) quienes sugieren que el evento de 1995 no corresponde a una repetición de los sismos de 1932 basado en una comparación de los sismogramas registrados para los eventos. En cambio, las réplicas del evento Mw 7.6 de 1973 si se encuentran dentro del área de réplicas determinada por Kelleher *et al*. (1973) para el sismo Mw 7.6 de 1941. La distribución de réplicas del sismo de 1941, sin embargo, esta definida con muy pocos epicentros (ver Kelleher *et al*., 1973) y es difícil evaluar la relación entre los dos eventos a pesar de que el evento de 1973 cuenta con un modelo preliminar de deslizamiento determinado por Santoyo *et al*. (2006).

En la Figura 7 se puede observar que las asperezas de sismos recientes de Mw > 7 forman un patrón entrelazado de zonas de alto deslizamiento. Por ejemplo, las asperezas de los eventos de 1995 y 2003 en la costa de Colima y también las asperezas de los sismos de 1981 y 1985 en Michoacán se ubican en lugares adyacentes en la zona de contacto interplaca. Esta observación es consistente con los resultados de Mendoza y Martínez López (2017) quienes observaron que las zonas de máximo deslizamiento del sismo de Papanoa del 2014 (Mw 7.3) en la costa de Guerrero no coinciden con las del evento de Petatlán de 1979 (Mw 7.4). Esta distribución de asperezas adyacentes podría implicar que los espacios entre asperezas de sismos anteriores identifican zonas de mayor deslizamiento en sismos futuros a lo largo del contacto interplaca (Mendoza y Martínez-López, 2017). Otra alternativa es que las asperezas se mantienen fijas en el tiempo y se deslizan en sismos recurrentes, aunque los sismos recientes

en la zona de Michoacán-Colima-Jalisco no muestran este comportamiento.

La Tabla 2 muestra las propiedades de las asperezas, representadas por valores promedio calculados de las 300 soluciones para los polígonos definidos anteriormente en las Figuras 2 a 6 para cada evento. Se incluyen valores promedio de 1) D_{max}, el deslizamiento máximo observado para cada aspereza, 2) D_p, el deslizamiento promedio dentro del polígono, y 3) T_d, la duración promedio de dislocación dentro de este mismo polígono. La Tabla 2 incluye la desviación estándar calculada para cada uno de estos tres parámetros. Las 300 soluciones independientes también se examinaron de manera individual para identificar variaciones en el área de las asperezas. Para cada evento, se identificaron las dimensiones mínimas y máximas de las asperezas y estas se utilizaron para identificar el rango de variación en el área. Basado en estos rangos, se calculo además la variación en la caída de esfuerzo de cada aspereza. Estos rangos en área y caída de esfuerzo se incluyen en la Tabla 2.

Los parámetros presentados en la Tabla 2 sirven para definir la variabilidad que puede haber en las propiedades de las asperezas tomando en cuenta los posibles errores en los parámetros de entrada que se utilizan en el proceso de inversión. Se puede observar que el deslizamiento máximo y promedio de las asperezas generalmente se mantienen en un rango de ~1-4 m con excepción del sismo de Playa Azul 1981 que tiene valores menores y la aspereza **A** del sismo de Michoacán 1985 que tiene valores mayores. Las duraciones de dislocación son parecidas para eventos de similar magnitud. Para los sismos de Mw ~7.5 los valores son de ~5s y para los sismos Mw 8 el valor es ~12s con una incertidumbre del orden del ancho de la ventana de tiempo, indicando que la duración de la dislocación en las asperezas se escala con el tamaño del sismo.

La variabilidad en el área de las asperezas es similar en general con excepción del sismo de Tecomán 2003 que muestra áreas más pequeñas con menor variabilidad. Este evento del 2003 tiene la mejor cobertura azimutal de estaciones, y la mejor definición en el área de las asperezas podría estar ligada a la distribución de estaciones. Se examinaron las ubicaciónes de las asperezas tomando en cuenta las incertidumbres en el área y se encontro que las asperezas siguen estando en lugares adyacentes a lo largo del contacto interplaca sin un empalme significativo, incluso para eventos que ocurrieron cerca de cada uno (p.ej. los sismos de 1995 y 2003 en Jalisco y los de 1981 y 1985 en Michoacán). Las incertidumbres en las dimensiones de las asperezas sugieren caídas de esfuerzo menores a 2.0 MPa para las asperezas, similares a los valores de 3.0 MPa que se observan en general para sismos de subducción (p.ej. Allmann y Shearer, 2009).

En algunos casos las soluciones individuales obtenidas de las 300 inversiones muestran más de una aspereza en el mismo lugar. Por ejemplo, en algunas de las soluciones del

Tabla 2. Propiedades de las asperezas de los eventos estudiados. Se listan valores promedio del deslizamiento máximo (Dmax), el deslizamiento promedio (Dp), y la duración promedio de dislocación (Td) junto con las desviaciones estándar, calculadas para cada aspereza a partir de 300 inversiones independientes. Se lista también la variabilidad observada en el área y en la caída de esfuerzo Δσ.

Evento	Aspereza	D_{max} (cm)	D_p (cm)	T_d (s)	Area (km^2)	Δσ (MPa)
25-10-1981 (Mw 7.2)	A	141 ±36	92 ±38	6± 1	690 -2210	0.10 – 0.38
19-09-1985 (Mw 8.0)	A	566 ±91	356 ±69	10 ±2	900 - 1400	0.64 – 1.42
	B	329±56	277 ±55	12 ±2	600 - 2200	0.49 – 1.55
21-09-1985 (Mw 7.5)	A	367 ±80	237 ±69	6 ±1	700 - 1600	0.32 – 1.90
9-10-1995 (Mw 8.0)	A	194 ±41	160 ±36	12 ±2	600 - 1800	0.22 – 0.58
	B	303±58	158 ±50	12 ±2	700 - 2100	0.24 – 0.96
	C	201 ±44	120 ±68	12 ±2	400 - 1300	0.25 – 1.11
22-01-2003 (Mw 7.5)	A	294 ±42	203 ±58	5 ± 1	250 - 330	0.95 – 1.49
	B	293 ±54	192 ±57	4 ±1	350 - 530	0.72 – 0.90

evento del 9 de octubre de 1995 las asperezas B y C se juntan para formar una sola fuente del tamaño aproximado de las dos asperezas. Similarmente, en algunas soluciones del evento del 22 de enero de 2003 las dos asperezas se juntan para formar una sola que cubre aproximadamente la misma área. Se observa que el momento sísmico total de estas áreas separadas corresponde a la suma del momento sísmico de las asperezas individuales. Estas observaciones reflejan el nivel de incertidumbre que existe en la aplicación de la metodología de falla finita utilizando los datos telesísmicos para estos eventos. Sin embargo, las ubicaciones de las zonas de alto deslizamiento en la zona de ruptura no varían significativamente, indicando que las asperezas de los sismos se pueden recuperar de manera adecuada. Estos resultados además indican que el procedimiento utilizado para muestrear los errores de los parámetros de entrada ofrece una alternativa para determinar las incertidumbres de las asperezas utilizando los datos telesísmicos.

Conclusiones y discusión

Se determinaron de manera sistemática los modelos de deslizamiento de los sismos de magnitud Mw mayor a 7 ocurridos desde 1980 en la zona de subducción de Michoacán-Colima-Jalisco utilizando ondas P y SH registradas a distancias telesísmicas. Se aplicó una metodología de inversión de falla finita utilizando una parametrización consistente que permite una amplia flexibilidad en la duración de dislocación. Los modelos de deslizamiento obtenidos de la inversión se utilizaron para definir las asperezas de los eventos en la zona de subducción. Se observa que las asperezas de los sismos recientes se entrelazan entre si a lo largo del contacto interplaca, consistente con los resultados de Mendoza y Martínez-López (2017), quienes encontraron que las zonas de alto deslizamiento del sismo Mw 7.3 de Papanoa en 2014 no coinciden con las áreas de máximo deslizamiento del sismo Mw 7.4 de Petatlán de 1979. Park y Mori (2007) observaron un patrón similar de empalme limitado entre asperezas para los zona de subducción de Nueva Bretaña en la región del sur-Pacífico.

Nuestros resultados indican además que el contacto interplaca en la región de Michoacán-Colima-Jalisco se ha roto en secciones individuales en los últimos 40 años y quizás los espacios entre asperezas de sismos recientes de Mw ~7 podrían identificar lugares de deslizamiento principal en eventos futuros como lo menciona Mendoza y Martínez López (2017). También es posible que las asperezas se mantienen fijas en el tiempo. Sin embargo, los eventos analizados en este estudio no muestran ese comportamiento, quizás debido al corto tiempo de evaluación. Sería importante realizar estudios más completos que incluyan una mayor cantidad de eventos para ver si el comportamiento observado en este trabajo se mantiene para distintos ciclos sísmicos.

En la zona de estudio no se puede descartar la posibilidad de que se rompa todo el segmento en un solo sismo. Esto se ha observado recientemente en otras zonas de subducción como Chile y Japón (Delouis *et al*., 2010; Simons *et al*., 2011) donde la interface de la placa tectónica se había estado rompiendo en eventos de magnitud Mw ~7-8 y no se esperaba un sismo de magnitud 9.0. En México se tienen reportes de un sismo histórico de magnitud Mw 8.6 en Oaxaca el 28 de marzo de 1787, en una región donde solo se han generado sismos de magnitud entre 7.3 a 8.2 en los últimos 100 años (Suárez y Albini, 2009). Es importante entonces seguir investigando el comportamiento de asperezas en esta y otras zonas de subducción para examinar el potencial sísmico real que pueda existir a nivel regional.

Se aplicó además un procedimiento simple donde se corrieron 300 inversiones independientes para identificar las incertidumbres en los modelos telesísmicos de cada evento tomando en cuenta los posibles errores en la geometría de la falla, la profundidad del hipocentro y la velocidad de ruptura. Este ejercicio permitio identificar la variabilidad en las propiedades específicas de las asperezas incluyendo el deslizamiento máximo, el deslizamiento promedio, la duración de dislocación, el área y la caída de esfuerzo. Las incertidumbres que se observan en las dimensiones de las asperezas no son suficientemente amplias para generar un empalme significativo entre asperezas, indicando que los posibles errores en la parametrización de la falla no afecta nuestra conclusión de asperezas entrelazadas para sismos recientes en la zona de subducción de Michoacán-Colima-Jalisco.

Nuestros resultados indican que a grandes rasgos el deslizamiento máximo, el deslizamiento promedio, y las dimensiones de las asperezas de los diferentes eventos son generalmente similares. Esto tendría implicaciones importantes para comprender el proceso de generación de sismos interplaca en zonas de subducción y también para la simulación realista del movimiento del suelo esperado. Sería importante entonces estudiar otros eventos para ver si estas similitudes generales se mantienen. Las duraciones de dislocación de las asperezas están relativamente

bien restringidas, con incertidumbres limitadas al ancho de la ventana de tiempo utilizada en el proceso de inversión. Se observan valores de duración para las asperezas que se escalan con el tamaño del evento (~5s y ~12s para sismos de Mw ~7.5 y de Mw 8.0, respectivamente). Las caídas de esfuerzo calculadas para todas las asperezas se mantienen menores a 2.0 MPa, consistente con valores estimados previamente para sismos interplaca en zonas de subducción. Los resultados de la investigación indican que un simple muestreo de los parámetros de entrada ofrece una alternativa para examinar las propiedades e incertidumbres de las asperezas.

Los resultados de este estudio también tienen implicaciones importantes para la estimación de leyes de escalamiento que relacionan los diferentes parámetros de la fuente sísmica. Se han desarrollado leyes de escalamiento para zonas de subducción a partir de modelos de deslizamiento recuperados para eventos de fallamiento inverso (p. ej. Somerville *et al*., 2002; Murotani *et al*., 2008; 2013; Ramirez-Gaytan *et al*., 2014). Sin embargo, los modelos de deslizamiento se han determinado con diferentes metodologías, datos y parametrizaciones de la falla lo cual dificulta una definición confiable y consistente de las zonas de alto deslizamiento. Los modelos de deslizamiento que se utilizan además tienen incertidumbres que no se han tomado en cuenta y sería de gran utilidad poder incorporar estas incertidumbres para considerar la posible variabilidad en los parámetros de la fuente. Para la zona de subducción de México, por ejemplo, sería útil examinar las asperezas de todos los eventos de magnitud Mw mayor a 7 que han ocurrido desde 1980 siguiendo el procedimiento desarrollado en este trabajo. Esto resultaría en una definición mas realista de las leyes de escalamiento, lo cual mejoraría el conocimiento actual del peligro sísmico.

Agradecimientos

Este trabajo fue financiado por los proyectos de UNAM/PAPIIT IN104317 y el proyecto CONACYT Problemas Nacionales-PN2015-639. Las imágenes se realizaron con el programa GMT (Generic Mapping Tools) de Wessel y Smith (1991). Además agradecemos los comentarios de dos revisores anónimos.

References

Anderson, J. G., Singh S. K., Espíndola J. M., y Yamamoto J., 1989, Seismic strain release in the Mexican subduction thrust, *Phys. Earth Planet Interiors*, 58, 307-332.

Allmann B. P. y P. M. Shearer, 2009, Global variations of stress drop for moderate to large earthquakes, *J. Geophys. Res., 114, B01310*.

Astiz L., Kanamori H. y Eissler H., 1987, Source characteristics of earthquakes in the Michoacan Seismic Gap in Mexico, *Bull. Seism. Soc. Am.,* 77, 4, 1326-1346

Beresnev, I. A., 2003, Uncertainties in Finite-Fault Slip Inversions: To What Extent to Believe? (A Critical Review), *Bull. Seism. Soc. Am., 93, 6, 2445-2458.*

Courboulex, F., Singh S. K., Pacheco J. F. y Ammon C. J., 1997, The 1995 Colima-Jalisco, Mexico, earthquake (Mw 8): A study of the rupture process, *Geophys. Res. Lett., 24, 1019-1022*.

Delouis, B., Norquet J. M. y Vallée M., 2010, Slip distribution of the February 27, 2010 Mw=8.8 Maule Earthquake, central Chile, from static and high-rate GPS, InSAR, and broadband teleseismic data, *Geophys. Res. Lett* 37, L17305.

Esteva L., 1988, La investigación y la práctica de la Ingeniería Sísmica en México después de los sismos de 1985, *Rev. Soc. Mex. Ing. Sísm, 34*.

Eshelby, J. D., 1957, The determination of the elastic field of an ellipsoidal inclusion and related problems, *Proc. Roy. Soc., A241, 376-396*.

Hartzell S. H. y Heaton T., 1983, Inversion of strong motion and Teleseismic waveform data for the fault rupture history of the 1979 Imperial Valley, California, earthquake, *Bull. Seism. Soc. Am., 73, 6A, 1553-1583*.

Hartzell, S. H. y. Heaton T. H., 1986, Rupture history of the 1984 Morgan Hill, California, earthquake from the inversion of strong motion records, *Bull Seism. Soc. Am. 76, 649-674*.

Hartzell, S., 1989, Comparison of seismic waveform inversion results: Application to the 1986 North Palm Springs, California, Earthquake, *J. Geophys. Res., 94, 7515-7534*.

Hartzell, S. y Langer Ch., 1993, Importance of model parameterization in finite fault inversions: Application to the 1974 Mw 8.0 Peru Earthquake, *J. Geophys Res., 98,*

22123-22134.

Hartzell, S., Mendoza C., y Zeng, 2013, Rupture model of the 2011 Mineral, Virginia, earthquake from teleseismic and regional waveforms, *Geophys. Res. Lett., 10, 1-6.*

Havskov, J., Singh S. K., Nava E., Dominguez T., y Rodríguez M., 1983, Playa Azul, Michoacán, Mexico Earthquake of 25 October 1981 (M s = 7.3), *Bull. Seism. Soc. Am. 73, 449-457*.

Juarez-García, H., Whitney R. A., Guerrero J. J., Gama A., Vera R., y Hurtado F., 1997, The October 9, 1995, Manzanillo, Mexico, earthquake, *Seism. Res. Lett., 68, 413-425*.

Kanamori, H., 1978, Quantification of earthquakes, *Nat., 411-414.*

Kanamori, H., 1981, The nature of seismicity patterns before large earthquakes, *Earthquakes Prediction 1-19.*

Kelleher, J., Sykes, L., y Oliver, J., 1973, Possible Criteria for Predicting Earthquake Locations and their Application to Major Plate Boundaries of the Pacific and the Caribbean, *J. Geophys. Res., 78, B14, 2547-2585.*

Lay y Kanamori, 1981, An asperity model of large earthqukes sequences, *Earthquakes Prediction*, *579-592*.

Lay T., Kanamori H., y Ruff L., 1982, The asperity model and the nature of large subduction zone earthquakes, *Earthquake Prediction Research, 1, 3-71*.

Lay, T., Ammon C. J., Kanamori H., Koper K. D., Sufri O., y Hutko A. R., 2010, Teleseismic inversion for rupture process of the 27 February 2010 Chile (Mw 8.8) earthquake, *Geophys. Res. Lett., 37, 13.*

Lomnitz, C., 1977, A procedure for eliminating the indeterminacy in focal depth determination. *Bull. Seism. Soc. Am., 67, 533-535*.

Martínez-López R. y Mendoza C., 2015, Acoplamiento Sismogénico en la zona de subducción de Michoacán-Colima-Jalisco, México, *Bol. Soc. Geol. Mex., 68, 2, 199-214*.

Mendoza, C. y Hartzell S., 1988, Aftershock Patterns and main shock faulting, *Bull. Seism. Soc. Am., 78, 4, 1438-1449.*

Mendoza, C. y Hartzell S., 1989, Slip distribution of the 19 September 1985 Michoacan, Mexico, *Bull. Seism. Soc. Am., 79, 3, 655-669*.

Mendoza, C., 1993, Coseismic slip to Two Large Mexican Earthquakes From Teleseismic Body waveforms Implications for Asperity Interaction in the Michoacán Plate Boundary Segment, *J. Geophys. Res., 98, B5, 8197-8210*.

Mendoza, C., 1995, Finite-Fault Analysis of the 1979 March 14 Petatlan, Mexico, Earthquake Using Teleseismic P-Wave-Forms: *Geophys. J. Inter., 121(3), 675-683.*

Mendoza, C. y Hartzell S., 1999, Fault-Slip Distribution of the 1995 Colima-Jalisco, Mexico, Earthquake, *Bull. Seism. Soc. Am., 89, 5, 1338-1344*.

Mendoza, C., Castro-Torres S., y Gomez Gonzalez J. M., 2012, Moment -Constrained Finite-Fault Analysis using Teleseismic P waves: Mexico Subduction zone, *Bull. Seismol. Soc. Am.*, 101,6, 2675-2684.

Mendoza, C. y Hartzell S., 2013, Finite fault Source Inversion Using Teleseismic P waves: Simple Parametrization and Rapid Analysis, *Bull. Seism. Soc. Am.*, *103, 834-844*.

Mendoza C. y Martinez Lopez R., 2017, The Mw 7.3 Papanoa, Mexico earthquake of April 18, 2014: Implications for recurrent Mw > 7 thrust earthquakes in western Guerrero, *Geof. Int., 56:1, 13-26*.

Murotani, S., Miyake H. y Koketsu K., 2008, Scaling of characterized slip models for plate-boundary earthquakes, *Earth Planet Space, 60, 987-991*.

Murotani, S., Satake R. y Fujii, 2013, Scaling relations of seismic moment, rupture area, average slip, and asperity size for M~9 subduction-zone earthquakes, *Geophys. Research Lett.,* 40, 19, 5070-5074.

Pacheco, J. y Sykes L.R., 1992, Seismic moment catalog of large shallow earthquakes, 1900 to 1989, *Bull. Seism. Soc. Am., 82, 1306-1349, 1992.*

Pacheco, J., Singh S. K., Domínguez J., Hurtado A., Quintanar L., Jiménes Z., Yamamoto J., Gutiérrez C., Santoyo M., Bandy W., Guzmán M., y Kostoglodov V., 1997, The October 9, 1995 Colima-Jalisco, Mexico earthquake (Mw 8): An aftershock study and a comparison of this earthquake with those of 1932, *Geophys.*

Res. Lett., 24, 17, 2223-2226.

Park S. y Mori J., 2007, Are asperity patterns persistent? Implication from large earthquakes in Papua New Guinea, J. *Geophys. Res., 112, B3303.*

Ramírez-Herrera, M.T., Kostoglodov, V., Urrutia-Fucugauchi, J., 2010, Overview of Recent Coastal Tectonic Deformation in the Mexican Subduction Zone: *Pure and Applied Geophysics, 168(8), 1425-1433.*

Ramírez-Gaytán, A., Aguirre, J., Jaimes. M.A., Huérfano V., 2014, Scaling Relationships of source Parameters of Mw 6.9-8.1 Earthquakes in the Cocos-Rivera-North American Subduction Zone: *Bull. Seism. Soc. Am., 104(2), 840-854.*

Santoyo, M. A., Singh S. K., Mikumo T., y Ordaz M., 2005, Space-time Clustering of Large Thrust Earthquake along the Mexican Subduction Zone: An Evidence of Source Stress Interaction, *Bull. Seismol. Soc. Am.*, 95, 5, 1856-1869.

Santoyo A. M., Mikumo, T., Quintanar, L., 2006, Faulting process and coseismic stress change during the 30 January, 1973, Colima, Mexico interpolate earthquake (Mw=7.6), *Geof. Inter. 45(3), 163-178.*

Simons M., Minson S. E., Sladen A., Ortega F., Jiang, Owen J. S. E., Meng L., Ampuero J., Wei Sh., Chu R., Helmberger D. V., Kanamori H., Hetland E., Moore A. W., Webb F. H., 2011, The 2011 Magnitude 9.0 Tohoku-Oki Earthquake: Mosaicking the Megathrust from seconds to centuries, *Science 332, 1421.*

Singh S. K., Askiz L. y Hasvkov J., 1981, Seismic Gaps and recurrence periods of large Earthquake along the Mexican subduction zone: A reexamination, *Bull. Seism. Soc. Am*., 71, 3, 827-843.

Singh, S. K., Ponce L. y Nishenko S. P., 1985, The great Jalisco, Mexico, earthquakes of 1932: Subduction of the Rivera Plate, *Bull. Seism. Soc. Am*., ***75*** *5, 1301-1313*.

Stolte C., McNally K.C., González-Ruiz J., Simila G.W., Reyes A., Rebollar C., Munguia L., Mendoza L., 1986, Fine structure of a post-failure Wadati-Benioff zone, *Geophys. Res. Lett., 13, 577-580*.

Somerville, P. K. Irikra, R, Graves, S. Sawada, D. Wald N. Abrahamson, Y. Iwasaki, T. Kagawa, N. Smith y A. Kowada A., 1999, Characterizing crustal earthquake slip models for the prediction of strong ground motion, *Seismol. Res. Lett., 70, 59-80*.

Somerville, P., Collins N., Sato T., Ishii T., Dan K., y Fujiwara H., 2002, Characterizing heterogeneous slip models for large subduction earthquakes for strong ground motion prediction, i*n Proc. of the 11th Symp. of Earthq. Eng., 1, 163-166*.

Suárez, G. y Albini, P., 2009, Evidence for Great Tsunamigenic Earthquakes (M 8.6) along the Mexican Subduction Zone, *Bull. Seism. Soc. Am*., 99(2A), 892-896.

UNAM Seismology Group, 1986, The September 1985 Michoacán Earthquakes: Aftershock Distribution and History of Rupture, *Geophys. Res. Lett., 13, 573-576*.

UNAM Seismology Group, 2015, Papanoa, Mexico earthquake of 18 April 2014 (M W 7.3), *Geof. Int., 54-4, 363-386.*

Yagi, Y., Mikumo T. y Pacheco J., 2004, Source rupture of the Tecoman, Colima, México earthquake of January 22, 2003, determined by joint inversion teleseismic body wave and near field data, *Bull. Seism. Soc. Am., 94, 1795-1807.*

Wessel, P. and W. H. F. Smith, Free software helps map and display data, *EOS Trans. AGU, 72, 441, 1991.*